Title
Multi-Spacecraft Observations of Collisionless Shocks in the Heliosphere

Author
Hanson, Elizabeth

Publication Date
2020

Peer reviewed|Thesis/dissertation

Multi-Spacecraft Observations of Collisionless Shocks in the Heliosphere

by

Elizabeth Hanson

A dissertation submitted in partial satisfaction of the

requirements for the degree of

Doctor of Philosophy

in

Physics

in the

Graduate Division

of the

University of California, Berkeley

Committee in Charge:

Professor Stuart Bale, Chair
Professor Eliot Quataert
Professor Jonathan Wurtele

Summer 2020

Abstract

Multi-Spacecraft Observations of Collisionless Shocks in the Heliosphere

by

Elizabeth Hanson

Doctor of Philosophy in Physics

University of California, Berkeley

Professor Stuart Bale, Chair

In this work, we introduce background relevant to and our own analyses of collisionless shock observations in the heliosphere. The observations of interest are in situ measurements collected by spacecraft immersed in the plasma. We introduce basic concepts in the physics of shocks and space plasmas and describe some specific techniques appropriate for the analysis of shock observations. Then we discuss the spacecraft mission that provided the data for our studies: a four-probe constellation known as Magnetospheric Multiscale (MMS). Instruments providing the most necessary measurements to our work (electric fields, magnetic fields, and particle distributions and moments) are discussed individually. The subsequent three chapters, detailing the analyses we performed on this data, represent the work we have published on the subject.

In the first paper, we compare shock normals, planarities, and Normal Incidence Frame (NIF) cross-shock potentials determined from electric field measurements and proxies, for a subcritical (Fast Magnetosonic Mach number $M_F = 1.1 \pm 0.1$) interplanetary (IP) shock and a supercritical bow shock ($M_F = 2.13 \pm 0.04$). The low-Mach shock's cross-shock potential was 26 ± 6V. The shock scale was 33km, too short to allow comparison with proxies from ion moments. Proxies from electron moments provided potential estimates of 40 ± 5V. Shock normals from magnetic field minimum variance analysis were nearly identical, indicating a planar front. The high-Mach shock's cross-shock potential was estimated to be from 290 to 440V from the different spacecraft measurements, with shock scale 120km. Reflected ions contaminated the ion-based proxies upstream, whereas electron-based proxies yielded reasonable estimates of 250 ± 50V. Shock normals from electric field maximum variance analysis differed, indicating a rippled front.

For the second paper, we investigate the dependence of shock parameters (speed v_{sh}, normal $\hat{n}$, and angle θ_{Bn}) on the choice of upstream and downstream regions for 51 bow shock crossings in MMS Fast Survey data. We summarize guidelines for selecting stream regions based on the magnetic field and particle moments. Preferred upstream and downstream combinations were identified by minimizing RH conservation errors. Comparing parameters from different up/downstream combinations provided a measure of how stream region choices affect the parameters. Shifting from the preferred stream region combination to another would cause <5° change in $\hat{n}$ for 90% of shocks, <15km/s change in v_{sh} of 70% of shocks, and <5° change in θ_{Bn} for 84% of shocks. All parameters would shift by more than their standard deviations σ. The most

robust is $\hat{n}$, which would change by <1σ for 22% and <3σ for 86% of shocks, while v_{sh} is the least robust, changing by <3σ for only 12% of shocks. Summary plots and detailed lists of parameters are provided in a separate Supplement, freely available at https://doi.org/10.5281/zenodo.3583341.

In the third paper, we return to the IP shock that was recorded crossing the MMS constellation on 2018 January 8. Plasma measurements upstream of the shock indicate efficient proton acceleration in the IP shock ramp: 2-7 keV protons are observed upstream for about three minutes (~8000 km) ahead of the IP shock ramp, outrunning the upstream waves. The differential energy flux (DEF) of 2-7 keV protons decays slowly with distance towards the upstream region (dropping by about half within 8 Earth radii from the ramp) and is lessened by a factor of about four downstream from the ramp (within a distance comparable to the gyroradius of ~keV protons). Comparison with test-particle simulations has confirmed that the mechanism accelerating the solar wind protons and injecting them upstream is classical shock drift acceleration. This example of observed proton acceleration by a low-Mach, quasi-perpendicular shock may be applicable to astrophysical contexts, such as supernova remnants or the acceleration of cosmic rays.

Table of Contents

Preface

I was anticipating a rather more pedestrian ordeal for the writing of my dissertation.

In a sense, my self-imposed sequestering wouldn't have differed much from the lockdowns that have been mandated by public health authorities. I work out before breakfast, try to focus on my dissertation with unpredictable success, clear my head with an hour-long walk in the late afternoon, and practice my instrument.

What's different is that I would have been working out at the gym instead of at home and dancing tango several times a week. My weekends would have been a blitz of errands, arts events, or social engagements. I would not have been sewing cloth face masks, and the news would have been easier to tune out when I need to focus. Between a global health emergency and a national identity crisis, my own concerns have often felt trivial and my research charming but abstruse.

Either way, I would probably have written the bulk of my dissertation in pencil while lying on the floor of my studio. Writing on the floor is not a new habit.

Berkeley, summer 2020

Acknowledgements

Many people in my life deserve heartfelt thanks. My apologies to any that I neglect to mention; any such omissions are "something of my negligence, nothing of my purpose".

For work with the Parker Solar Probe electronics testing: Dennis Seitz, Helen Yuan, Sasha Siy, and John Bonnell.

For work with THEMIS/ARTEMIS data: Chadi Salem, John Bonnell, and Chris Chaston.

For work with shocks in MMS data: Forrest Mozer, Oleksiy Agapitov, Vladimir Krasnoselskikh, Stuart Bale, Ivan Vasko, and the MMS teams that made the mission possible.

For undergraduate research and foundations: Cynthia Cattell, John Dombeck, and the University of Minnesota space physics group.

Special thanks go to my canine collaborator HK for her attentive participation in science discussions and for a generous Office Hours policy throughout her tenure at SSL.

For artistic fellowship and support: Diana Stork, Cheryl Ann Fulton, Miranda Lindelöw, Madeleine Cule, and all the tender hearts at Abrazo Queer Tango.

Deep gratitude and affection are owed to my family and friends for years of unstinting encouragement and support.

Last but hardly least, I offer general thanks for my harp, Leontine. Not until graduate school did I appreciate how the intangibility and transience of music – its "dying fall" – could release the pressure of written symbols, page upon page upon page, loading down my psyche.

Chapter 1
Introduction

Throughout this document, the emphasis will be on *in situ* observations of space plasmas, the adoptive home of satellites flung from Earth, with special consideration for the challenges and rewards of measuring low-frequency electric fields. Our intrepid scout in this case is not a single probe: the Magnetospheric Multiscale (MMS) mission's four spacecraft fly in a tetrahedral formation with separation distances as low as a few tens of km.

Such multi-spacecraft observations are especially desirable in the context of collisionless shocks, where the physics is more readily untangled when simultaneous measurements from multiple positions are available. Our primary interest is in quasi-perpendicular shocks: the Earth-centered orbit of MMS has led to the accumulation of many invaluable observations as the constellation travels from the magnetosphere into the solar wind and back, crossing the terrestrial bow shock along the way. When the spacecraft are in the solar wind, there is always the chance that an interplanetary (IP) shock will serendipitously pass by, adding an intriguing but unpredictable point of comparison for the bow shock measurements.

In Part I, before we delve into any detailed analysis, we will naturally dwell on critical foundational concepts. Chapter 2 is devoted to the fundamentals of shock physics, starting with the distinctions between collisional, hydrodynamic shocks (more ordinary companions of everyday life) and collisionless plasma shocks (seemingly a vexing paradox). Collisionless plasma shocks being the more entertaining variety, and the sort that our satellites encounter in space, we proceed thereafter to describe them in greater detail.

Part II addresses data processing and acquisition. Some special processing and analysis techniques were of particular use to us, and these are discussed in Chapter 3. We also explain some of the challenges of and strategies for measuring electric fields at low frequencies and calibrating the data that result. Other techniques are particular to the analysis of shock observations, such as various strategies for elucidating the geometry of the shock.

Chapter 4 is devoted to MMS, the space mission that collected the data we used. This four-spacecraft constellation in orbit around the Earth passes routinely though the bow shock, a by-product formed as the solar wind flows continually past the Earth's magnetosphere. A little good luck resulted in the collection of an IP shock observation, which we have also explored. MMS offers a valuable complement of instruments, operating at high resolution in both time and space. Specific instruments most applicable to our work are described individually.

It was for the sake of reconnection studies rather than shocks that the MMS mission was developed: at that time, urgent questions in reconnection science could not be resolved without detailed observations at electron scales. Thus, the mission was tailored to provide multipoint measurements at exceptionally high sampling rates while the spacecraft were separated by distances comparable to the local electron inertial length (Burch et al., 2016).

Since the increase of its orbital apogee in later phases of the primary mission, and thanks to the precession of its orbit, the MMS constellation regularly crosses the terrestrial bow shock, covering a broad interval of Magnetic Local Times from near dawn to near dusk (Fuselier et al., 2016). This range of crossing points means that MMS samples a variety of characteristic shock parameters, which makes it a valuable mission for studying not just reconnection but also collisionless shocks.

In the six decades since research into collisionless shocks first began, space missions have provided crucial observations of IP shocks and the terrestrial bow shock. Examples include ISEE (Sckopke et al., 1983), Cluster and THEMIS (Hobara et al., 2010), Polar (Hull et al., 2006), Wind (Wilson et al., 2012); now MMS is joining their ranks.

In Part III, we detail our analyses and results. Chapter 5 consists of a study comparing two markedly different shocks: a strong bow shock with rippled geometry and disruptive ion reflection versus a weak but fast-moving IP shock with planar geometry and more complex but subtle ion dynamics (Cohen et al., 2019; Hanson et al., 2019; Hanson, Agapitov, Vasko, et al., 2020). The main measurement of interest was the electrostatic potential across the shock transition, which we compared to proxy calculations.

While much progress has been made in understanding the mechanisms of energy transformation from the bulk ion flow to the thermal and suprathermal populations (see reviews (Bale et al., 2005; Krasnoselskikh et al., 2013) and references therein), only a few publications previously treated measurements of electric field and potential across the shock (Bale et al., 2008; Bale & Mozer, 2007; M. Balikhin et al., 2005; M. A. Balikhin et al., 2002; Dimmock et al., 2011, 2012; Formisano, 1982; Heppner et al., 1978; Hobara et al., 2010; Scudder, Mangeney, Lacombe, Harvey, & Aggson, 1986; Scudder, Mangeney, Lacombe, Harvey, Aggson, et al., 1986; Scudder, Mangeney, Lacombe, Harvey, Wu, et al., 1986; Walker et al., 2004; Wygant et al., 1987).

The difficulty of measuring *in situ* electric fields is one reason for the scarcity of electric field studies, but when adequate measurements are available, it is possible to estimate the cross-shock potential. The cross-shock potential impacts energy redistribution at the shock front (Zank et al., 1996) and other physical processes in the shock. Goodrich & Scudder (1984) were the first to point out the dependence of potential field on the reference frame and to highlight the role of the potential in the formation of flat-top and beam-like characteristics of the electron distribution.

In Chapter 6, we take a different approach and process a database of over 50 bow shock observations using a modified Rankine-Hugoniot (RH) analysis. We repeated the RH analysis four times for every spacecraft's data from every shock, each time with a different combination of handpicked upstream and downstream regions. The goal was to understand the consequences that stream region choices have on the calculated shock parameters and geometry (Hanson, Agapitov, Mozer, et al., 2020).

Early spacecraft observations of collisionless shocks were limited by low data sampling rates, which made it natural to concentrate on analysis of the macroscopic features and physics (Formisano, Hedgecock, et al., 1973; Formisano, Moreno, et al., 1973; Formisano & Hedgecock, 1973; Kennel et al., 2013; Leroy et al., 1982). Whether a given study inclines more to the macroscopic or the microscopic view, situating a given shock within the context of previous work still involves estimation of average plasma parameters before and after the shock, in the so-called upstream and downstream regions. The low sampling rates of measurements used in early studies necessitated averaging over long periods of minutes before and after the shock (e.g. Formisano, Hedgecock, et al., 1973; Newbury et al., 1998). Advances in spacecraft measurement technology have resulted in sophisticated measurements at much higher cadences: selecting data appropriate for the upstream and downstream averages can now present a surfeit of options.

Chapter 7 returns to the IP shock of Chapter 5. A unique feature of this event was the observation of higher-energy (2-7keV) protons upstream of the shock front for a sustained period of nearly three minutes. This long-lived population could be seen partly thanks to the planar geometry of the shock and partly because the shock was not strongly quasi-perpendicular, having a shock angle of only 69°. Comparison to a test particle simulation helped us to conclude that

shock drift acceleration (SDA) was likely responsible for accelerating these protons (Hanson, Agapitov, Vasko, et al., 2020).

Although our observations are taken within the heliosphere, collisionless shocks occur throughout the universe, where they may shape the emissions of supernovae or accelerate cosmic rays (Biermann et al., 2018; Gargaté & Spitkovsky, 2012). Gradients within the shock transition may lead to SDA: ions may travel along the shock front and gyrate through the ramp, gaining energy with each pass before they escape upstream or downstream (Armstrong et al., 1985; Decker & Vlahos, 1985; Pesses et al., 1982). SDA has been combined with diffusive shock acceleration (DSA) in some models because both mechanisms act on particles drifting along the shock front within a small distance (comparable to the ion gyroradius) of the ramp (Jokipii, 1982). Ion acceleration models that rely upon time spent within the strong field gradients of the shock transition are relevant not only to solar wind but also to interstellar pick-up ions and the heliospheric termination shock (Lee et al., 1996; Zank et al., 1996). In addition, SDA and DSA have been proposed as mechanisms that may explain observations of cosmic rays and supernova remnants (Biermann et al., 2018; Caprioli & Spitkovsky, 2014; Gargaté & Spitkovsky, 2012; Ohira, 2016; Park et al., 2015; Zank et al., 2015).

Chapter 8 briefly summarizes the whole and is followed by a bibliography and the appendices pertinent to Chapters 5-7.

Part I

Foundations

Chapter 2
The Physics of Collisionless Shocks in Space Plasmas

The central theme of this work is the collisionless shock as manifested in space plasmas. More particularly, we have focused on observations of the terrestrial bow shock and a traveling interplanetary (IP) shock recorded by a constellation of four spacecraft. Here we endeavor to set forth some of the scientific background necessary to an understanding of shocks, beginning with the simpler and more familiar phenomenon of shocks in gas and liquid.

These "everyday" shocks occur in a medium predominantly composed of neutral atoms or molecules, where the transition from an unshocked state to the shocked state is mediated by collisions. In contrast, when shocks occur in a plasma, in which some significant proportion of constituent particles are ionized, long-range field forces begin to compete with collisions in governing the particle dynamics. In a plasma that is sufficiently dilute for collisions to play a negligible role, the interplay of electric and magnetic fields with charged particles gives rise to a range of phenomena inaccessible to a hydrodynamic shock (Burgess, 1995). Nevertheless, some fundamental concepts common to both hydrodynamic shocks and collisionless plasma shocks deserve to be highlighted as such.

From a phenomenological perspective, a shock is a sharp transition between two regimes in the medium. One regime is the unshocked fluid, which is cooler and less dense; in a collisional medium, the flow speed relative to the shock exceeds the sound speed. The second regime, having passed through the shock and emerged on the other side, is warmer and more dense, and its relative flow speed is less than the sound speed (Burgess, 1995). Although this description implies a shock at rest, this need not be the case. A moving shock may plow into the initially stationary medium, which trails along afterwards in the shock's wake, or both medium and shock may have motion relative to an observer (Burgess, 1995). This is often true for spacecraft observations of the bow shock, for instance.

A distinguishing feature of shocks in general is the fact that the relative speed between unshocked medium and shock exceeds the sound speed (or other characteristic speed pertinent to the medium). The consequence of this is that the unshocked medium has no "foreknowledge" of the impending shock, and the transition between fluid regimes is therefore sudden, brief, and tumultuous (Burgess, 1995).

Although both shock and medium may be in motion, it is generally most convenient for the purposes of analysis to transform into a rest frame of the shock. The Normal Incidence Frame (NIF) is common to both hydrodynamic and plasma contexts: here, the bulk flow of the medium is antiparallel to the shock normal. The shock normal is the unit vector perpendicular to the shock front; by convention, the normal points towards the unshocked medium. The unshocked medium is typically referred to as being "upstream" of the shock, while the shocked medium is "downstream" (Burgess, 1995).

Having transformed into an appropriate reference frame such as NIF, one valuable analysis task is to verify conservation between the two fluid regimes. This results in a set of equations known variously as "jump conditions" or the Rankine-Hugoniot (RH) relations, which describe conservation of the flux of mass, momentum, and energy in a hydrodynamic shock (Burgess, 1995; Kallenrode, 2004). In the context of a plasma, these are augmented by Maxwell's equations, and

thus we will reserve the detailed description for later, when we turn to shocks in a collisionless plasma.

There are, further, some shock parameters that are applicable to both hydrodynamics and plasma. The sonic Mach number compares the relative speed between the shock front and the inflowing upstream material to the sound speed of the medium. In a hydrodynamic fluid composed of neutral atoms or molecules, the sound speed is the only characteristic speed to consider, but we will see shortly that a plasma may support additional characteristic speeds, giving rise to other Mach numbers and physical effects (Burgess, 1995). The sonic Mach number and the sound speed will be described later along with the other Mach numbers and speeds of interest in plasma physics.

We now consider what complications arise when the fluid in question is a collisionless, fully-ionized plasma. Ordinarily the transformation of bulk flow energy into thermal energy would be mediated by collisions within the sharp transition region for a hydrodynamic shock, but plasma environments in the heliosphere are often collisionless, with the solar wind supporting a mean free path of ~1AU (1.5×10^8 km), many orders of magnitude greater than the typical length scales of the terrestrial bow shock (Burgess, 1995). Instead, long-range interactions, in which magnetic and electric fields act on the constituent charged particles, take the place of collisions in the transition, which is often called the "ramp" (Baumjohann & Treumann, 2012; Burgess, 1995).

The first line of attack when considering shocks in collisionless plasma is to treat the medium as an MHD fluid. In this description, ions and electrons are subsumed into a single entity, and all intricacies of dissipation are consigned to the ramp, which is assumed to be vanishingly thin. The ramp is thus treated as a discontinuity between two distinct plasma regimes, rather like in the hydrodynamic case. The RH relations now include additional demands of continuity imposed by Maxwell's Equations.

$$\frac{\partial n}{\partial t} + \nabla \cdot (n\boldsymbol{v}) = 0$$

$$\frac{\partial (nm\boldsymbol{v})}{\partial t} + \nabla \cdot (nm\boldsymbol{v}\boldsymbol{v}) = -\nabla \cdot \left(\boldsymbol{P} + \frac{B^2}{2\mu_0} \boldsymbol{I} \right) + \frac{1}{\mu_0} \nabla \cdot (\boldsymbol{B}\boldsymbol{B})$$

$$\frac{\partial \boldsymbol{B}}{\partial t} = \nabla \times (\boldsymbol{v} \times \boldsymbol{B})$$

$$\nabla \cdot \boldsymbol{B} = 0$$

where n is density, $\boldsymbol{v}$ is the velocity vector, m is mass, $\boldsymbol{P}$ is the pressure tensor, $\boldsymbol{B}$ is the magnetic field vector, μ_0 is the permeability of free space, and $\boldsymbol{I}$ is the identity tensor (Baumjohann & Treumann, 2012). In particular, the density, velocity, and mass used above correspond to center-of-mass quantities given by

$$n = \frac{m_e n_e + m_i n_i}{m_e + m_i}$$

$$m = m_e + m_i$$

$$\boldsymbol{v} = \frac{m_e n_e \boldsymbol{v}_e + m_i n_i \boldsymbol{v}_i}{m_e n_e + m_i n_i}$$

where the subscripts e and i indicate electrons and ions, respectively (Baumjohann & Treumann, 2012).

As before, convenience generally requires a shift into a shock rest frame. In a magnetized plasma, we now have another valuable option besides the NIF: the de Hoffmann-Teller Frame (HTF) is defined such that the bulk plasma flow is parallel or anti-parallel to the upstream magnetic field, thereby eliminating any electric field component due to $\boldsymbol{v} \times \boldsymbol{B}$ (see Figure 2.1). Whereas it is always possible to shift into the NIF, a physically appropriate HTF may not necessarily be attainable (Burgess & Scholer, 2015). Assuming a nonrelativistic shock and nonrelativistic bulk flow, the transformation velocity $v_{T,NIF}$ from e.g. the spacecraft frame (SCF) to NIF is simply

$$v_{T,NIF} = \left(v_{sh}, \langle v_{u,y} \rangle, \langle v_{u,z} \rangle\right)$$

where the shock normal is assumed to be along the x-axis for simplicity, v_{sh} is the shock speed, and $\langle v_{u,i} \rangle$ is the average upstream speed along the i-axis. The transformation from SCF to NIF for $\boldsymbol{v}$, $\boldsymbol{B}$, and $\boldsymbol{E}$ is then

$$\boldsymbol{v}_{NIF} = \boldsymbol{v}_{SCF} - \boldsymbol{v}_{T,NIF}$$
$$\boldsymbol{B}_{NIF} = \boldsymbol{B}_{SCF}$$
$$\boldsymbol{E}_{NIF} = \boldsymbol{E}_{SCF} - \boldsymbol{v}_{T,NIF} \times \boldsymbol{B}_{SCF}$$

with the caveat that this operation may prove quite complicated in the context of real observations (Burgess & Scholer, 2015). In contrast, the transformation velocity from SCF or NIF to HTF is dependent upon the shock geometry. As this, too, is a shock-rest frame, the x-component is still tied to the shock speed, but the y and z components together must shift by an amount whose magnitude is

$$v_{HT} = v_u \tan(\theta_{Bn})$$

where v_u is the magnitude of the upstream bulk flow and θ_{Bn} is the angle between the shock normal and the average upstream magnetic field (Burgess & Scholer, 2015). The dependence on $\tan(\theta_{Bn})$ means that v_{HT} may become unmanageably large in more perpendicular shocks. Even a nonrelativistic configuration may require a relativistic transformation, and no HTF is possible if

$$\tan(\theta_{Bn}) \geq {}^{c}/_{v_u}$$

where c is the speed of light (Burgess & Scholer, 2015).

Meanwhile, it is important to note that the RH relations in MHD can be satisfied by discontinuities that are not actually shocks. The equations may be solved by three classes of discontinuity:

1) Mass does not flow along the normal direction. In other words, there is no mixing of the two adjacent plasma regimes under consideration. Two subsets are possible within this classification: *contact discontinuities* and *tangential discontinuities* (Baumjohann & Treumann, 2012). In a contact discontinuity, the normal component of the magnetic field is the same across the boundary, forcing the two regimes to share pressure and tangential components of magnetic field and velocity. Thus, the two plasmas march along together in lockstep on either side of the discontinuous boundary (Baumjohann & Treumann, 2012).

In a tangential discontinuity, the magnetic field's normal component is zero. Here, the plasmas on either side of the discontinuity need not match each other's tangential magnetic field or velocity components. They may slide freely and independently past each other, as long as pressure balance across the boundary is preserved (Baumjohann & Treumann, 2012).

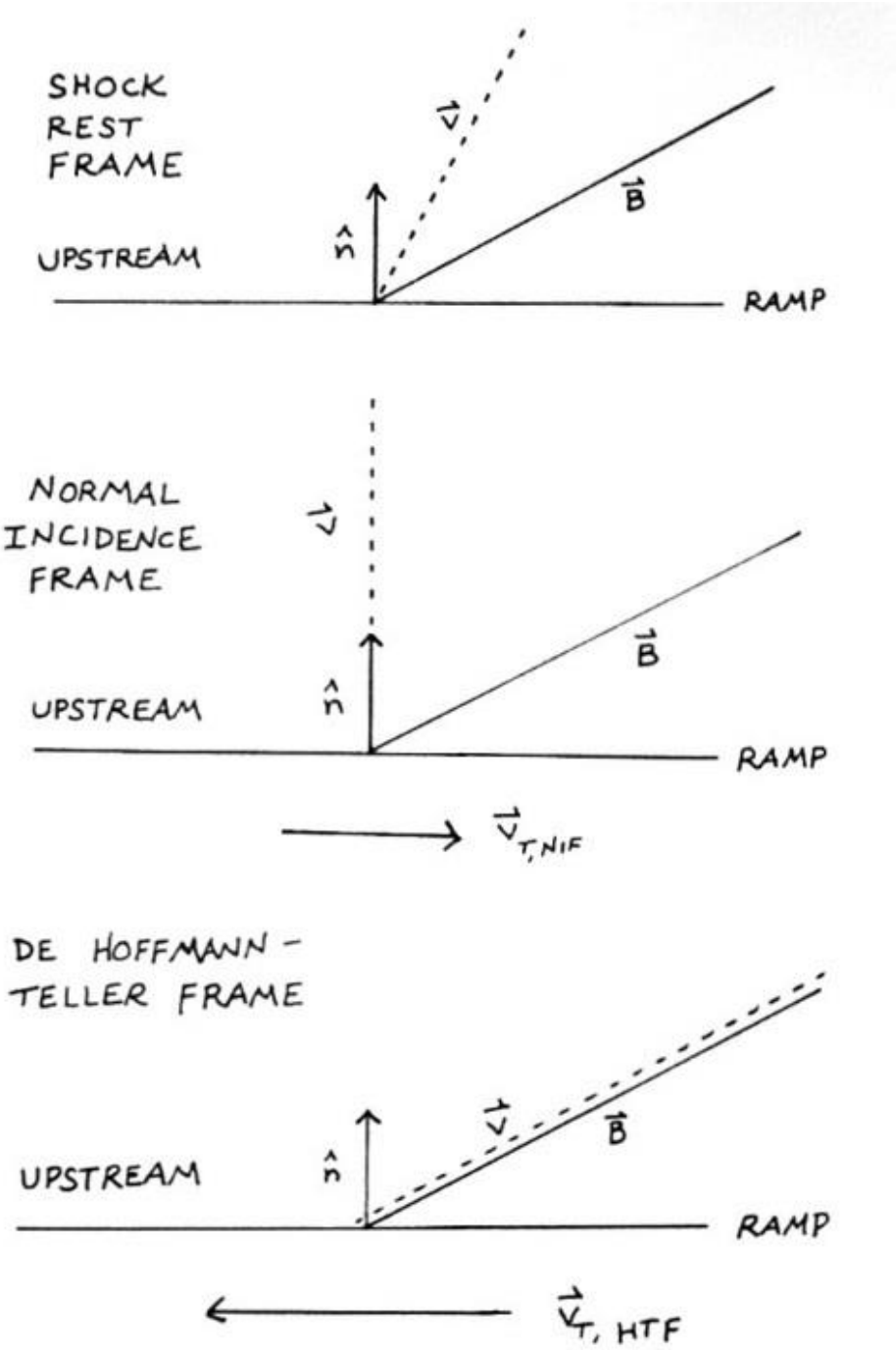

Figure 2.1. Reference frames. The horizontal line in each frame represents the ramp, above which is the upstream region. The shock normal and magnetic field vectors are the same from frame to frame. Top: an example of a shock in its most simple rest frame. Center: the rest-frame shock has been shifted to the NIF; the flow is parallel to the normal. A vector indicating the direction of the NIF transformation velocity is shown beneath the ramp. Bottom: the rest-frame shock has been shifted to the HTF; the flow is parallel to the magnetic field. A vector indicating the direction of the HTF transformation velocity is shown beneath the ramp; its length is

approximately representative of its relationship to the NIF transformation velocity for this example.

2) Another class, known as *rotational discontinuities*, is distinguished by constant, nonzero mass flow normal to the boundary. In contrast to the previous case, we see a continuous migration of material from one plasma region to its neighbor. However, as the mass flow undergoes no change, the two regions must have the same density (Baumjohann & Treumann, 2012). The domino effect on the conservation relations thus mandates constant normal components of both magnetic field and velocity. A curious consequence of the jump conditions for this type of discontinuity is that the tangential magnetic field and velocity rotate by the same angle across the boundary, while pressure and temperature do not change. Thus there is no change to the entropy (Baumjohann & Treumann, 2012).

3) The third discontinuity class must therefore be the phenomenon we are most eagerly interested in: shocks. In the case of fast-mode shocks, which are the most relevant to our studies, we are dealing with nonzero mass flow, accompanied by an increase in density and commensurate drop in normal velocity across the boundary (Baumjohann & Treumann, 2012).

We have so far eschewed a rapid-fire listing of the most common and useful shock parameters, but now that we have navigated safely through hydrodynamic shocks, into the realm of MHD plasmas, past related but here irrelevant discontinuities, and finally into the teeming sea of collisionless shocks, we may as well pause to orient ourselves.

Many parameters of importance are defined with respect to the shock normal, which we have already touched upon briefly. This unit vector, indicating the direction perpendicular to the surface of the shock front and conventionally pointing upstream, may remain unchanged over a wide spatial scale, where the assumption of a planar shock front is valid (Baumjohann & Treumann, 2012). Alternatively, and as we shall see later in this work where we discuss real observations, the shock normal may be a more localized entity if the shock front deviates from planarity over the scales of interest. In the latter case, as the applicability of a given shock normal is limited, so too is the applicability of other parameters that depend upon it.

Another important parameter we have already referenced is the shock angle θ_{Bn}, or the acute angle between the shock normal and the average upstream magnetic field vector (see Figure 2.1). This angle roughly determines typical behaviors and dynamics evident in and near the shock. On the most basic level, shocks are thereby sorted into quasi-parallel ($\theta_{Bn} \leq 45°$) and quasi-perpendicular ($\theta_{Bn} \geq 45°$) (Burgess, 1995). Further distinctions may be made by identifying parallel and perpendicular shocks; so-called oblique shocks fall somewhere in the middle, with conflicting opinions as to where the boundaries may be said to lie (Burgess, 1995; Burgess & Scholer, 2015; Kallenrode, 2004). This fundamental geometry of the shock will be seen to affect the particle dynamics and wave propagation surrounding the shock.

Also essential is the shock speed: this and the shock normal are both necessary to shift into the rest frame of the shock, although determining the shock speed and shock normal in the context of real observations may be far from simple. (Methods and possible pitfalls will be discussed in Chapter 3.) Once in the shock rest frame, one can obtain the upstream average bulk velocity and speed of material flowing into the shock (v_u, generally for ions if one is interested in the solar wind). The upstream inflow speed yields Mach numbers when compared to characteristic speeds of the plasma; the Mach numbers, like θ_{Bn}, can be used to loosely categorize the shock.

Previously, when we were considering properties of a hydrodynamic shock, we mentioned that the sonic Mach number was the ratio between the inflow speed and the sound speed. We can

calculate the sonic Mach number for a collisionless shock in plasma, but the Alfvén and fast magnetosonic Mach numbers are arguably more valuable (Baumjohann & Treumann, 2012; Burgess 1995; Burgess & Scholer, 2015; Kallenrode, 2004). Let us consider these three characteristic speeds for a representative plasma: the sound, Alfvén, and fast magnetosonic speeds.

The chief contributor to the sound speed c_s is thermal energy:

$$c_s^2 = \frac{\gamma p}{n m_i} = \frac{\gamma k_B T}{m_i}$$

where γ is the polytropic index, often assumed to be 5/3 (appropriate for an ideal monatomic gas) in the solar wind; k_B is Boltzmann's constant; p is the thermal pressure; n is the density; m_i is the ion mass; and T is the particle temperature (Baumjohann & Treumann, 2012).

In contrast, the Alfvén speed c_A depends on the magnetic energy present in the plasma (Baumjohann & Treumann, 2012):

$$c_A^2 = \frac{B^2}{\mu_0 n m_i}$$

where B is the magnetic field magnitude and μ_0 is the permeability of free space.

The fast magnetosonic speed c_{ms} unites contributions from both thermal and magnetic energy (Baumjohann & Treumann, 2012):

$$c_{ms}^2 = c_s^2 + c_A^2$$

and the corresponding sonic, Alfvénic, and fast magnetosonic Mach numbers (M_s, M_A, and M_{ms}, respectively) are simply formed by taking the ratios with upstream bulk flow speed in the shock rest frame: $M_s = \frac{v_u}{c_s}$, and so on (Baumjohann & Treumann, 2012).

We remarked previously that a hydrodynamic shock is characterized by supersonic upstream bulk flow with a sharp transition to subsonic bulk flow downstream. For a plasma shock, we can generalize this requirement and say that the upstream bulk speed must exceed the upstream Alfvén and fast magnetosonic speeds as well. The shocks of interest to our study will be of the type known as "supercritical", but for the sake of completeness it is worthwhile to mention their tamer counterparts as well. The division between subcritical and supercritical shocks is determined by the so-called "critical Mach number", but a complication arises because the critical Mach number is neither a concrete number nor a well-defined analytical expression. Instead, the critical Mach number may be estimated from the RH relations by assuming a downstream Mach number of $M = 1$, just on the threshold between pre-shocked (unshocked) and post-transition (shocked). Depending upon the unique plasma parameters, the critical Mach number will be some low value less than 3 (Baumjohann & Treumann, 2012).

A subcritical shock will exhibit a less complex range of behaviors within and surrounding the ramp. This is because the subcritical shocks are able to convert incoming flow energy into thermal energy almost exclusively by means of dissipation within the ramp, possibly with some assistance from dispersion by escaping waves (Burgess & Scholer, 2015). Above the critical Mach number, these avenues no longer suffice to dispose of the excess energy. Indeed, subcritical shocks are exceedingly rare in the heliosphere, especially in the case of Earth's bow shock, which has been observed to be reliably supercritical (Burgess & Scholer, 2015). We will return and discuss features of supercritical shocks after we dispose of a few more shock parameters.

The ratio of Alfvén speed to the speed of light is another oft-quoted parameter, which, however, has no specific name to distinguish it. It may help to convey the extent to which a shock is subject to relativistic dynamics: multiplying by the Alfvén Mach number would give the relativistic β value

$$\beta = M_A \frac{c_A}{c} = \frac{v_u}{c}$$

not to be confused with plasma β, which we will turn to presently.

Average plasma parameters in the distinct upstream and downstream regions are also of value: not just the magnetic field, but also numerous plasma moments. These include the ion and electron density n_i and n_e, presumed equal in quasi-neutral space plasmas; ion and electron temperatures T_i and T_e, preferably available separated into parallel and perpendicular components; ion and electron velocities v_i and v_e; and ion and electron pressures p_i and p_e, if possible also split into parallel and perpendicular components. All of these are quantities that, under favorable circumstances, one could expect to obtain as direct measurements from space instruments. Given these, other useful quantities may be calculated, such as the ion or electron plasma beta β_i or β_e, which is the ratio of thermal versus magnetic pressure:

$$\beta_s = \frac{2\mu_0 p_s}{B^2}$$

where the species subscript s should be replaced by i or e for ions or electrons respectively, as the case may require (Baumjohann & Treumann, 2012).

All that is needed in order to compute the ion and electron plasma frequencies ω_{pi} and ω_{pe} is the density:

$$\omega_{ps}^2 = \frac{q_s^2 n_s}{\epsilon_0 m_s}$$

where the species subscript s should be replaced by i or e for ions or electrons respectively and ϵ_0 is the vacuum permittivity (Baumjohann & Treumann, 2012). Given an electron-proton plasma abiding by quasi-neutrality, we expect the electron plasma frequency to exceed the ion plasma frequency by their mass ratio $\sqrt{1836}$.

Armed with the plasma frequencies, we can compute the inertial length of each species, $d_s = \omega_{ps}/c$, where c is the speed of light (Baumjohann & Treumann, 2012). We generally expect the transition layer of a collisionless shock to be comparable in scale to the ion inertial length (Burgess & Scholer, 2015). Similarly, features associated with ion reflection in quasi-perpendicular shocks are often limited by the ion gyroradius, with the gyroradius r_{gs} for a species s determined by

$$r_{gs} = \frac{m_s v_{\perp s}}{|q_s| B} = \frac{v_{\perp s}}{\omega_{gs}}$$

where $v_{\perp s}$ is the velocity component perpendicular to the magnetic field direction and ω_{gs} is the gyrofrequency (Baumjohann & Treumann, 2012).

Having all the above parameters to hand gives us a fairly well-rounded picture of the shock's general character. The shock angle allows us to siphon quasi-parallel shocks into one category and quasi-perpendicular shocks into another. We can also look at the way the shock angle changes from upstream to downstream: "fast" shocks experience an increase of the shock angle after passage of the ramp, meaning that the magnetic field has bent farther away from alignment with the shock normal. The opposite case can occur as well, with the downstream magnetic field being more closely aligned with the shock normal in a "slow" shock, but fast shocks are far more prevalent in the heliosphere (Baumjohann & Treumann, 2012; Burgess, 1995).

The distinction between quasi-parallel and quasi-perpendicular shocks is more than a mere exercise in academic taxonomy. The specific angle between the magnetic field and the shock front is associated with observable differences in structure surrounding the ramp. This is because the

motion of charged particles in and near the shock, while ostensibly controlled by the long-range fields, also impacts those fields in return.

We said earlier that dissipation internal to the shock transition suffices for subcritical shocks. These, however, are rare in the Earth's bow shock (Burgess, 1995), which is the consuming topic of interest for our analyses later. For supercritical shocks, ion reflection constitutes a major avenue for the necessary dissipation. In the case of quasi-parallel shocks, where the magnetic field lines stretch almost directly forth from the shock front like a highway, reflecting ions find a relatively easy escape route away from the shock (see Figure 2.2). As a result, they may travel significant distances from the ramp, creating an interesting region of turmoil known as a foreshock (Baumjohann & Treumann, 2012; Burgess & Scholer, 2015). Indeed, it becomes next to impossible to define a clear, unambiguous shock front for a quasi-parallel shock.

In general, the transition of states as mediated by the quasi-parallel shock is gradual, contrary to the ideal MHD paradigm of a sharp discontinuity. Where escaping particles flow against the bulk of the upstream plasma, they may spawn instabilities and turbulence that further disrupt the oncoming river of plasma (Baumjohann & Treumann, 2012).

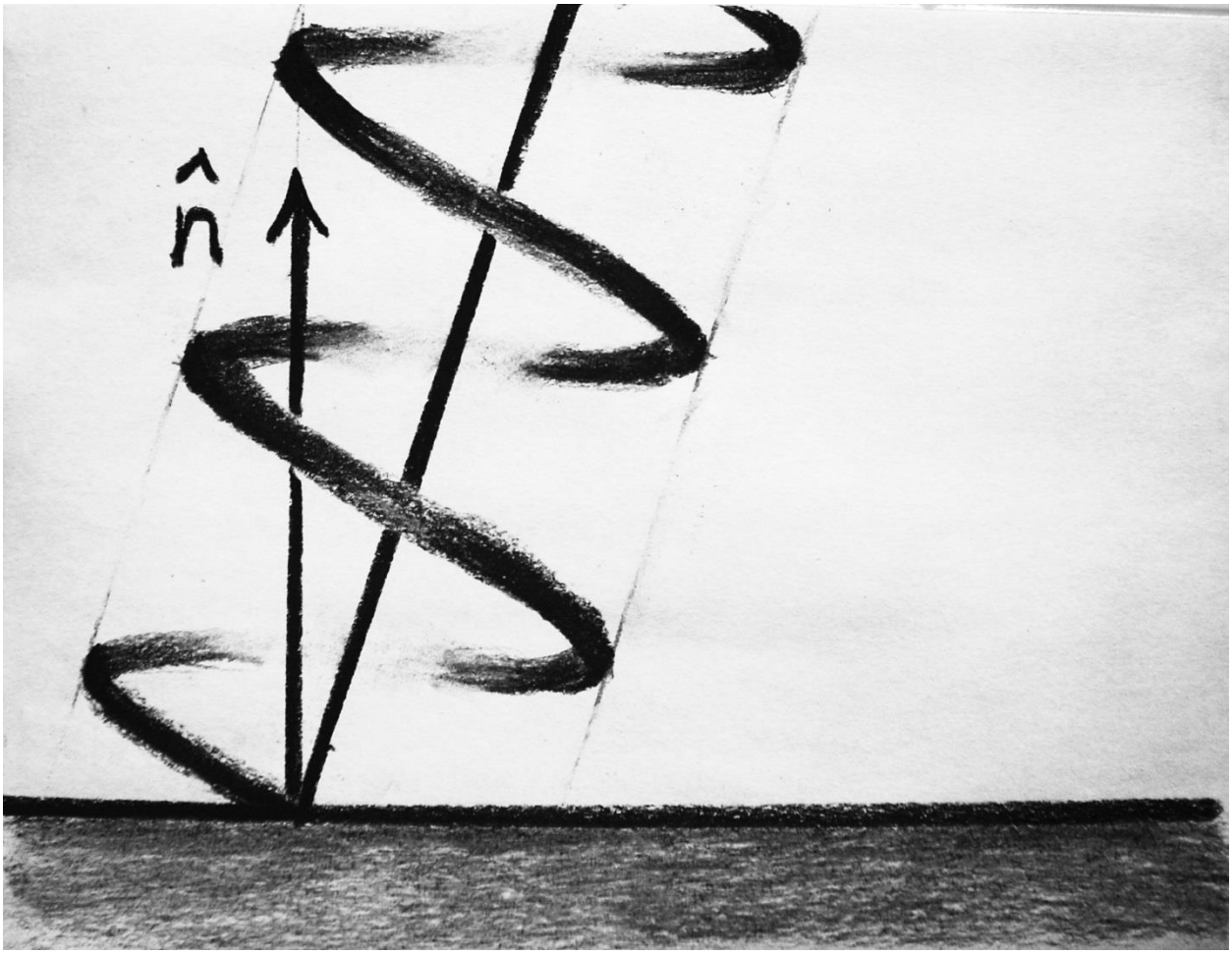

Figure 2.2. Artist's rendition of the trajectory of an ion reflecting off a quasi-parallel shock front, whence it may escape by gyrating back up the magnetic field line as shown. The straight, diagonal black line represents the direction of the upstream magnetic field, while the shaded region represents the shock front. (Figure inspired by Burgess (1995).)

We are not so plagued by ambiguities when we turn our attention back to the quasi-perpendicular shocks. The geometric relationship between the magnetic field lines and the shock front is such that ions attempting to flee back upstream must travel much farther along the confining magnetic field lines before the shock front is out of reach of the ions' gyrations (see Figure 2.3). Consequently, ions are more vulnerable to gyrating back into the furiously roiling shock transition layer, and fewer of them succeed in escaping beyond the range of their own gyroradii (Burgess, 1995). While the supercritical quasi-perpendicular shock does feature a region of turbulence and reflected ions upstream of the ramp like the quasi-parallel shock does, this region in the quasi-perpendicular case is far more limited in spatial extent, being generally of the order of an ion gyroradius or less. Because the fluctuating magnetic field exhibits a rise from the upstream average magnitude prior to the sharp increase in the ramp, this region is known as the "foot" (Baumjohann & Treumann, 2012; Burgess, 1995; Burgess & Scholer, 2015).

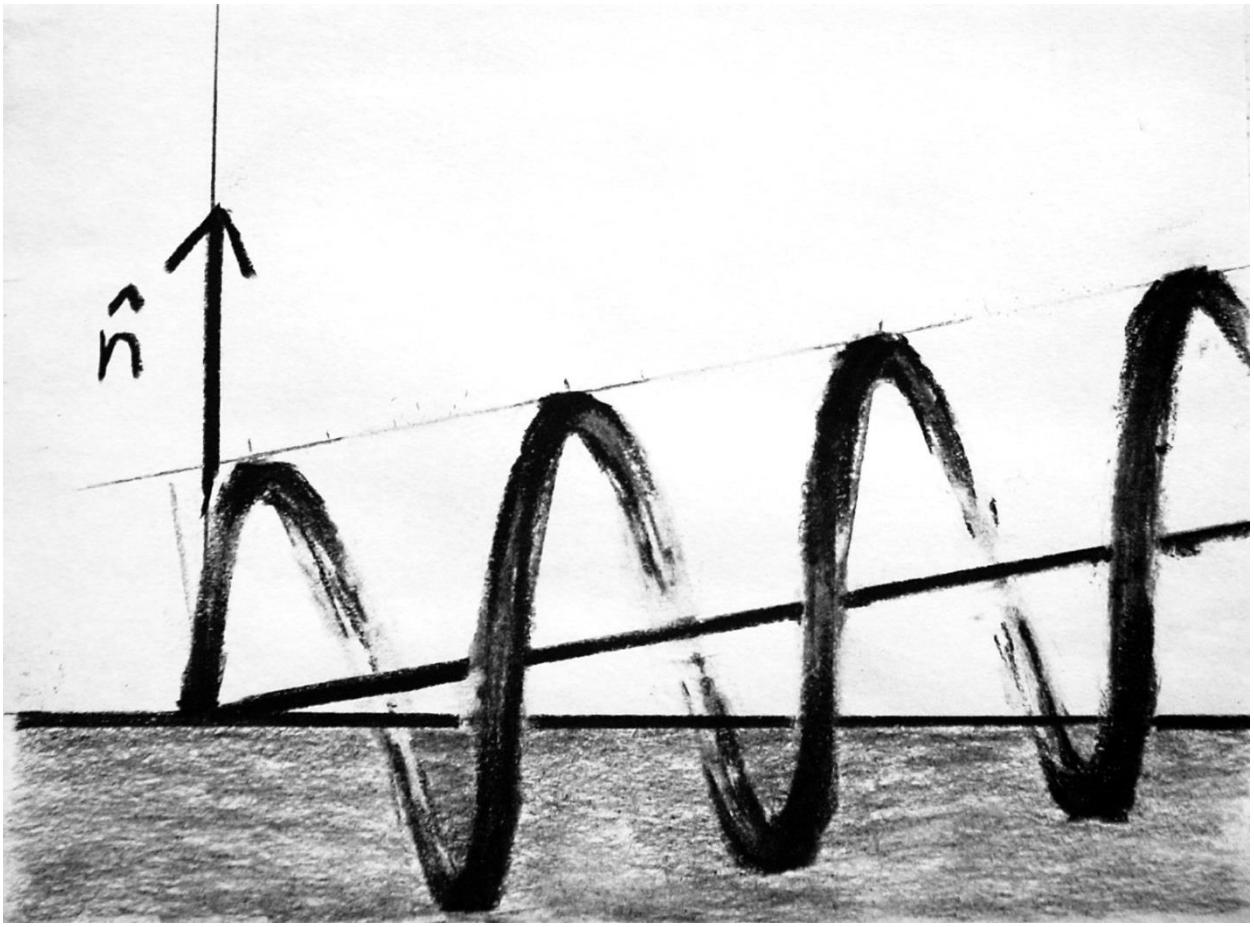

Figure 2.3. Artist's rendition of the trajectory of an ion reflecting off a quasi-perpendicular shock front. As in Figure 2.2, the shock normal is labeled, the diagonal black line indicates the magnetic field direction, and the shaded region represents the shock front. Notice that this ion has a similar pitch angle to the ion in Figure 2.2, and its gyrating path leads it repeatedly back to the shock front, whence it may not escape again. (Acceleration effects are not represented here. Figure inspired by Burgess (1995).)

Whereas the scale of the foot is typically comparable to an ion gyroradius, the ramp, which accounts for the greater share of the magnetic field's jump from upstream to downstream magnitudes, occupies a smaller scale length on the order of the ion inertial length (Burgess & Scholer, 2015). In sufficiently strong shocks, another agitated region called the "overshoot", also spanning about an ion gyroradius, may immediately follow downstream of the ramp before the magnetic field relaxes into a more quiescent downstream state. Alternatively, the heightened magnetic field in the overshoot may be followed by a similar-scaled region of depressed field called the "undershoot"; in some cases, a repeating cycle of over- and undershoots may be observed before the magnetic field settles into its equilibrium downstream behavior (see Figure 2.4) (Burgess, 1995). Ion reflection being modest or absent in a subcritical shock, these features (foot, overshoot, and undershoot) are not expected to be present.

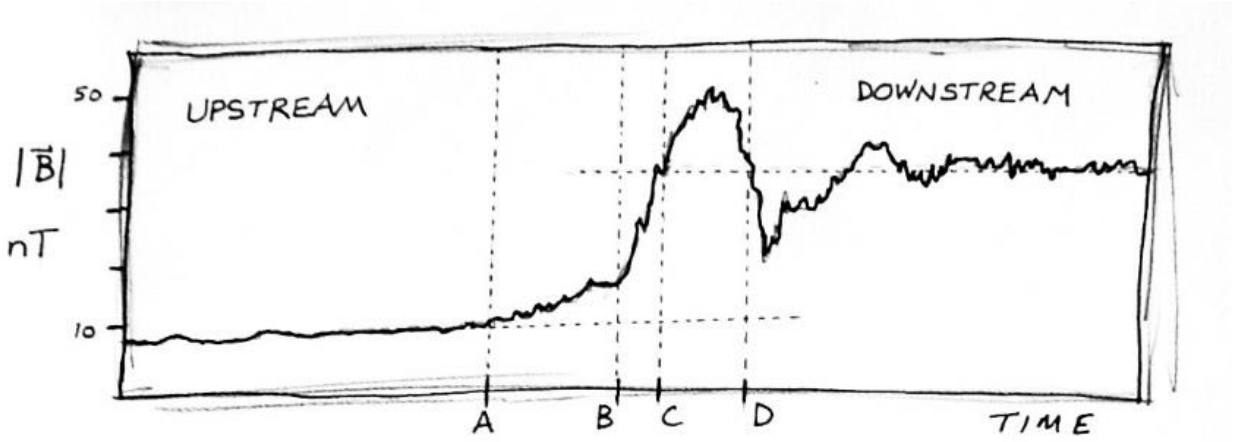

Figure 2.4. Rough sketch of the magnetic field profile of an imaginary, but fairly typical, quasi-perpendicular shock. The horizontal axis represents time while the vertical axis gives the magnetic field magnitude in units of nT. This is the sort of profile you might expect to see in bow shock data. Features of interest are bounded by letters: (AB) foot, where ion reflection is expected to be most active; (BC) ramp, the sharpest increase of the transition; and (CD) overshoot, followed by a more zealous undershoot than the artist should perhaps have hazarded. (Figure inspired by floods of real data and by a figure in Burgess and Scholar (2015).)

Naturally, the realm of collisionless shocks encompasses an enormous range of phenomena occurring in nature or in the laboratory. To some extent, space physicists are fortunate enough to have the best of both worlds: while our regions and phenomena of interest may often be far beyond the scope of the laboratory, we are still able to collect direct measurements with the help of spacecraft sent into the plasmas we wish to study.

One of the most faithful collisionless shocks within reach is part of the armor protecting life on Earth from the potentially dangerous tantrums of the Sun: the bow shock forms at the interface where the solar wind is deflected to flow around the Earth's magnetosphere. Earth-orbiting satellites of sufficient apogee may routinely pass from the magnetosphere to the solar

wind, obligatorily crossing the bow shock in the process. Solar wind and bow shock measurements formed an important part of the early evidence that plasmas are able to sustain shocks in spite of a negligible collision frequency (Axford, 1962; Kellogg, 1962; Kennel et al., 1985).

Planetary bow shocks in the heliosphere are an example of shocks formed by fast flow past a stationary obstacle. The solar wind is both supersonic and super-Alfvénic, so that the orbiting planets present a nasty surprise when they appear suddenly in its path. Precisely what constitutes the obstacle varies from one planet to another, depending on their magnetic properties, but in the case of the Earth it is our magnetosphere that the solar wind piles up against and is deflected around (Walker & Russell, 1995).

As the magnetosphere is not a rigid boundary but can "bounce" a little as the ram pressure of the solar wind varies, so too the precise shapes and positions of the magnetopause, magnetosheath, and bow shock will also vary. Their general shape is bullet-like, as the solar wind's dynamic pressure compresses the magnetosphere on the dayside, eases up while deflecting towards dawn and dusk, and "drags" the magnetosphere backwards to form the long magnetotail on the nightside (Burgess & Scholer, 2015; Walker & Russell, 1995). While the magnetotail may extend outward several hundreds of Earth radii (R_E) (Hughes, 1995), the dayside magnetopause generally hovers around 15 R_E of Earth, with the "subsolar" bow shock around 20 R_E (Burgess & Scholer, 2015). The moon, which orbits Earth at a distance of 60 R_E, routinely passes from the magnetosphere to the solar wind and back every orbit (Luhmann, 1995).

Because the direction of the magnetic field frozen into the solar wind is fairly constant, whereas the direction of the shock normal varies up to 135° between Earth's dawn and dusk regions, a huge variety of shock angles may be observed (see Figure 2.5) (Baumjohann & Treumann, 2012). From dawn to noon MLT (Magnetic Local Time), the bow shock is most typically quasi-parallel because the interplanetary magnetic field at 1AU is usually directed ~45° dawnward from the Sun-Earth line. Noon to dusk, in contrast, tends to be quasi-perpendicular (Burgess, 1995; Burgess & Scholer 2015; Kallenrode, 2004). Furthermore, the bow shock is almost invariably supercritical, with the result that reflected particles are observed throughout. In the quasi-perpendicular regions of the bow shock, the archetypal features previously described are often seen: the ramp is often preceded by a foot, where reflected ions gyrate, and may be followed by an overshoot (Baumjohann & Treumann, 2012; Kennel et al., 1985). As expected, in the bow shock's quasi-parallel regions, reflected particles escape easily and stream back into the solar wind so far that the foreshock can extend beyond the lunar orbit (Burgess, 1995).

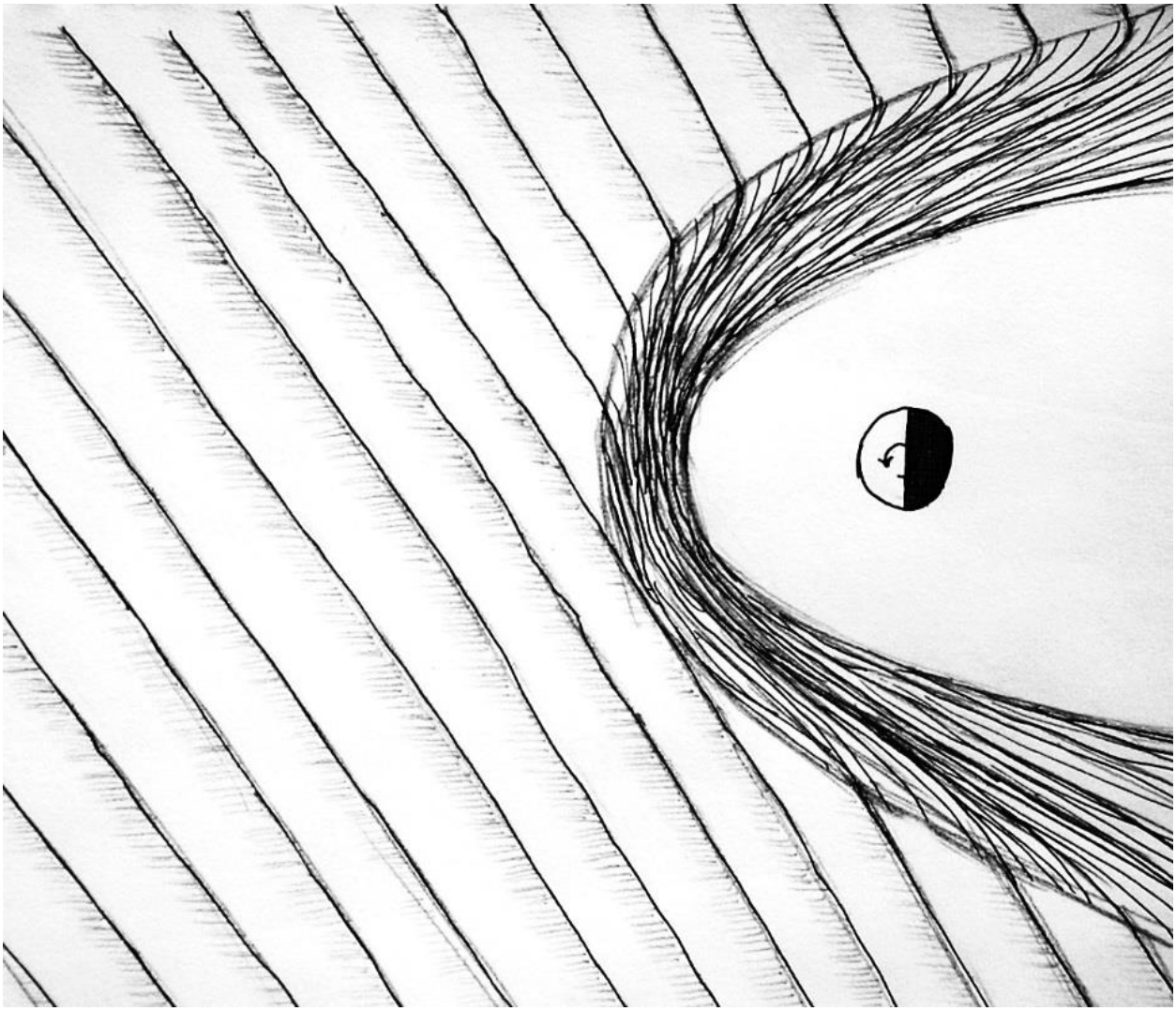

Figure 2.5. Artist's rendition of the interaction between solar wind and terrestrial magnetosphere (not to scale). The view is of the ecliptic plane, and the Earth's direction of rotation is indicted by a curving arrow. The solar wind flows in from the left, carrying the frozen-in magnetic field lines with it. By the time the solar wind reaches the Earth, the magnetic field tilts approximately 45° clockwise from the Earth-Sun line (horizontal direction). The piling of magnetic field lines in front of the magnetosphere is shown; the bow shock forms at the outermost edge of this pile-up. Before noon MLT, the bow shock tends to be quasi-parallel, while it is usually quasi-perpendicular after noon MLT. (Figure inspired by Kallenrode (2004) and Burgess and Scholar (2015).)

The foreshock itself is not a homogeneous region but has one area dominated by reflected ions, while the area nearer the Sun is dominated by electrons (see Figure 2.6). This is because regions of the bow shock closer to noon than to dawn become less quasi-parallel: reflected ions have increasing difficulty escaping from the shock front in such regions and need higher energies in order to do so, whereas reflected electrons are still easily able to stream back up the magnetic field lines (Burgess, 1995). To add to the complications attending this region of space, waves and particles that penetrate even a little way upstream along the IMF from marginally quasi-

perpendicular regions may be subsequently convected by the solar wind bulk flow into foreshock regions. Thus, it is possible that some areas of the foreshock contain particles and waves that actually originated in the quasi-perpendicular bow shock (Burgess & Scholer, 2015).

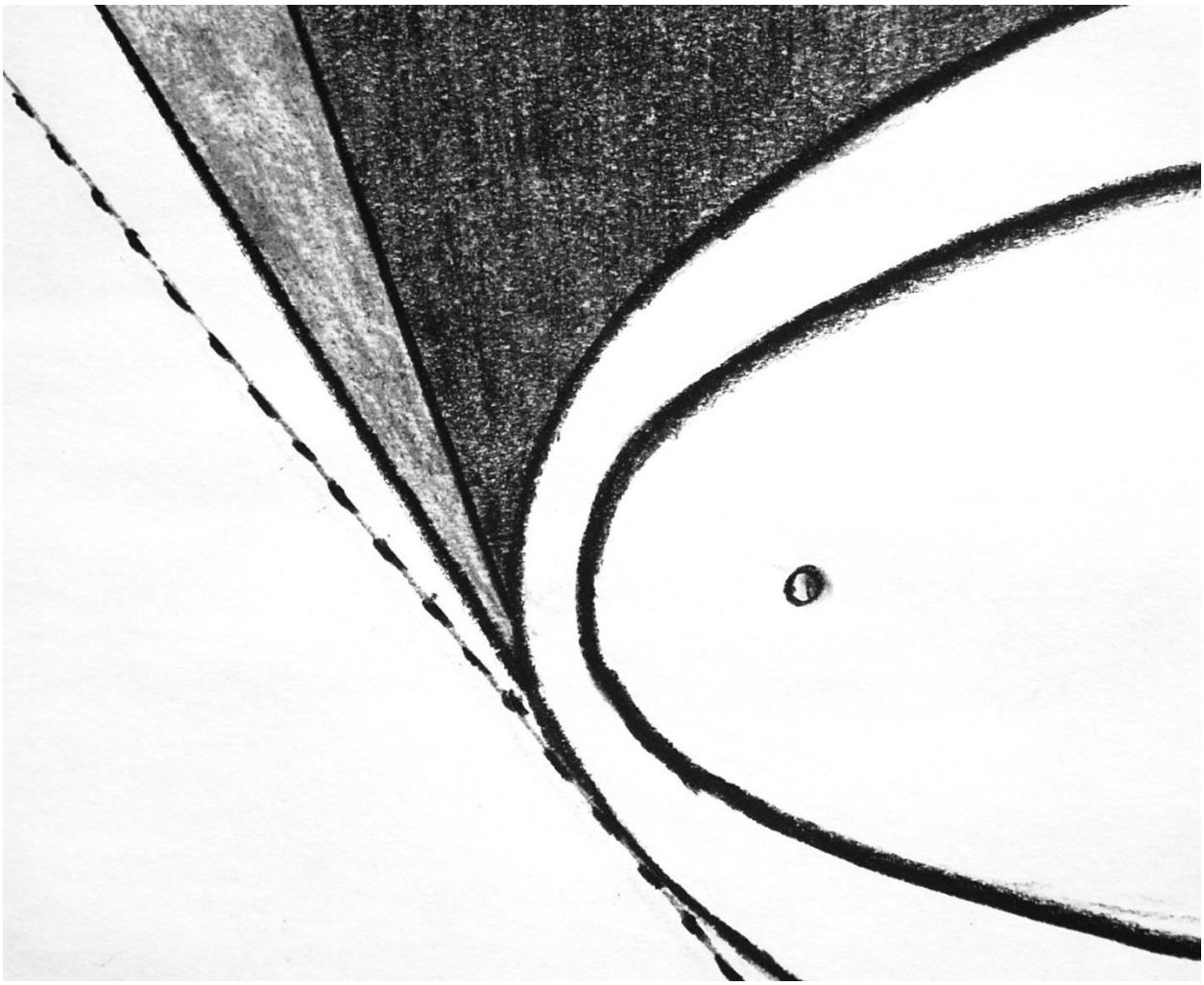

Figure 2.6. Artist's rendition of the electron and ion regions of the foreshock. The dashed straight line shows the tangent magnetic field line. The outer curve is the bow shock, and the inner curve is the magnetosphere. The darkest shaded region is the ion foreshock, while the lighter shaded region is the electron foreshock. Precise positions and relationships are naturally dependent on changing environmental conditions. (Figure adapted from Burgess (1995).)

Early observational studies of the bow shock rarely had the benefit of multiple spacecraft flying as a single constellation, which makes deduction of the shock normal simpler and more accurate (Bale et al., 2005). Consequently, numerous models were developed to estimate the bow shock shape and position, given a set of observed parameters of the solar wind and magnetosphere. We will elaborate further on this topic in Chapter 3. For now, suffice it to say that solar wind speed and dynamic pressure, the position of the observed bow shock crossing, and the orbital motion of Earth have often been taken into account in order to compute a reasonable estimate of the bow

shock normal vector. This does not account for the possibility of small-scale, local perturbations that may appear in the shock front due to rippling or reformation (Schwartz, 1998).

Spacecraft observations of Earth's bow shock result not from transit of spacecraft through a sluggish shock but from the sweeping passage of the shock across the spacecraft. Indeed, compared to typical bow shock speeds in the tens of km/s, a spacecraft orbiting Earth at a few km/s moves negligibly slowly (Burgess & Scholer, 2015).

Less reliable than the bow shock but equally interesting are the IP shocks that occasionally propagate outward through the heliosphere. These may be generated ahead of coronal mass ejections (CMEs) from the Sun or at the boundary where a fast solar wind stream, issuing forth behind a slower stream as the Sun rotates, overtakes the slower-moving material, causing a pile-up (see Figure 2.7). Such encounters between solar wind streams are known as co-rotating interaction regions (CIRs) and may involve a pair of shocks, one on either side of the interface (Burgess & Scholer, 2015). Upon leaving the Sun, a garden-variety CME (and any shock it may drive) has a radius of curvature much larger than that of Earth's bow shock (Kallenrode, 2004). The difference is even more striking in the case of IP shocks in CIRs, which satisfy the assumption of a planar shock front much more readily than the smaller, more curved bow shock (Burgess & Scholer, 2015; Kallenrode, 2004).

With origins even more dramatic than those of the bow shock, IP shocks are generally observed to move much faster as well. CME speeds may be as high as 2000 km/s, though speeds near 300 km/s are typical (Kallenrode, 2004). CIR-spawned IP shocks move at speeds comparable to the fast solar wind stream driving them, say several hundred km/s (Kallenrode, 2004). The IP shock discussed in our observational analyses to follow was unusual for a shock caused by a CIR because its speed was rather low, 330 km/s.

Having thus familiarized ourselves with the most basic foundations of shock physics, including some notes about shocks found in the heliosphere, we close here. It will next be important to consider techniques necessary for the unraveling and analysis of shock observations.

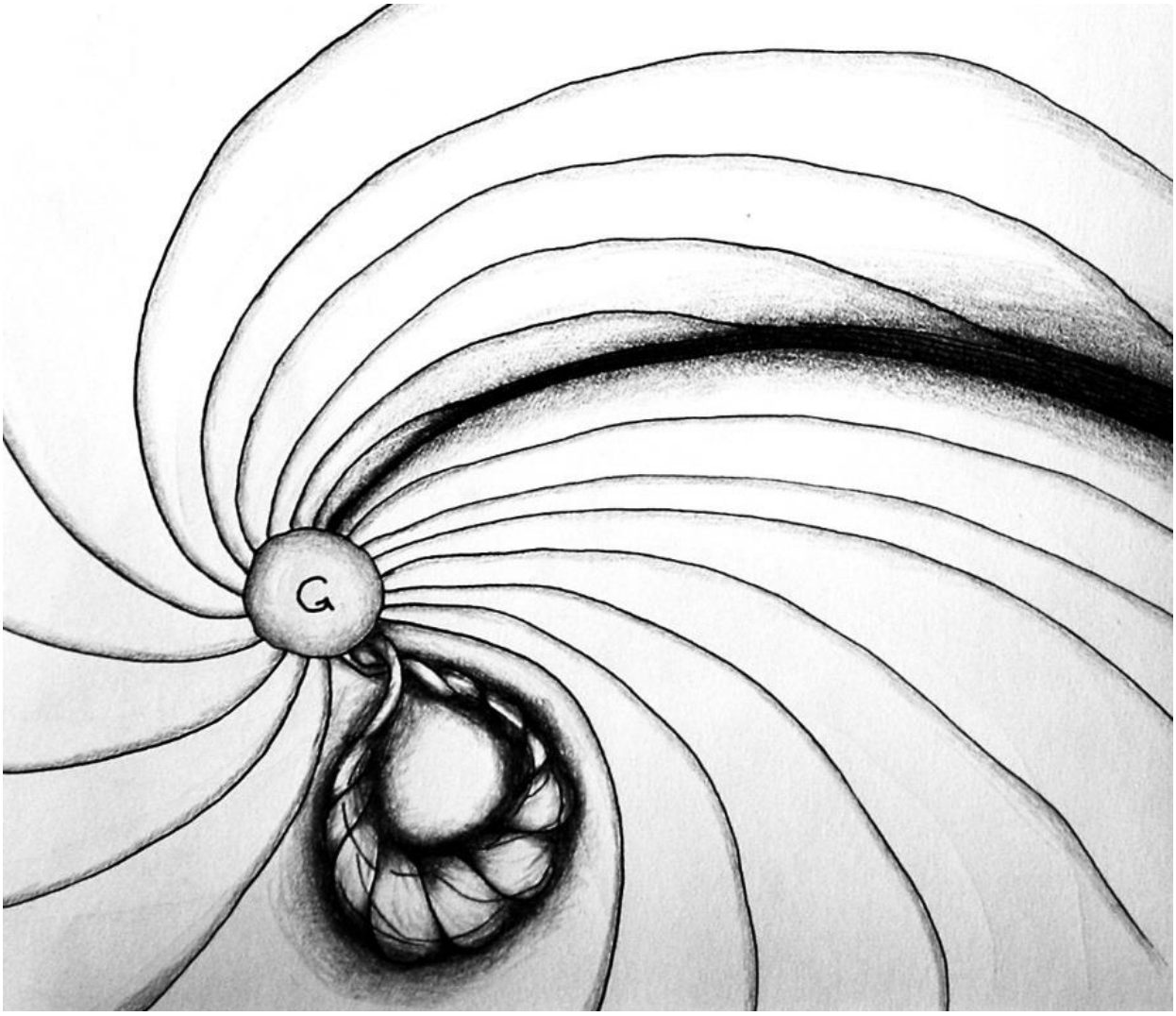

Figure 2.7. Artist's rendition of solar activity that may give rise to shocks. Here we are looking down at the ecliptic plane. The Sun is left of center, marked with a curved arrow to indicate its direction of rotation. A fast solar wind stream exiting the upper right quadrant of the Sun is overtaking the slower material ahead of it, forming a CIR. From the lower right quadrant of the Sun, a CME is emerging dramatically. (Figure inspired by Burgess and Scholar (2015).)

Part II

Experimental and Data Analysis Techniques

Chapter 3
Processing Techniques for Deriving Shock Parameters from Single- and Multi-Point Plasma Measurements

3.1 Determining the shock normal

The first step in any confrontation with real data from a shock observed in space is to take one's bearings, and for this the critical task is to determine the shock normal. Unless one is solely concerned with microphysics, much analysis depends on this; even those whose main subject is microphysics will likely need to provide this information to help readers place the shock in context. While determination of the shock normal is no insignificant hurdle, there are at least a few options to choose from in attacking the problem.

3.1.1 Variance analysis

Minimum (Maximum) Variance Analysis (MVA) of the magnetic (electric) field involves identifying the orthogonal directions of the maximum, intermediate, and minimum change in three-dimensional vector data across a discontinuity. Analysis of the magnetic field data is more common as these measurements are more frequently available. At least three vectors are required for this method – or two vectors and some reasonable constraining assumption – generally consisting of a vector before, within, and after the discontinuity. Where small-scale fluctuations in the observed magnetic field seem likely to obscure the macroscopic behavior, a larger number of measurements can be included in the computation, which is simply an optimization problem (Sonnerup & Scheible, 1998).

The origin of this method lies in an ideal model where the discontinuity is solely one-dimensional. There, due to the requirement $\nabla \cdot \boldsymbol{B} = 0$, the component of $\boldsymbol{B}$ normal to the discontinuity cannot sustain any spatial or temporal gradient. (Similarly, the electric field must have its maximum variance in the shock-normal direction.) In reality, one cannot expect zero variance, but identification of the minimum variance direction for the magnetic field, or equivalently the maximum variance direction for the electric field, should more or less capture the direction of the shock normal as well.

In order to apply this method to real data, we resort to matrices. Here we closely follow the procedure set forth by Sonnerup and Scheible (1998). The end goal is to find the unit vector $\boldsymbol{n}$ that minimizes the variance σ^2:

$$\sigma^2 = \frac{1}{M}\sum_{m=1}^{M}[|(\boldsymbol{B}^m - \langle \boldsymbol{B} \rangle) \cdot \boldsymbol{n}|^2]$$

where the superscript m indicates one of a total number M measurements of the 3D magnetic field $\boldsymbol{B}$, and the average magnetic field $\langle \boldsymbol{B} \rangle$ has been computed as

$$\langle \boldsymbol{B} \rangle = \frac{1}{M}\sum_{m=1}^{M}[\boldsymbol{B}^m]$$

This goal is achieved by computing the variance matrix elements $M_{\mu\nu}$ for each pair of Cartesian coordinates $\mu, \nu = 1,2,3$ or x, y, z:

$$M_{\mu\nu} = \langle B_\mu B_\nu \rangle - \langle B_\mu \rangle \langle B_\nu \rangle$$

having computed the appropriate averages according to the definition above (Sonnerup & Scheible, 1998). It is then necessary to solve the eigenvalue/vector equations for each component μ:

$$\lambda n_\mu = \sum_{\nu=1}^{3} M_{\mu\nu} n_\nu$$

The results of this calculation are three orthogonal eigenvectors $\boldsymbol{x}_i$, corresponding to the minimum, intermediate, and maximum variance directions, and their associated eigenvalues λ_i. The eigenvalues are the variance values along each eigenvector $\boldsymbol{x}_i$ (Sonnerup & Scheible, 1998).

As mentioned, although most of the description above refers to magnetic field measurements, the same procedure may be performed on electric field measurements, if they are available and reliable. The main difference lies in the fact that the maximum variance of the electric field should provide the shock normal, whereas for the magnetic field this should be the minimum variance direction. In the best possible outcome, the variance analysis will yield three equally useful direction vectors, which can provide a convenient coordinate system in which to process the shock measurements. Certainty in the variance vectors is partly reflected in their eigenvalues; if these differ markedly, i.e. if $\lambda_{min} \ll \lambda_{mid} \ll \lambda_{max}$, the direction vectors are well determined (Sonnerup & Scheible, 1998).

Unfortunately, it often turns out that only the maximum variance direction is clearly defined, while the minimum and intermediate eigenvalues may differ by a factor of only 2-3, leaving the minimum variance direction rather uncertain. In this regard, analysis of the electric field may offer some advantage because the shock normal direction should be aligned with the less ambiguously determined maximum variance direction.

One conspicuous shortcoming of MVA, besides the ambiguous answers it may give, is the fact that it only provides the shock normal direction; it does not give the shock speed, which is necessary in order to access any shock rest frame.

3.1.2 Rankine-Hugoniot (RH) analysis

RH analysis was introduced briefly in the previous chapter, where we noted that it arose from requiring conservation laws to be satisfied across the shock, assumed to be planar. Here the "jumps" must be evaluated between appropriately defined upstream and downstream regions (Schwartz, 1998). Lack of clarity about how to designate the upstream and downstream regions appropriately in the vicinity of real bow shock measurements, along with doubt and concern about the possible consequences of inappropriate designations, provided the chief motivation for our statistical study, described later in this work. There we comment in detail on strategies for defining the upstream and downstream regions in observational data, where the subsequent analysis was a modified form of RH analysis.

In practical terms, RH analysis is a little more cumbersome to implement than MVA, which mostly boils down to a few matrix operations. Assuming that the upstream and downstream regions have already been sensibly chosen for a tolerably docile shock, one must next calculate several vector component averages in those regions using some assumed normal vector, which may or may not be anywhere near the real one. Understandably, this has led to a variety of ingenious strategies over the years for zeroing in on the normal as quickly as possible and with the least waste of computational resources (Viñas & Scudder, 1986). Fortunately, the necessary calculations no longer impose so onerous a computational burden, and it is not so unreasonable simply to try a

few hundred possible normal vectors within some angular search area and pick the one that yields the best adherence to the shock conservation relations.

Like MVA, RH analysis is performed on data from a single spacecraft, where the most critical measurements to obtain are the magnetic field vector and the velocity vector of either ions or electrons. (In solar wind contexts, for instance, ion moments are harder to measure with accuracy and electrons may be preferred.) Electric field measurements may or may not be of sufficient quality for the analysis; if not, one may attempt to employ the cross-product $\boldsymbol{v} \times \boldsymbol{B}$ instead. For instance, we preferred to try $\boldsymbol{v} \times \boldsymbol{B}$ in our statistical study but ultimately chose to leave this contribution out entirely, as it yielded very ambiguous "variance maps", explained below.

In order to exploit the strategy of comparing conservation from many possible normal vectors, we can examine "variance maps", which indicate the change between upstream and downstream averages, of any combination of (normalized) contributions from the normal magnetic field, normal momentum flux, and transverse electric field. Such maps are formed as contour or color plots against the (angular) coordinates of the corresponding normal vector. Correctly identifying the normal then becomes a problem of finding the minimum variance on the map, with the caveat that multiple minima may be occur and may be difficult to differentiate.

For all its complexities, one of the benefits to using RH analysis to identify the shock normal is that the shock velocity is obtained as a by-product of the analysis.

3.1.3 Bow shock models

A helpful reality check when studying spacecraft observations of the bow shock, especially if the mission only involves one spacecraft, is comparison with a model bow shock normal. In our analysis, we were fortunate enough to have recourse to 4-spacecraft data; thus, timing analysis (to be discussed shortly) was available to us in our case studies, and RH analysis sufficed for our needs in the statistical study. At no time were we dependent upon a model for the shock normal. The model was thus more a matter of curiosity, an interesting reference point for comparison with normals obtained by other means.

The critical steps in identifying the shock normal from a bow shock model are set forth in detail in Schwartz (1998), along with the most commonly used models. Bow shock models do not differ radically in their basic considerations or geometry; rather, differences are due to the quantity of data available, how observed bow shock crossings were grouped (or not), whether any distinctions were made based on Mach numbers or IMF orientations, etc. (Compare Farris et al. (1991), Peredo et al. (1995), and Slavin & Holzer (1981), for instance.) The shape of the bow shock is generally considered to be a conic section, with individual models differing in the fine-tuning of the shape. These models are necessarily of limited spatial extent, since the bow shock eventually gives way to the magnetotail rather than tying off neatly as an ellipse or carrying on indefinitely as a tidy hyperboloid (Schwartz, 1998). We opted to employ the model of Slavin & Holzer (1981), so any specific remarks from our process will relate to the implementation of this particular model.

Since the solar wind travels radially outward at hundreds of km/s, while the earth shoulders along its orbital path at about 30km/s, the bow shock's ellipsoidal dayside shape is tilted, its major axis slightly offset from the radial direction by some aberration angle α (Schwartz, 1998). One can take a typical value of this angle, which is about 4°, or if velocity measurements are available one can calculate the angle as observed during a specific event of interest (Slavin & Holzer, 1981).

Similarly, the solar wind will alter the size and scale of the bow shock boundary by compressing it more or less aggressively as the solar wind pressure varies. One way to approach

this is to scale the bow shock model by comparing the measured solar wind pressure to some reference pressure, but this remains a rather uncertain means of addressing the problem. A more reliable strategy, and one that we were able to take advantage of, is to rescale the aberrated bow shock such that its boundary includes an observed crossing point (Schwartz, 1998). For our analyses, an iterative code was used to identify a scaling coefficient that placed the bow shock boundary within $10^{-4}R_E$ of an observed crossing point.

Once the aberration and scaling are determined, all that remains is to compute the normal vector to the model bow shock at the observed shock crossing location. The gradient of the shock's two-dimensional surface must be returned to the original coordinate system by reversing the aberration (Schwartz, 1998). Requiring the normal vector to have unit length provides another constraint, and it is conventional to select the direction such that the normal vector points towards the upstream region, in this case the oncoming solar wind.

As with MVA, a disadvantage of resorting to bow shock models for the shock normal is that the shock speed must be obtained by other means. However, if as in our case it is used more as a sanity check or point of comparison for other calculations, it certainly has some value.

3.1.4 Timing analysis

Timing analysis is a method that relies upon the availability of data from four spacecraft flying in a controlled formation (Schwartz, 1998). We will briefly outline the general process and then mention some conditions that must be met in order to obtain unambiguous results.

The moment of the shock crossing is first identified in timeseries data from each spacecraft; often the magnetic field magnitude, or a single vector component, is used as the basis for this comparison. The spacecraft position or separation vectors at this time must be known. Then both the normal vector and the shock speed can be found simultaneously by solving the system of equations:

$$\begin{pmatrix} \boldsymbol{r}_{12} \\ \boldsymbol{r}_{13} \\ \boldsymbol{r}_{14} \end{pmatrix} \cdot \frac{1}{v_{sh}} \begin{pmatrix} n_x \\ n_y \\ n_z \end{pmatrix} = \begin{pmatrix} t_{12} \\ t_{13} \\ t_{14} \end{pmatrix}$$

Where subscripts 12, 13, 14 indicate separations in space $\boldsymbol{r}$ or time t between spacecraft 1 and 2, 1 and 3, or 1 and 4, respectively. The shock velocity v_{sh} is the velocity of the shock along the direction of the normal $\boldsymbol{n}$ (Schwartz, 198). While this method is generally considered more reliable than any of the single-spacecraft methods discussed previously, there are a few possible pitfalls that may prevent its application.

First, it must be possible to find a uniquely identifiable feature in the timeseries magnetic field profiles from all four spacecraft. Spatial variations on the scale of the spacecraft separation distances, or temporal variations on the scale of the timing separations, may prevent this.

If fluctuations obscure the magnetic field profiles, making it hard to decisively identify the ramp, for instance, it may be possible instead to model the magnetic field as a hyperbolic tangent. Then a threshold value of the magnetic field may be chosen, somewhere between the upstream and downstream equilibrium values, and the time when each modeled profile attains the threshold value then gives the matching time. The caveat here is that not all profiles lend themselves willingly or gracefully to approximation by a hyperbolic tangent.

One of the key design features of the Magnetospheric Multiscale (MMS) mission, which provided the data for the analyses we will describe later, is that the separation distances between the four spacecraft may be as small as a few tens of kilometers, allowing investigations into

electron-scale microphysics. This boon to reconnection studies can be a stumbling block in timing analysis: smaller separation distances lead to smaller "separation times." If a shock is particularly fast-moving, the necessity of dividing by the separation times can come dangerously close to division by zero, increasing the uncertainty of the result or, worse, making it impossible to exploit timing analysis at all.

The considerations above mean that successful execution of timing analysis requires a fair amount of human supervision. Unlike the previous methods of determining the shock normal, all of which we deployed in an automated manner in our statistical study, timing analysis does not lend itself with good grace to automation. This limits the range of its possible applications. For small studies and case studies, where detailed attention to the processing of each individual shock is feasible, it is a desirable method for obtaining both the shock normal and the shock speed.

3.2 Shock-oriented coordinates

Spacecraft observations of near-Earth shocks will generally be given in some Earth-centric coordinate system such as Geocentric Solar Ecliptic (GSE) or Geocentric Solar Magnetic (GSM). For convenience, it is advisable to rotate the shock observations into a coordinate system defined by the shock geometry. Thereafter it is simple to transform the data into some suitable shock-rest frame such as NIF or HTF. Naturally, the shock normal forms the most interesting axis, and if it has been obtained via MVA, then a complete set of orthogonal basis vectors has already been secured.

In situations where MVA was not performed, or where it returned unreliable results, an intuitive option for defining the second basis vector involves the magnetic field magnitude. In the plane perpendicular to the shock normal (this plane should ideally represent the shock surface itself), the projection of the average upstream magnetic field vector can provide a useful basis vector, similar to what would have been provided as the maximum variance direction had MVA been viable. Taking the third vector as the right-handed completion of the triad, we often called these basis vectors an "MVA coordinate system" for lack of a more concise name, even though MVA had nothing to do with the process.

Once rotation into this shock-oriented coordinate system has been accomplished, the next typical step is transformation into an appropriate shock rest frame.

3.3 Implementing shock rest frames in space observations

In the matter of rendering measured data into a useful shock frame, there are two main aspects to consider. One is the basic velocity transformation itself, and the other is the choice of reference frame.

Let us assume for a moment that we have already determined the appropriate transformation velocity $\boldsymbol{v}_T$ for our desired reference frame. Note that near-Earth space plasma shocks are unlikely to be relativistic: the terrestrial bow shock is typically observed to have speeds in the tens of km/s (Burgess & Scholer, 2015). Even CMEs rarely travel faster than 2000 km/s (Kallenrode, 2004). The non-relativistic transformation of the measured velocity $\boldsymbol{v}$, magnetic field $\boldsymbol{B}$, and electric field $\boldsymbol{E}$ goes as

$$\boldsymbol{v}' = \boldsymbol{v} - \boldsymbol{v}_T$$

$$\boldsymbol{B}' = \boldsymbol{B}$$
$$\boldsymbol{E}' = \boldsymbol{E} + \boldsymbol{v}_T \times \boldsymbol{B}$$

In the above equations, the prime superscript designates vectors in the new shock rest frame.

The most bare-bones or minimalist way to access a shock rest frame would be simply to set the shock-normal component of the transformation velocity to equal the shock speed, allowing the other components to be zero. This transformation is not typically used, however. Instead, more meaningful choices are the Normal Incidence Frame (NIF) and de Hoffmann – Teller Frame (HTF), both described previously in Chapter 1.

The shock-tangential components of the NIF transformation velocity are simpler to determine than those corresponding to HTF. To shift into NIF, it is necessary to find the average upstream velocity components: these then give the remaining components of the transformation velocity, so that after the transformation the upstream ion flow is directed straight into the shock front, parallel to the normal. Choosing the appropriate upstream region may be the more challenging part of this procedure.

Alternatively, the goal of transformation into HTF is to eliminate any motional electric field by forcing the upstream ion flow to be parallel to the magnetic field. There are a couple ways to approach this task. One might be tempted to take a rather brutal or bloodthirsty approach to the problem by comparing the average upstream velocity and magnetic field vectors, but a more successful and nuanced result may be obtained by resorting to matrices and treating it as an optimization problem. (See Khrabrov & Sonnerup (1998).)

From that perspective, the task is to minimize the motional electric field accumulated within the designated upstream time range. Khrabrov & Sonnerup (1998) provide equations that can determine the transformation velocity to HTF from any arbitrary reference frame or coordinate system: although their algorithm can be applied after the data have been rotated into a shock-oriented coordinate system, starting from shock-oriented coordinates is by no means required. In their algorithm, they minimize the average of the squared electric field magnitude over a set of M data points. (In our case, these were in the upstream region.) This average can be expressed as

$$\langle |\boldsymbol{E}|^2 \rangle = \frac{1}{M} \sum_{m=1}^{M} \left[\left| \left(\boldsymbol{v}^{(m)} - \boldsymbol{v}_T \right) \times \boldsymbol{B}^{(m)} \right|^2 \right]$$

where the transformation velocity $\boldsymbol{v}_T$ remains to be determined in the process of minimization. The superscript (m) identifies data corresponding to the time stamp having index m. Solving for $\boldsymbol{v}_T$ requires taking the velocity gradient of the above and setting it to zero (Khrabrov & Sonnerup, 1998). We begin by defining for each time stamp a 3×3 matrix $\boldsymbol{K}^{(m)}$ with elements

$$\boldsymbol{K}_{\mu\nu}^{(m)} = \left| \boldsymbol{B}^{(m)} \right|^2 \left[\delta_{\mu\nu} - \frac{B_\mu^{(m)} B_\nu^{(m)}}{|\boldsymbol{B}^{(m)}|^2} \right]$$

along with an average matrix $\boldsymbol{K}_0$ for the entire set M

$$\boldsymbol{K}_0 \equiv \langle \boldsymbol{K}^{(m)} \rangle = \frac{1}{M} \sum_{m=1}^{M} \left[K_{\mu\nu}^{(m)} \right]$$

Then the solution $\boldsymbol{v}_T$ can be written

$$\boldsymbol{K}_0 \boldsymbol{v}_T = \langle \boldsymbol{K}^{(m)} \boldsymbol{v}^{(m)} \rangle = \frac{1}{M} \sum_{m=1}^{M} \left[\boldsymbol{K}^{(m)} \boldsymbol{v}^{(m)} \right]$$

which leads to

$$\boldsymbol{v}_T = \boldsymbol{K}_0^{-1} \frac{1}{M} \sum_{m=1}^{M} \left[\boldsymbol{K}^{(m)} \boldsymbol{v}^{(m)} \right]$$

as long as $\boldsymbol{K}_0^{-1}$ does not lead to division by zero (Khrabrov & Sonnerup, 1998). Of course, as was already discussed, transformation to the HTF may not be possible at all, if the inflow speed and shock angle are too great.

3.4 Separating distinct populations in ion distribution data

In handling the ion distributions and moments, there are two techniques we employed that merit focused discussion. These were somewhat particular to the MMS mission because of the high spatial and temporal resolution of data from the electrostatic analyzers of the Fast Plasma Investigation (FPI) instrument (Pollock et al., 2016), which is described in Chapter 4. They consisted of first identifying distinct populations in the upstream ion distributions and then recalculating moments for each population separately.

Separation of the ion populations required examination of the so-called "skymaps", a data product in which the phase space density (PSD) is provided in a timeseries of multi-dimensional arrays, each time stamp including the data for 32 energy bins in 32 azimuthal and 16 polar angle bins. The angular coordinate system is defined in a despun coordinate system centered on the spacecraft body (Pollock et al., 2016). In such a despun coordinate system, the incoming solar wind is a stable and predictable presence within a reliable group of angular bins. It is therefore possible to isolate the angular bins corresponding to the solar wind ions from the rest of the ion distribution, taking any significant population outside the solar wind's angular range to correspond to ions reflected from the shock front.

These populations can be tracked separately, in addition to the total population, through the upstream region until the arrival of the shock ramp. What this subsequently enables is the calculation of moments (density, velocity, etc.) not merely for the solar wind ions and the reflected ions, but even for subsets in energy within these populations. In practice, we were most interested in energy subsets for the reflected populations, in order to estimate the density of reflected ions in higher energy ranges compared to the total ion density.

3.5 Electric field measurements in space plasma

In discussing the measurement of electric fields in space plasma, we focus our attention particularly on the double-probe technique, the dominant method employed on spacecraft. After test flights on sounding rockets, double-probe instruments were successfully deployed on the S3-3 and ISEE satellite missions, with S3-3 making the first low-frequency electric field measurements in 1976 (Mozer et al., 1977, 1978; Mozer & Bruston, 1967). Probes are suspended in the plasma at a significant distance from the spacecraft and arranged so that pairs of probes extend in opposite directions. Each pair of probes should be collinear with each other and the spacecraft. The basic measurement here is the potential difference between a single probe and the spacecraft; subtracting the singled-ended measurement of one probe from that of its counterpart then eliminates the spacecraft potential, leaving the potential difference between the probe pairs (Laakso et al., 1995; Mozer, 2016). We will return to this idea shortly, when we discuss calibration

of electric field data. Our overriding interest throughout this section will be DC electric field measurements.

The manner whereby surfaces such as the probes and spacecraft attain an electrostatic potential is important to describe. Charged particles flow to the spacecraft continually from many possible origins: ambient plasma ions and electrons, photoelectrons engendered by sunlight striking spacecraft or instrument surfaces and booms, secondary electrons, and (if applicable) a bias current (Fahleson, 1967; Lai, 2011; Mozer, 2016; Whipple, 1981).

The bias current is fed to the probe by electronics on the spacecraft in order to limit the probe voltage to an optimal range for registering the measurements. In order to explain why and how this works, we refer to Figure 3.1, which shows a so-called "I-V curve" (Chen, 1965; Laakso et al., 1995; Mozer, 2016).

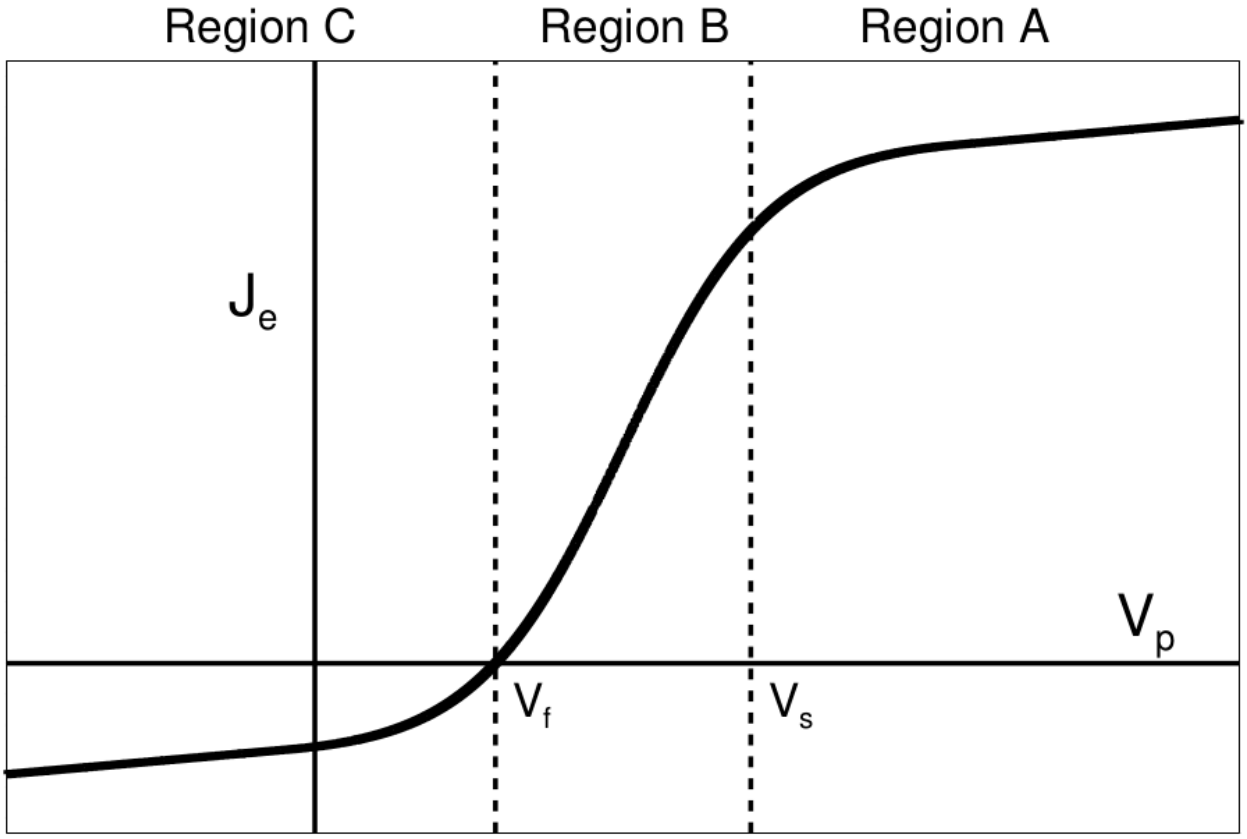

Figure 3.1. Characteristic I-V curve of a Langmuir probe immersed in a plasma. The horizontal axis is probe voltage, and the vertical axis is electron current. Region A consists of probe voltages exceeding the space potential V_s. Region C includes all probe voltages below the floating potential V_f. In between these extremes is Region B, the ideal measurement range. Adapted from Chen (1965).

In Figure 3.1, the horizontal axis represents the voltage V_p of an electric field probe immersed in a plasma, while the vertical axis shows electron current J_e. The voltage V_p is understood to be with respect to some arbitrary reference point, meaning the entire curve may shift right or left depending what reference point is chosen. The plasma is assumed to be quasi-neutral,

with equal temperatures for ions and electrons. Note the points on the curve corresponding to the values V_s and V_f. These separate the I-V curve into three distinct regimes A-C, presently to be described.

Point V_s (the "space potential") represents the potential of the surrounding plasma (Chen, 1965). This may seem like a good place for the probe potential to reside, but let's not be too hasty. Suppose the probe does have potential V_s – what then? It offers no strong attraction or repulsion to the charged particles in the surrounding plasma, and any electrons or ions that strike the probe do so merely in the course of their thermal meanderings. In a single-temperature plasma, electron thermal speeds far exceed those of the ions, so that the current to the probe is dominated by electrons (Chen, 1965).

Next we consider Region A, corresponding to probe potentials that are more positive compared to V_s. Under these circumstances, charged particles are now electrically aware of the probe's presence: ions are repelled, further reducing their current contribution, while electrons are attracted. This causes a separation of charges just above the probe surface, with electrons clustering closest to the probe and thereby forming a negatively-charged sheath. In spite of the probe's electron-attracting potential, the crowd of electrons in the sheath effectively cancels the probe potential at long distances, preventing the uncontrolled stampede of electrons to the probe that one might naïvely expect to see. Instead, within region A, the electron current is said to be saturated (Chen, 1965).

Region B (the "transition region"), where the probe potential is modestly negative compared to the plasma potential V_s, sees the ions being slightly attracted to the probe, while electrons are slightly repelled (Chen, 1965). Both species are still able to reach the probe and contribute to the current because the electrons' thermal speed is high enough to overcome the slight electrostatic repulsion. Point V_f (the "floating potential"), where all currents are balanced, marks the boundary between the Region C and the transitional Region B (Chen, 1965).

Beyond V_f, in Region C, we find the ions' analog of the electron saturation in Region A. At these very low potentials, the electrons' high thermal speeds are insufficient to overcome the probe's negative potential, and electrons are wholly driven away. Instead, ions gather around the probe surface, and the probe potential is all but nullified outside the ion sheath (Chen, 1965).

In the above discussion, we have assumed equal temperatures for ions and electrons, which is not a realistic scenario in most space environments. Additionally, our discussion of the particle motion has neglected any influence of magnetic fields. However, this theory is necessary for understanding, among other things, the role of the bias current applied to the probe: its role is to force the probe's equilibrium voltage to reside within the transition region (Chen, 1965).

Determining the optimal bias current must be done in flight repeatedly throughout the mission in order to adapt to the unique plasma conditions encountered over time in different regions of the magnetosphere and heliosphere. Prior to launch, however, high-quality electric field measurements can be promoted by striving to make pairs of probes, along with their associated electronics or exposed parts, as nearly identical as possible (Mozer, 2016). This is because the primary measurement along any electric field component is the potential difference between opposite pairs of probes. Ideally, if the spacecraft and a pair of probes 1 and 2 are at potentials V_{sc}, V_1, and V_2 with respect to the unknown local plasma potential, then the single-ended potential measurements from probes 1 and 2 are $V_1^{meas} = V_1 - V_{sc}$ and $V_2^{meas} = V_2 - V_{sc}$, respectively. Subtraction yields the potential difference between probes 1 and 2 (Mozer, 2016):

$$V_{12} = V_1^{meas} - V_2^{meas} = (V_1 - V_{sc}) - (V_2 - V_{sc}) = V_1 - V_2$$

There's a catch here. We have swept two unsavory possibilities beneath the rug:

1) What if the reference potential at V_{sc}, V_1, and/or V_2 is not the same? In other words, we have neglected spatial variations on scales comparable to or smaller than the probe separation distance (Laakso et al., 1995).

2) What if individual quirks in either probe result in enhancements or variations in emission of photo- or secondary electrons? Then the current balance equation for the affected probe will be skewed, bringing it to a different equilibrium potential with respect to the plasma and thereby causing a spurious contribution to the single-ended potential measurement. Any noisy behavior that affects only one probe and not the other will not be subtracted away when calculating V_{12}. This is the motivation for manufacturing identical probes that will respond in a uniform manner to stimuli in the plasma environment or to illumination (Mozer, 2016).

Before accessing and analyzing electric field data, there are some important questions to consider first.

1) What is the frequency range of interest? Obtaining and calibrating the DC electric field data is far more difficult that processing higher-frequency data, and thus there will be more stringent limitations in event selection. In the case of a spinning spacecraft, for instance, it will often be hard to justify the use of axial component data for DC electric field analysis (Mozer, 2016).

2) How is the magnetic field oriented with respect to the spacecraft? If the axial measurement is inadequate, one may have to choose between ignoring the third component altogether or estimating it by exploiting the MHD assumption that $\boldsymbol{E} \cdot \boldsymbol{B} = 0$. Other estimation schemes may be tailored to specific situations, such as that employed by Dimmock et al. in a study of shocks (Dimmock et al., 2011).

If one opts to avoid using the axial component, the magnetic field needs to be either mostly axial or mostly in the spin plane. In the former case, the spin plane measurements can then be understood to represent the two perpendicular components of the electric field. In the latter case, the spin plane data will provide one perpendicular component and the parallel component.

If one has set one's heart on analyzing three components using the assumption $\boldsymbol{E} \cdot \boldsymbol{B} = 0$, the third component E_z^{est} is estimated by solving

$$E_z^{est} = \frac{\left(E_x B_x + E_y B_y\right)}{B_z}$$

where E_x (B_x) and E_y (B_y) are the spin-plane components of the electric (magnetic) field, and B_z is the axial component of the magnetic field. Then the predominant direction of the magnetic field is particularly important in determining whether the estimated component E_z^{est} is reasonable. If the axial component of the magnetic field is very small, the axial electric field component E_z^{est} may blow up unrealistically.

Part of this decision-making process, as well as the business of event selection, hinges critically on a visual assessment of the data quality. There are several common misfortunes that can befall the probes in space, potentially spoiling the measurements, and it may not be possible to mitigate their damaging effects on the data by means of post-processing. Among typical problems that occur are biasing issues (e.g. when magnetospheric missions stumble unexpectedly into the solar wind) and asymmetries due to passage of a probe through the shadow or plasma wake of the spacecraft. As previously mentioned, asymmetry in the probes or their environmental conditions can give rise to false voltage signals (Mozer, 2016).

We can take advantage of the intrinsic geometry when assessing spin-plane measurements. Single-ended measurements from an opposing pair of probes can be compared: ideally, the signals should be approximately sinusoidal in time, with nearly identical amplitudes that are anti-correlated. The period of the sinusoidal variation is expected to be the spacecraft spin period. We can then compare voltage differences V_{12} and V_{34} from the spin-plane pairs: these also should be sinusoidal on the spin period and of comparable amplitudes. Additionally, since each pair lags behind the other by a quarter revolution, the two signals should be 90° out of phase.

As yet we have said nothing about the relative value of these potential signals, only specifying that they should be similar in size. This is because determining DC offsets of electric field data is a significant calibration ask, and one which is particularly difficult for the axial component – sometimes even prohibitively so. Ideally, one has access to magnetic field data and particle moments so that one can compare the measured electric field signals to $\boldsymbol{v} \times \boldsymbol{B}$, the cross-product of the velocity and the magnetic field. These may differ somewhat on fast timescales, but the general expectation is that, so long as the spacecraft is in a plasma environment where MHD can reasonably hold sway, the overall features of $\boldsymbol{E}$ and $\boldsymbol{v} \times \boldsymbol{B}$ should coincide.

We mentioned previously that inappropriate biasing can cause problems in the electric field measurement, especially if the spacecraft is outside of its intended environment or if local plasma conditions shift for the worse. Bias sweeps are repeated regularly throughout the mission (e.g. once per orbit) in an effort to adapt continually to local changes (Mozer, 2016). In the course of such a sweep, the full range of values for the bias current and the guard voltages (for more about guard voltages, see Chapter 4, section 4.4) are cycled through in all possible combinations to determine where the observed electric field signal settles into some small, sensitively fluctuating value, rather than ricocheting back and forth between extreme values that indicate saturation (Mozer, 2016). If the sweep is always performed in the magnetosphere, for instance, it is likely that the bias and guard settings will prove unfavorable should the spacecraft pass into the solar wind, where prevailing plasma conditions are markedly different.

These are only some of the most salient aspects of electric field measurement and calibration that affected our own work. There are many other pitfalls, tricks, and details, some of which are described in Mozer (2016).

Chapter 4
Magnetospheric Multiscale (MMS) Mission and Data Products

The Magnetospheric Multiscale (MMS) mission is primarily motivated by a drive to better understand magnetic reconnection. Specifically, it is designed to probe magnetic reconnection at the dayside interaction between the solar wind and the magnetosphere and on the nightside near the plasma sheet in the near magnetotail (Burch et al., 2016; Fuselier et al., 2016). Outstanding unresolved questions in reconnection science at the time when MMS was being developed required a detailed picture of electron dynamics. In particular, it was highly desirable to make multipoint measurements at exceptionally high sampling rates while the spacecraft were separated by distances on the order of the local electron inertial length. The reason for this was because the electron diffusion region, where electron kinetic effects such as strong currents may drive energy dissipation and magnetic field topology changes, should have a thickness similar to the electron inertial length (Burch et al., 2016).

The primary mission of MMS was conducted in a series of phases or stages, each concentrated upon gleaning the greatest possible science return from a given area of each orbit (the science Region of Interest or ROI) (Fuselier et al., 2016). The first phases were optimized for measurements in the dayside reconnection region; during the first several days of each phase, spacecraft separations (or, equivalently, the size of the tetrahedral constellation) are systematically varied through values near the local electron inertial length in order to identify the ideal separation. The spacecraft are then flown at that separation for the rest of the phase, typically lasting a few months (Fuselier et al., 2016).

During the first phases of the MMS mission, designed such that the orbital apogee had a strong chance of coinciding with the dayside reconnection region, the spacecraft rarely passed through the bow shock into the solar wind. Not until later phases, when the apogee was gradually increased in order to access the more remote nightside reconnection region in the magnetotail, did MMS make regular passes through the terrestrial bow shock (Fuselier et al., 2016). Even then, restrictions on data transmission mean that burst mode data is not available for all such crossings.

Since the increase of apogee, and thanks to the precession of the orbit, the MMS constellation has regular periods when the orbital apogee is generally in the solar wind. Over a few months, it slides from the duskside of the bow shock (generally associated with quasi-perpendicular shocks) to the dawnside (where quasi-parallel shocks and the foreshock are typical) (Fuselier et al., 2016). Sampling a wide range of parameters characteristic to different regions of the bow shock, MMS is thus a valuable mission for studying not just reconnection but also collisionless shocks. The presence of four identical spacecraft and the high sampling rates suit MMS data exceptionally well for studies of shock microphysics in addition to macrophysics.

For our purposes, a subset of the available instruments were of greatest value: magnetic field measurements from the Fluxgate Magnetometer (FGM), ion and electron distributions and moments from the Fast Particle Investigation (FPI), and electric field measurements from the Spin-Plane Double Probe (SDP). Our work with electric fields was in the low-frequency (DC) regime, which is more challenging for the Axial Double Probe (ADP), designed to complete the measurements from SDP. We will describe ADP even though we were unable to take advantage of its data. Similarly, the ion data from FPI was generally sufficient for our purposes, and only in one instance did we refer to the Hot Plasma Composition Analyzer (HPCA).

4.1 FGM

The MMS FGM is part of the FIELDS suite of instruments, the purpose of which is to provide self-consistent, mutually-calibrated magnetic and electric field measurements (Russell et al., 2016; Torbert et al., 2016). The FIELDS suite incorporates not only FGM, SDP, and ADP, but also the Search-Coil Magnetometer (SCM), which provides magnetic field data in a higher-frequency regime, and the Electron Drift Instrument (EDI), which shoots beams of electrons, curving in the local magnetic field and returning to detectors on the spacecraft, to provide an additional estimate of the fields. The data from all constituent FIELDS instruments are used for intercalibration among the instruments (Torbert et al., 2016).

The FGM itself actually consists of two separate units: the Analog and Digital Fluxgates (AFG and DFG, respectively). Each spacecraft is equipped with two identical fluxgate sensor units, mounted at the end of 5m booms in the spin plane, on opposite sides of the spacecraft (Russell et al., 2016). Although the sensors are the same, the reading and processing electronics for the AFG and DFG are completely distinct and independent from each other. This is to ensure that a fault in one of the units cannot disable the other. Magnetic field vector measurements are considered critical for the successful fulfilment of the MMS mission's science goals, and thus extra precautions were taken to protect the measurement from errors (Russell et al., 2016).

As long as both the AFG and DFG are functioning, they can also serve as a useful check against each other. The AFG electronics are based on designs that have been flown successfully on many prior missions, while the DFG is newly designed for MMS and relies upon an ASIC (Russell et al., 2016). The FGM data is useful primarily for lower-frequencies, from DC to a maximum near the nominal Nyquist frequency of 64Hz (Russell et al., 2016).

4.2 SCM

Since we did not make significant use of the SCM data in our studies, we will be brief here. It is not strictly true to say that the SCM is a passive device, whereas the FGM is an active device. The SCM does include additional feedback windings on each axis, the purpose of which is to counteract some of the natural resonance effects of the inductor (Le Contel et al., 2016).

The main anticipated value of the SCM data, which covers a frequency range of 1Hz to 6kHz, is that it will enable detailed study of fluctuations and waves in the vicinity of reconnection. Therefore it is necessary to maintain a high sampling frequency at all times. Unlike the FGM, which consists of a doppelgänger pair of sensors with one analog and one digital set of processing electronics, there is only one SCM per spacecraft, mounted partway along the same boom as the AFG (Le Contel et al., 2016).

4.3 FPI

Rapid accumulation of *in situ* particle distributions presents a singular challenge on any space mission, with the challenge growing more acute in more tenuous plasmas. Top-hat electrostatic analyzers, or ESAs, have been a popular choice for particle measurements on many

previous missions (e.g. FAST, THEMIS), enabling measurements in many angles and energies. These were first flown on sounding rockets in 1982 before being implemented on the Giotto and AMPTE space missions (Carlson et al., 1982). The catch is that, in order to obtain a full 3D distribution (4pi sr solid angle), the spinning spacecraft must complete a full rotation. Thus, the sampling period of the particle distributions is tied to the spacecraft spin period. In the case of MMS, that would be over 4s, much too slow to be of use in the quest to understand magnetic reconnection (Pollock et al., 2016).

Indeed, the mission requirements for particle distributions stipulated that electron (ion) data should be sampled every 30 (150) ms. This unusual difficulty was addressed by equipping each spacecraft with multiple ESAs, eight for electrons and eight for ions (Pollock et al., 2016). (Other missions, too, have bypassed the limitation of one distribution per spin period; examples include FAST, Polar, and Juno (Pollock et al., 2016).)

Top-hat electrostatic analyzers are comprised of a pair of concentric, approximately hemispherical shells. Particles entering through an aperture at the crown of the outer shell are deflected by a potential difference between the shells. This potential difference is adjustable and is used to limit particles measured to some specific energy range at any given time: excessively (insufficiently) energetic particles will deflect too little (too much), strike the outer (inner) shell, and be lost (Pollock et al., 2016).

The initial trajectory of a particle in the desired energy range will lead it to strike one anode in a circular ring of multichannel plate (MCP) detectors, thereby indicating its trajectory to belong to a specific angular bin from the available annulus. The other angle necessary to describe its motion is determined from the spin phase of the spacecraft (Pollock et al., 2016).

In the specific case of MMS, the eight detectors for a given species (electrons or ions) are arranged in pairs in the spacecraft spin plane, with each pair placed along the outermost edge of the spacecraft body. The detectors are positioned such that the annulus of MCP anodes is vertical, i.e. the plane of the annulus is perpendicular to the spin plane. Only half the annulus, corresponding to 180 degrees in polar angle, is used in this configuration (Pollock et al., 2016).

Each pair of detectors is mounted such that their apertures are directed 45 degrees away from each other in the spin (azimuthal) plane. Additional electronics outside the aperture set the deflection of particles approaching the aperture. Thus, each detector can be stepped through four different ranges of incoming azimuthal angle bins, spanning a total of 22.5 degrees per device (Pollock et al., 2016).

The rate at which azimuthal deflection and energy bin changes for each detector can be accomplished determines the sampling rate for the electron and ion distributions. Between the ROI and the perilous radiation belts, FPI operates in Slow Survey mode. Here, three spin periods of 4.5s are required to accumulate a full, 3D distribution for each particle species. In order to share the wear-and-tear equally, the detector responsible for the Slow Survey measurements is changed every orbit (Pollock et al., 2016).

Within the ROI, the instrument operates at full capacity but produces two types of data product resolutions: Fast Survey and Burst. Burst-rate data represent the highest-speed operation of the instrument and are saved during the entire ROI transit. All Fast Survey data are transmitted to the ground, but there is sufficient telemetry bandwidth to downlink only a small percentage of Burst data. Fast Survey data does not imply any difference in the operation of the instrument compared to Burst data. Instead, the Burst distributions are averaged down to a sampling rate of one per spin period in order to create Fast Survey distributions (Pollock et al., 2016).

4.4 ADP/SDP

Both the ADP and SDP rely on the double probe technique described in the previous chapter. SDP includes two pairs of probes in the spacecraft spin plane, while ADP consists of one pair of probes along the spin axis. The probe pairs are arranged to form three orthogonal components in order that their combined data yield 3D electric field measurements from DC to 100kHz (Ergun et al., 2016; Lindqvist et al., 2016). Another common element of SDP and ADP is their range of sampling rates: time series measurements are taken at 8 s^{-1} and 32 s^{-1} in Slow and Fast Survey modes, respectively. Burst data may be stored at 1024 s^{-1}, 8192 s^{-1}, or 65536 s^{-1} (Ergun et al., 2016; Lindqvist et al., 2016).

Otherwise, the actual construction of ADP and SDP differ significantly. Maintaining the probes far away is of key importance to minimize the impact of spacecraft-related currents on the probes and to avoid the influence of the spacecraft potential. In the spin plane, the centrifugal effect is exploited so that probes may be tethered to the spacecraft merely by lightweight wire booms that also house the signal cables. The four SDP probes are attached to the spacecraft at the end of 57m booms, giving a probe-to-probe separation of 120m. The preamplifiers are located 2m inward of each probe, with the rest of the processing electronics housed on the spacecraft itself (Lindqvist et al., 2016).

For the ADP, centrifugal effects are the enemy, and the farther out the probe extends, the greater are the engineering challenges in keeping it stably in position. Furthermore, it is important for the moment of inertia around the spin axis to be unquestionably dominant, a relationship that is increasingly jeopardized as the axial electric field booms are increased in length (Ergun et al., 2016). The axial booms on MMS are ambitiously long, with a combined length of nearly 30m, exceeding all previous attempts at spacecraft measurements of the electric field along the axial component. The booms themselves must be more sturdily constructed than the spin plane booms; instead of simple cables, the axial booms consist of a helical structure of many interlacing parts that can be coiled for storage during launch. The booms are topped by a stiff rod that carries both the preamplifier and an antenna to collect the electric field signals (Ergun et al., 2016).

Bias currents can be applied to the probes for both SDP and ADP. In addition, surfaces near the probes can be maintained at "guard voltages" intended to discourage photoelectrons from the spacecraft or the booms impinging on the probes (Ergun et al., 2016; Lindqvist et al., 2016). In the case of SDP, the sides of the preamplifier nearer to and farther from the probe can be set to different voltages (Lindqvist et al., 2016). A guard voltage for the ADP can be set for the preamplifier and lower parts of the rod (the "receiving element") down to the end of the boom (Ergun et al., 2016). The boom itself is crowned by a plate, the surface of which is kept in shadow by a ring encircling the plate; the underside and top side of this plate can likewise be maintained at separate "inner guard" and "outer guard" voltages (Ergun et al., 2016).

Part III

New Findings and Statistics

Chapter 5
Cross-Shock Electric Potential: Theory, Direct Estimation from MMS Measurements, and Validation

This chapter lays out the analysis of our first shock paper (Hanson et al., 2019), published in *Geophysical Research Letters*. In this study, we focused on two specific shock observations in the MMS data and estimated the electrostatic potential across the ramp.

5.1 Scientific background

The electric cross-shock potential is an important element of shock structure, influencing energy redistribution at the shock front (Zank et al., 1996). The potential difference, its distribution across the shock, and the scale of its variation are of primary importance for understanding physical processes in shocks. Goodrich & Scudder (1984) were the first to point out the dependence of potential field on the reference frame and to highlight the role of the potential in the formation of flat-top and beam-like characteristics of the electron distribution.

Collisionless shocks have been studied for over 60 years, and many satellites have collected *in situ* measurements of interplanetary (IP) shocks and Earth's bow shock (e.g. ISEE (Sckopke et al., 1983), Cluster and THEMIS (Hobara et al., 2010), Polar (Hull et al., 2006), Wind (Wilson et al., 2012)). Significant progress has been made in understanding the mechanisms of energy transformation from the directed ion flow to the thermal and suprathermal populations; see reviews (Bale et al., 2005; Krasnoselskikh et al., 2013) and references therein. The structure of the magnetic field shock front; evolution of ion and electron distribution functions; and characteristics of waves upstream, inside, and downstream of the shock have been reported in numerous publications (Krasnoselskikh et al., 2013). However, there are only a few publications devoted to measurements of electric field and electrostatic potential across the shock (Bale et al., 2008; Bale & Mozer, 2007; M. Balikhin et al., 2005; M. A. Balikhin et al., 2002; Dimmock et al., 2011, 2012; Formisano, 1982; Heppner et al., 1978; Hobara et al., 2010; Scudder, Mangeney, Lacombe, Harvey, & Aggson, 1986; Scudder, Mangeney, Lacombe, Harvey, Aggson, et al., 1986; Scudder, Mangeney, Lacombe, Harvey, Wu, et al., 1986; Walker et al., 2004; Wygant et al., 1987). One reason for the scarcity of electric field data is associated with the difficulty of the measurement.

Three methods to handle measurements of the electric field were discussed by Dimmock et al. (2011). The first is to neglect the effects of the spin-axis component by projecting the spin-plane measurements onto the shock normal. This allows evaluation of the field and electrostatic potential when the rotation axis is close to the magnetic field direction. Two other techniques rely on reconstructing the spin-axis component based on assumptions about the electric field structure.

The second technique requires that the electric field component parallel to the magnetic field is zero. In contrast, the third technique supposes that the NIF electric field consists of only two contributions: one from $\boldsymbol{v} \times \boldsymbol{B}$, which is supposed to be constant along the shock crossing, and the other from the electric field along the shock normal. The shock is assumed both planar and stationary, implying that only the magnetic field component perpendicular to the shock normal (i.e. $\boldsymbol{B} \times \boldsymbol{n}$) contributes to $\boldsymbol{v} \times \boldsymbol{B}$, leading to the requirement $\boldsymbol{E} \cdot (\boldsymbol{B} \times \boldsymbol{n}) = 0$. Dimmock et al.

(2011) applied all three techniques to a single shock and reached the surprising conclusion that the different techniques yielded similar values of the potential.

There is also an indirect approach for evaluating the electrostatic potential, based on a theoretical hydrodynamic description of the shock, assuming planarity, stationarity, and no reflected ions. These assumptions are suitable for subcritical, low-Mach shocks. With the additional assumption that the shock transition is smaller than the ion inertial length, in agreement with statistical studies by Hobara et al. (2010) and Mazelle et al. (2010), one can derive simplified proxies for the potential. These proxies are based on ion deceleration, which is mainly determined by the potential in the NI frame. Another proxy may be found from a simplified description of electron dynamics, neglecting the electron mass.

Hereafter we discuss two high-beta, quasi-perpendicular shocks with multipoint observations from the Magnetospheric Multiscale (MMS) mission. MMS is a four-spacecraft constellation, flying in a tetrahedral formation with typical separation distances of tens of kilometers (Fuselier et al., 2016). The primary science goal of MMS is to investigate reconnection processes, but the wealth of data provides ample material for the study of other space plasma phenomena. One of our events of interest is a planar IP shock with low Mach number, and the other is a rippled bow shock crossing with moderate Mach number. For both events, we compare the cross-shock potential profiles obtained from the measurements to proxies computed from the magnetic field data and particle moments.

5.2 Characteristic parameters and data overview

Collisionless shocks in space plasma are characterized by several parameters, computed upstream of the shock, that determine their scales and general behavior:

- The angle θ_{Bn} of the shock normal relative to the background magnetic field;
- Magnetosonic Mach number M_F, the ratio of the flow speed to the characteristic speed of fast magnetosonic waves propagating at angle θ_{Bn} relative to the background magnetic field;
- Ion and electron β, the ratio of particle pressure to magnetic field pressure; and
- The ratio of the Alfvén speed v_A to the speed of light c, $v_A/c = \Omega_i/\omega_i$, where Ω_i and ω_i are the ion gyrofrequency and plasma frequency, respectively.

These parameters form the basis of shock classification. In particular, shocks are divided into two main groups: quasi-perpendicular ($60^\circ < \theta_{Bn} < 90^\circ$), quasi-parallel ($\theta_{Bn} < 40^\circ$), and intermediate ($\theta_{Bn}$ between these extremes). A shock may be considered fully perpendicular if $cos(\theta_{Bn})$ is less than the ratio of electron to ion mass. These limits are not precisely determined. Rather, they are based on the trajectories of particles reflected from the shock front. In quasi-parallel shocks, the reflected particles can infiltrate the upstream flow, whereas in quasi-perpendicular shocks they return to the shock front and eventually cross it.

We present two shocks observed by the four MMS spacecraft: one is an IP shock with low Mach number observed on January 08, 2018 and the other is a bow shock crossing with moderate Mach number observed on November 02, 2017. Magnetic field measurements were obtained from the Fluxgate Magnetometer (FGM) (Torbert et al., 2016), and particle data come from the Fast Plasma Investigation (FPI) (Pollock et al., 2016). While we have performed the analysis using velocity data from both ions and electrons, we ultimately chose the electron velocity because it is

more accurately measured in the solar wind. We used spin-plane electric field measurements (Lindqvist et al., 2016) from three of the MMS spacecraft: MMS 1, 2, and 3. The third component of the electric field was reconstructed from $\boldsymbol{E} \cdot \boldsymbol{B} = 0$ or $\boldsymbol{E_{NIF}} \cdot (\boldsymbol{B} \times \boldsymbol{n}) = 0$ (Dimmock et al., 2011). Additional analysis of the IP shock utilizes magnetic field measurements from the Fluxgate Magnetometers (Auster et al., 2008) on board the two ARTEMIS spacecraft (Angelopoulos, 2011).

No cleaning or filtering was applied to the magnetic field data. The IP shock electron velocity data was sufficiently clean, but the electron velocity data for the bow shock crossing was subjected to low-pass filtering to remove high-frequency fluctuations.

Offsets were applied to the electric field components such that each agreed overall with the features of the solar wind $\boldsymbol{v} \times \boldsymbol{B}$. This electric field data was later used to calculate the cross-shock potentials. We also obtained shock normals from the bow shock electric fields after bandpass filtering.

Oscillations in the form of precursor whistlers and statistical fluctuations in the ion moments are present in the data of both shocks before and after the ramp. Whistlers do not impact the shock geometry, and any effect they have on electrostatic potential occurs outside the ramp. Ion moment fluctuations surrounding the IP shock and preceding the bow shock crossing are most probably spacecraft orientation effects caused by the nonspecific FPI measurement regime in the solar wind. The periodic spikes visible in the IP shock electric field fortunately land on either side of the ramp (the spikes are due to wake effects, which can be mitigated by the algorithm of (Eriksson et al., 2007); see the dotted trace in Figure 5.1c). Finally, in order to shift the electric field from the spacecraft frame to the NI frame, the shock-tangential components of the transformation velocity are obtained from averages of the upstream electron velocity data, which has better statistics in the solar wind and should minimize the effect of oscillations.

5.2.1 IP shock

An IP shock swept past all four MMS spacecraft simultaneously on 2018-01-08 / 06:41:11, while the spacecraft were separated by 15-24km at [4.3, 22.7, -0.6] (GSM coordinates in R_E). An overview of the data is shown in Figure 5.1a-f. (Additional plot of magnetic field components and detailed table of average plasma parameters are included in Appendix A1.) The IP shock had $\theta_{Bn} = (69 \pm 2)^{\circ}$, $\beta_i = 2.8 \pm 0.4$, $\beta_e = 2.3 \pm 0.3$, Alfvén ratio $(1.3 \pm 0.1) \times 10^{-4}$, Alfvén Mach $M_F = 2.3 \pm 0.1$, and magnetosonic Mach number $M_F = 1.1 \pm 0.1$. (However, the upstream ion temperature is likely overestimated by MMS. Ion temperature data from WIND is more reliable and instead yields $\beta_i = 0.3 \pm 0.1$ and $M_F = 1.5 \pm 0.2$, close to the subcritical value.)

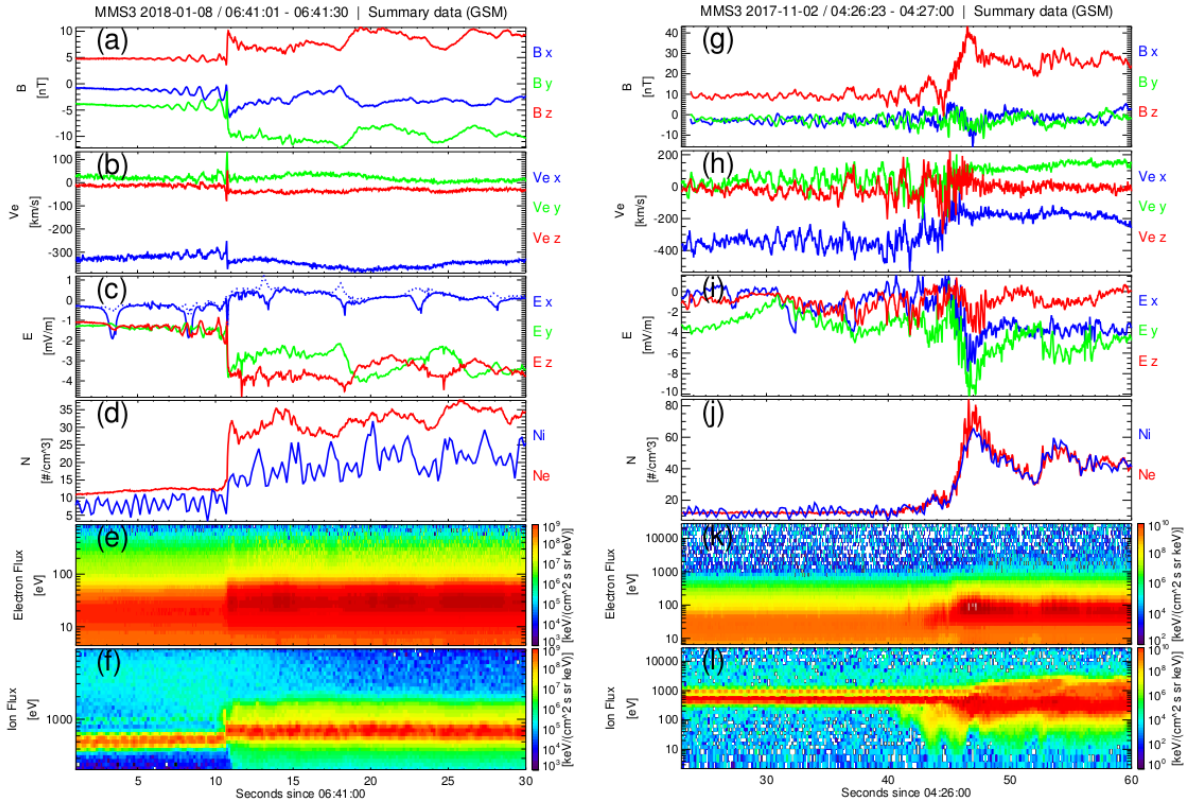

Figure 5.1. Summary of MMS3 data for (a)-(f) IP shock on 2018-01-08 and (g)-(l) bow shock crossing on 2017-11-02. Panels (a), (g): Magnetic field (GSM). Panels (b), (h): Electron velocity (GSM). Panels (c), (i): Electric field (GSM). Panels (d), (j): Ion and electron densities. Panels (e), (k): Ion energy flux. Panels (f), (l): Electron energy flux.

We determined the shock normal in two ways: minimum variance analysis (MVA) and timing analysis of the data from the four satellites. MVA was performed on the magnetic field data from each spacecraft (2018-01-08 / 06:41:07.5 – 14.5). All MVA shock normals were within 10° of the timing analysis shock normal and nearly identical (in the context of the error cone) to each other (see Appendix A1 for details). The second direction of the full set of basis vectors was obtained by projecting the MMS3 average upstream magnetic field onto the plane perpendicular to the shock normal, while the third direction completed the right-handed set.

5.2.2 Bow shock crossing

MMS passed from the solar wind through the bow shock around 04:26:46 on 2017-11-02. At this time, the spacecraft were separated by 23-30km at [24.2, 1.7, 7.0] (GSM coordinates in R_E). An overview of the data is shown in Figure 5.1g-l. All four spacecraft passed together through the ramp. (See plot of magnetic field components and detailed table of average plasma parameters in Appendix A1.) The bow shock crossing had $\theta_{Bn} = (85 \pm 5)^{\circ}$, $\beta_i = 1.4 \pm 0.2$, $\beta_e = 1.4 \pm 0.1$, Alfvén ratio $(2.1 \pm 0.1) \times 10^{-4}$, $M_F = 3.5 \pm 0.1$, and $M_F = 2.1 \pm 0.2$.

To estimate the local geometry of the shock surface, maximum variance analysis was performed on the bandpass-filtered electric field data from each spacecraft during the ramp. The

results showed significant deviation from the timing analysis normal, presumably indicating that the shock surface is rippled. Minimum variance analysis on the magnetic field data was unsuccessful (the intermediate and minimum variance components were comparable) because of the significant thickness of the shock structure and strong perturbations in the upstream magnetic field (see Appendix A1 for details).

We opted to use the timing analysis shock normal, with the full set of basis vectors defined in the same way as for the IP shock. The MMS3 upstream magnetic field provided the second direction of the MVA coordinate system because the MMS3 individual shock normal agreed well with the timing analysis result. The magnetic field, filtered electron velocity, and unfiltered electric field data were all rotated into this coordinate system.

5.3 Cross-shock potential

5.3.1 Estimating the cross-shock potential from electric field measurements

The cross-shock potential was estimated first in the Normal Incidence Frame (NIF), where the shock front is at rest and the upstream bulk flow is normal to the shock. The shock velocity becomes the shock-normal component of the transformation velocity, while the components tangent to the shock surface are the average components of the upstream electron velocity. The electron velocity and electric field transform accordingly:

$$\boldsymbol{v_{NI} = v_{MVA} - v_{T,NI}},$$

$$\boldsymbol{E_{NI} = E_{MVA} + v_{T,NI} \times B},$$

where $\boldsymbol{v_{T,NI}}$ is the constant transformation velocity and the electric field is unfiltered.

We integrated the shock-normal component of the electric field over the ramp, obtaining cross-shock potentials for both shocks (see Table A1.5 in Appendix A1 for details). Two reconstructions of the MMS3 electric field were applied: $\boldsymbol{E \cdot B} = 0$ and $\boldsymbol{E_{NIF} \cdot (B \times n)} = 0$ (Dimmock et al., 2011), although strictly speaking the latter is only expected to be valid for low-Mach shocks. However, even for the IP shock, the second reconstruction was hindered by the shock geometry: because the magnetic field is often aligned with the spacecraft axis, solving for the electric field axial component can lead to division by numbers near zero. Unrealistically large fluctuations are the result, with a cross-shock potential at least twice as large as the value obtained by assuming $\boldsymbol{E \cdot B} = 0$. Thus, while the technique is theoretically well justified (Dimmock et al., 2011), we found it inapplicable in our study, yielding unrealistic electric field magnitudes due to the natural constraints of the inversion procedure. Therefore, we only show the potentials from $\boldsymbol{E \cdot B} = 0$.

We also attempted to transform the data from the spacecraft frame to the HT frame, using the procedure outlined in section 9.3.1 of Khrabrov and Sonnerup (1998). While this transformation minimizes the motional electric field in the upstream region, in the shock ramp the potential due to the motional electric field exceeds the potential of the measured electric field, and we did not pursue the transformation further. However, examination of the magnetic field-aligned electron distributions can often provide an alternative estimate of the HT frame potential (Lefebvre et al., 2007).

5.3.2 Potential proxies from moments and magnetic field

We computed four proxies of the electric potential (Gedalin & Balikhin, 2004):

$$\Phi_v = 1 - v_i^2/\langle v_{i,up}\rangle^2$$
$$\Phi_n = 1 - \langle n_{i,up}\rangle^2/n_i^2$$
$$\Phi_P = 1 - \left(1 - \frac{(P_i - \langle P_{i,up}\rangle) + (P_e - \langle P_{e,up}\rangle) + (B^2 - \langle B_{up}\rangle^2)/2\mu_0}{m_i\langle n_{i,up}\rangle\langle v_{i,up}\rangle^2}\right)^2$$
$$\Phi_e = \frac{-1}{e}\int \frac{1}{n_i}\frac{\partial}{\partial z}\left[\frac{B_x^2 + B_y^2}{2\mu_0} + P_e\right] dz$$

In the above equations, Φ_v is derived from ion velocity, Φ_n from ion density, Φ_P from balancing thermal and magnetic pressures, and Φ_e from the electron equation of motion. Thus, v_i is ion velocity along the shock normal, n_i is ion density, P_i is ion thermal pressure, P_e is electron thermal pressure, B is magnetic field magnitude, m_i is ion mass, e is positive elementary charge, and B_x and B_y are the magnetic field components perpendicular to the shock normal. Averaged quantities $\langle X_{up}\rangle$ are computed upstream.

5.3.3 IP shock

Timing analysis provided a shock velocity of (330 ± 30) km/s in the spacecraft frame. The shock ramp passed over MMS3 in 0.1s. From this, we found the length of the shock crossing to be (33 ± 3) km, smaller than the ion inertial length of about (69 ± 5) km.

Figure 5.2a-d shows the MMS3 proxies and potential (similar plots for MMS1 and MMS2 are available in Appendix A1). The reflected ions (accelerated to ~3-7 keV) seen upstream in Figure 5.1e comprise less than 0.05 of the total ion density and thus do not spoil the ion proxies. Their density slowly decays in the upstream direction, and reflected ions are seen at distances up to $8R_E$ ahead of the shock. This indicates a large-scale planarity of the IP shock. The IP shock velocity and planar geometry were confirmed on the large scale (~$60R_E$) by ARTEMIS (THB and THC spacecraft) measurements in a vicinity of the Moon. THB was at [-8.9, -57.1, 4.2] (GSE coordinates in R_E) and observed the IP shock crossing at 06:50:09 (see Figure A1.4 in Appendix A1). THC was at [-7.1, -58.8, 4.5] and observed the IP shock crossing at 06:49:53.

The extreme brevity of the shock crossing prevents us from drawing conclusions about the proxies dependent upon ion moments, which have a sampling period similar to the ramp observation. The proxy in Figure 5.2c depends only on electron moments and shows a flat approach to and smooth increase during the ramp, on the order of (42 ± 10) V. The observed NIF potential in Figure 5.2d is roughly (24 ± 6) V for MMS3. A similar trend is apparent for MMS1 and MMS2 (see Table A1.5 in Appendix A1).

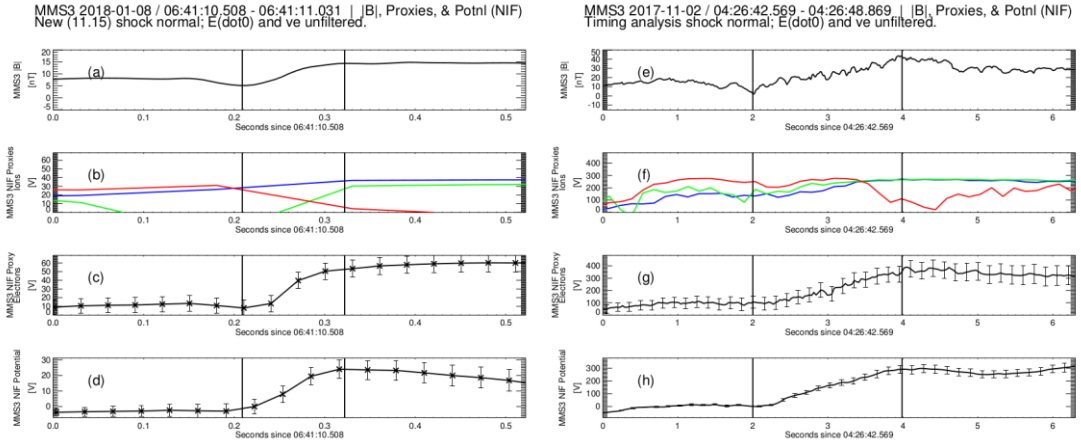

Figure 5.2. MMS3 magnetic field magnitude, potential proxies, and cross-shock potential for (a)-(d) IP shock on 2018-01-08 and (e)-(h) bow shock crossing on 2017-11-02. The ramp is marked by vertical lines through all panels. Panels (a), (e): Magnetic field magnitude. Panels (b), (f): Potential proxies that depend on ion moments: Φ_v from ion velocity (blue), Φ_n from ion density (green), and Φ_P from pressure balance (red). Note that Φ_P depends on the pressure due to electrons as well as ions. Panels (c), (g): Potential proxy that does not depend on ion moments: Φ_e from electron equation of motion. Panels (d), (h): Cross-shock potential in NIF. Error bars for all points are shown in Panels (c) and (d). For the sake of visual clarity, error bars for only one fifth of the points in Panels (g) and (h) are shown.

5.3.4 Bow shock

The NIF potentials varied between 290 V and 440 V for the different spacecraft measurements (see Table A1.5 in Appendix A1). The field-aligned electron distributions allowed estimation of the HT frame potential: the width of the flat top downstream corresponded to a potential of about (150 ± 20)V.

The shock velocity from timing analysis was (60 ± 10) km/s in the spacecraft frame, and the ramp passed over MMS3 in approximately 2 seconds, giving an approximate shock length of (120 ± 20) km. Although this is larger than the ion inertial length of about (65 ± 1) km, we computed potential proxies for this event as well. Before discussing the proxies, it is important to point out some features of the ion distributions. Figure 5.3b shows ion distributions measured by MMS3 at the bow shock, with two slices before (upstream) and one slice after (downstream) the shock ramp. The coordinate system is centered on the spacecraft. The ions are effectively demagnetized and their motion is stable with respect to the spacecraft. All polar angles have been combined; the angular position in the plot represents azimuthal angle in the spin plane.

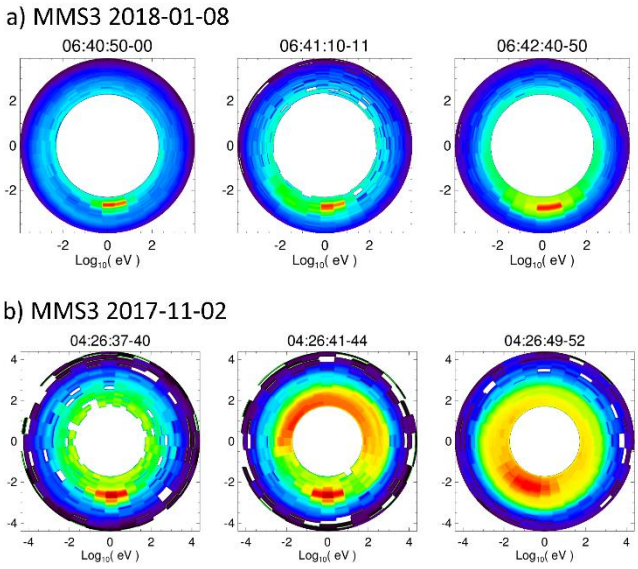

Figure 5.3. The MMS3 ion distributions in energy and azimuthal angle for (a) IP shock crossing on 2018-01-08 and (b) bow shock crossing on 2017-11-02. Time ranges shown are upstream (left), spanning the IP shock ramp or just preceding the bow shock ramp (center), and downstream (right).

In the far-upstream distribution of Figure 5.3b, the solar wind is visible as a concentrated beam in energy and angle. The near upstream distribution, showing a time range shortly before the ramp, shows not only the localized solar wind beam but also a lower-energy population traveling in the opposite direction with large angular spread. These are ions reflected from the positive electrostatic potential in the shock front. In the downstream plot, ions are observed at all angles and lower energies, indicating that they have been decelerated while passing through the ramp.

For comparison, the ion distributions from the IP shock are plotted in Figure 5.3a. The lowest available energy bin for the IP shock distributions was around 200eV because the four spacecraft were operating in solar wind mode. The time ranges shown are upstream, spanning the ramp, and downstream. No clear indication of reflected ions is seen, but the energy cut-off may introduce some uncertainty.

Figure 5.2e-h shows the proxies and potential from MMS3 for the bow shock crossing. (Similar plots for MMS1 and MMS2 are available in Appendix A1.) The detrimental influence of reflected ions during 04:26:41-44 is clearly visible as enhancements in the potential proxies of Figure 5.2f, all of which depend on ion moments. The pressure balance proxy, which depends upon both ions and electrons and is displayed with the ion proxies in Figure 5.2f, is also significantly disturbed downstream of the shock. This is due to downstream electrons reflecting off the shock ramp. In contrast, the proxy determined by the electron equation of motion in Figure 5.2g shows a flat approach to the ramp and a smooth increase on the order of (250 ± 60) V. The observed NIF potential in Figure 5.2h is roughly (290 ± 30) V.

5.4 Discussion and conclusions

The most striking difference between the low and high Mach number shocks was the geometry of the shock surface. The low Mach number IP shock was almost planar on the scale of the MMS inter-spacecraft separation, with the individual normals deviating from the timing analysis normal by less than 10°. In contrast, the high Mach number bow shock exhibited a perturbed surface that was rippled on the scale of the MMS spacecraft configuration. Individual normals deviated from the timing analysis normal by up to 30°. This is presumably a typical feature of high Mach number shocks, in agreement with several past modeling studies of shocks (Burgess, 2006a; Burgess & Scholer, 2007a; Lowe & Burgess, 2003a; Ofman & Gedalin, 2013c, 2013a; Winske & Quest, 1988a) as well as observations reported by Johlander et al. (2016). In particular,

Ofman & Gedalin (2013a, 2013c) discussed the deviation of the shock normal due to rippling, based on their 2D hybrid simulation study. The geometry of our observations is sketched in Figure 5.4, which shows the bow shock surface, with the electric field MVA normal in red at each spacecraft. A ripple in the shock surface helps reconcile the individual normals.

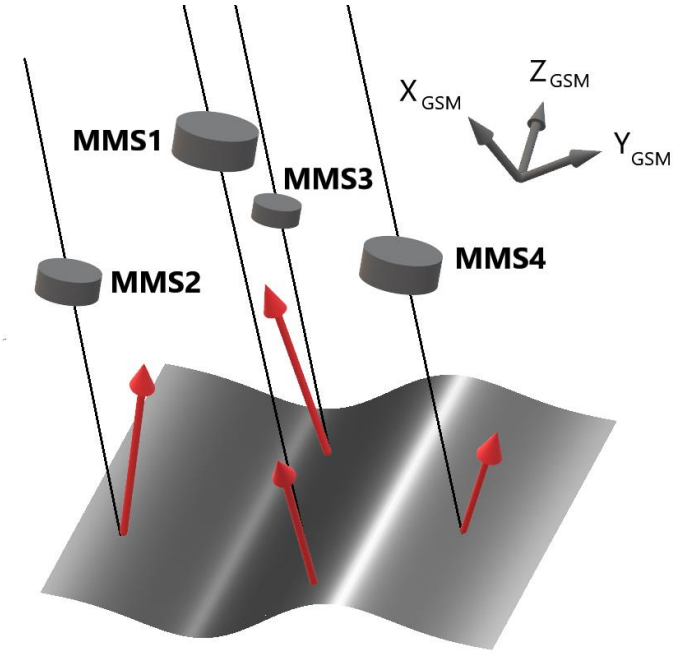

Figure 5.4. Shock geometry. The shock normal vectors from MVA of electric field data are shown for MMS 1-4; the shaded surface is a sketch reconciling the shock normals by means of a rippled front. The dominant magnetic field direction approximately coincides with GSM Z. The MMS4 shock normal is estimated from spin-rate electric field data.

To conclude, we present the results of a comparative study of two quasi-perpendicular collisionless shocks in the solar wind, with low (IP shock) and high (bow shock) Mach number:

- The cross-shock NIF potential from electric field measurements is 24-28V for the IP shock (with 41-42V from the electron proxies), and 290-440V for the bow shock (with 240-260V from the electron proxies).
- The ion proxies cannot be used for high Mach number shocks because the ion moments are spoiled by reflected ions before and during the ramp.
- The low Mach number IP shock surface was almost planar on the scale of the MMS spacecraft configuration as well as on the scale of the MMS and ARTEMIS separation distance (~20 R_E).
- The high Mach number bow shock surface was rippled on the scale of the MMS spacecraft configuration, in agreement with the results of Burgess (2006a), Burgess & Scholer (2007a), Lowe & Burgess (2003a), Ofman & Gedalin (2013a, 2013c), and Winske & Quest (1988a) and the observations of Johlander et al. (2016).

From this focused case study, we shifted our perspective and embarked on a statistical study of over 50 bow shock crossings.

Chapter 6
Collisionless Shocks of the MMS Era: Statistics and Parameter Dependence on the Upstream and Downstream Regions

In this chapter we present our second paper (Hanson, Agapitov, Mozer, et al., 2020), a statistical study that was published in the *Journal of Geophysical Research* as a technical report. Vexed by the persistent question, "What are the consequences for our analysis if we choose the upstream or downstream regions poorly?" we set out to quantify the variability in shock and plasma parameters based on specific designations of upstream and downstream regions.

6.1 Scientific background

Early spacecraft observations of collisionless shocks, such as the Earth's bow shock, were limited by low data sampling rates, which made it natural to concentrate on analysis of the macroscopic features and physics (Formisano, Hedgecock, et al., 1973; Formisano, Moreno, et al., 1973; Formisano & Hedgecock, 1973; Kennel et al., 2013; Leroy et al., 1982). As instrument technology has advanced, providing increasingly detailed data within the shock transition, observational studies have expanded to include waves (e.g. Balikhin et al., 2005; Breneman et al., 2013; Hobara et al., 2008; Hull et al., 2006, 2012; Lobzin et al., 2005; Oka et al., 2017; Vasko et al., 2018; Walker et al., 2008; Wilson III et al., 2014b; Wilson III et al., 2017), electric fields (e.g. Bale et al., 2005, 2008; Bale & Mozer, 2007; Balikhin et al., 2002; Cohen et al., 2019; Dimmock et al., 2011, 2012; Formisano, 1982; Hanson et al., 2019; Heppner et al., 1978; Hobara et al., 2010; Lefebvre et al., 2007; Scudder, Mangeney, Lacombe, Harvey, & Aggson, 1986; Scudder, Mangeney, Lacombe, Harvey, Aggson, et al., 1986; Scudder, Mangeney, Lacombe, Harvey, Wu, et al., 1986; Walker et al., 2004; Wygant et al., 1987), and nonstationarity and rippling (e.g. Burgess, 2006; Burgess & Scholer, 2007; Johlander et al., 2016; Lobzin et al., 2007; Lowe & Burgess, 2003; Ofman & Gedalin, 2013a, 2013b; Winske & Quest, 1988). Missions that have been utilized for collisionless shock studies include ISEE (e.g. Sckopke et al., 1983), Intershock (e.g. Walker et al., 1999), AMPTE (e.g. Balikhin et al., 1999), Cluster (Artemyev et al., 2013; Bale et al., 2005; Kis et al., 2013; Krasnoselskikh et al., 2013; Kruparova et al., 2019), THEMIS (e.g. Hobara et al., 2010; Wilson III et al., 2014a, 2014b), Polar (e.g. Bale & Mozer, 2007; Hull et al., 2006, 2012), and Wind (e.g. Wilson III et al., 2012; Wilson III et al., 2017), among others. Whether a given study inclines more to the macroscopic or the microscopic view, situating a given shock within the context of previous work still involves estimation of average plasma parameters before and after the shock, in the so-called upstream and downstream regions.

Identification of the upstream and downstream regions in an idealized theoretical context, or even in a self-contained simulation environment, is a relatively straightforward matter. From an observational perspective, the low sampling rates of measurements used in early studies necessitated averaging over long periods of minutes before and after the shock (e.g. Formisano, Hedgecock, et al., 1973; Newbury et al., 1998). Advances in spacecraft measurement technology have resulted in sophisticated measurements at much higher cadences, with the curious consequence that identifying data appropriate for the upstream and downstream averages can be a dilemma. Kennel et al. remarked that analysis of jump conditions using the Rankine-Hugoniot

(RH) relations required choosing two states "separated by a distance greater than the longest dissipative scale length" (1985), while Viñas & Scudder noted that no standard procedure existed for selecting data representative of the upstream and downstream states (1986).

In this paper we endeavor to collect and articulate some of the common wisdom behind such choices. We then put these guidelines into practice by selecting four possible combinations of upstream and downstream regions for each of a set of 51 shocks observed by the Magnetospheric Multiscale (MMS) mission. By comparing the shock parameters derived from different combinations of upstream and downstream regions, we seek to estimate the reliability of the parameters as well as the possible consequences of choosing different stream regions.

Summary plots and detailed parameter tables for each shock are provided in a separate Supplement, freely available at https://doi.org/10.5281/zenodo.3583341.

6.2 Data

Our database consists of 51 bow shock crossings recorded by the MMS mission. MMS is made up of four spacecraft launched in March 2015 to orbit the Earth in a 3D tetrahedral configuration, with inter-spacecraft separations on the order of tens of kilometers (Fuselier et al., 2016). The elliptical orbit remains within 25° of the ecliptic plane, with an early apogee of ~$12R_E$ that was later increased to $25R_E$ (Fuselier et al., 2016). Originally designed to probe reconnection physics in the vicinity of the Earth, the MMS mission has yielded a rich abundance of high-resolution data that lends itself well to probing other physics (Burch et al., 2016). We selected shock events by their magnetic field magnitude variation, and the majority of them (48 shocks or ~94%) are reasonably robust, with a few exceptions we retained for the sake of curiosity. The particle moments were gathered by the Fast Plasma Instrument (FPI) (Pollock et al., 2016), while the magnetic field measurements were taken by the Fluxgate Magnetometers (FGM) (Torbert et al., 2016). In order to ensure that we had ample flexibility in our choice of upstream and downstream regions for each shock, we limited ourselves to the Fast Survey particle moments (4.5s resolution) and magnetic field data (62.5ms resolution). Burst data is available for 24 of the 51 shocks, with ion moments at 150ms, electron moments at 30ms, and magnetic field vectors at 8ms (Pollock et al., 2016; Torbert et al., 2016).

6.3 Rankine-Hugoniot solution method

The observations from each spacecraft, for each shock, were handled independently. Estimation of the shock parameters required the magnetic field vector dynamics, particle velocity moment vector, and particle density. We processed the electron velocity and density, because solar wind electrons form a more isotropic distribution than the beam-like solar wind ions and thus can be measured with greater reliability by electrostatic analyzers (Hanson et al., 2019). The cadence of the electron moments (4.5s) is longer than that of the magnetic field vectors (62.5ms).

Two adjacent groups of 1000 time stamps (62.5s each) were then chosen from the upstream side of the shock and also the downstream side. Thus, there were four combinations of upstream and downstream regions. For a given combination of upstream and downstream time intervals, the magnetic field Minimum Variance Analysis (MVA) normal and the Slavin and Holzer (SH) model (Slavin & Holzer, 1981) normal were computed for comparison with the RH result. All these

methods of shock normal estimation are meticulously described by Schwartz in a chapter about shock geometry and parameters (1998). For the cases we processed, the normals obtained from MVA were similar to those derived from RH Analysis. A limited search area, with angular resolution of 1° in azimuth and polar angles, was defined in order to lessen the risk that both orientations of the shock normal would be present within the search area, as this could introduce problematic ambiguity.

For each shock, each spacecraft, each combination of upstream and downstream intervals, and each possible pair of GSM azimuth and polar angles in the search area, a normal vector was defined by the direction of the given azimuth and polar angle pair. The shock speed v_{sh} for each of 100 ensembles at a given azimuth and polar angle pair was computed from the continuous normal flow constraint. We checked the conservation of magnetic field and transverse momentum flux across the shock surface, but we omitted the transverse electric field (from the cross product of velocity and magnetic field) because it yielded poorly-defined minima.

The errors in conservation were normalized by averages taken across both upstream and both downstream regions: errors due to the magnetic field were normalized by the average magnetic field magnitude, while errors due to momentum flux were normalized by the sum of the average ion kinetic energy and magnetic energy. The normalized errors were rescaled to range between 0 and 1 and then added to yield a total error.

The average normal vector and shock speed for the ensemble was determined by identifying the minimum total error using the averages over the entire upstream and downstream ranges. With these two critical pieces of information – the shock normal and shock speed – we determined other shock and plasma parameters of interest for each pair of upstream and downstream regions, for each spacecraft, for each shock.

6.4 Setting initial boundaries for appropriate stream times

In order to choose upstream and downstream boundaries, we examined a plot of time-series data with the following panels: magnetic field magnitude, magnetic field vector, ion and electron density, ion energy flux, ion parallel and perpendicular temperature, electron energy flux, and electron parallel and perpendicular temperature. For most, but not all, shocks in our database, the ramp was observed within fractions of a second by all four spacecraft. In the event that the shock ramp observations do not coincide, special care must be taken to select upstream or downstream boundaries suitable for the individual spacecraft data.

In the upstream and downstream regions alike, there are certain features that should be captured or avoided. These features are summarized in Table 6.1, while examples of the phenomena described are shown in Figure 6.1.

	Upstream	Downstream
$\|B\|$	We want to see a smooth, nearly flat approach to the ramp. Small fluctuations are unavoidable and generally innocuous, but avoid plateau-like formations. Subjectivity enters here in judging how high is too high for such a plateau. The	Large-amplitude fluctuations in |B| are normal, but if they appear periodic, they may be wave-like activity rather than random oscillations. Periodic structures indicate that the plasma has not yet reached an equilibrium downstream state. Identifying, and avoiding, any overshoot

	gradual increase in $\|B\|$ preceding the ramp, i.e. the foot, should also be excluded when visible.	and undershoot is likewise not always simple: hence some of the value of comparing multiple downstream options.
B	The individual components of ***B*** should exhibit a smooth, flat approach to the ramp.	Any obvious, sustained rotation is to be avoided.
Density	The ion and electron densities should be smooth and flat while nearing the ramp.	The ion and electron densities should have stabilized into a comparatively flat signal after the ramp. During the overshoot or undershoot, they may continue to rise or fall slowly; this remains a region to avoid.
Energy Flux	The ion energy flux is particularly useful for refining the allowed boundaries of the upstream region. In the upstream, we want to see only the steady, comparatively narrow beam of the incoming solar wind. Features to watch out for and exclude are any significant population outside the solar wind beam energy range preceding the ramp, such as reflected ions. A similar caveat applies to the electrons, but this is rarely an issue.	The ion energy flux should settle into a broader signal, but concentrated populations of higher- or lower-energy ions may be visible near or immediately after the ramp. These will often appear correlated with irregular behavior in the temperature or density data, but not necessarily with the magnetic field data, which is why it is important and useful to include the particle moments when establishing upstream and downstream boundaries.
Temperature	The ion and electron parallel and perpendicular temperatures should be flat and steady for an extended period preceding the ramp. However, irregularities rarely occur in isolation: temperature enhancements ahead of the ramp often accompany non-solar-wind populations in the ion energy flux.	The remarks about the densities are relevant to the ion and electron temperatures, whose behavior may appear erratic for a little while after the ramp.

Table 6.1. Characteristics in summary data that can guide the selection of appropriate upstream and downstream regions for a shock observation.

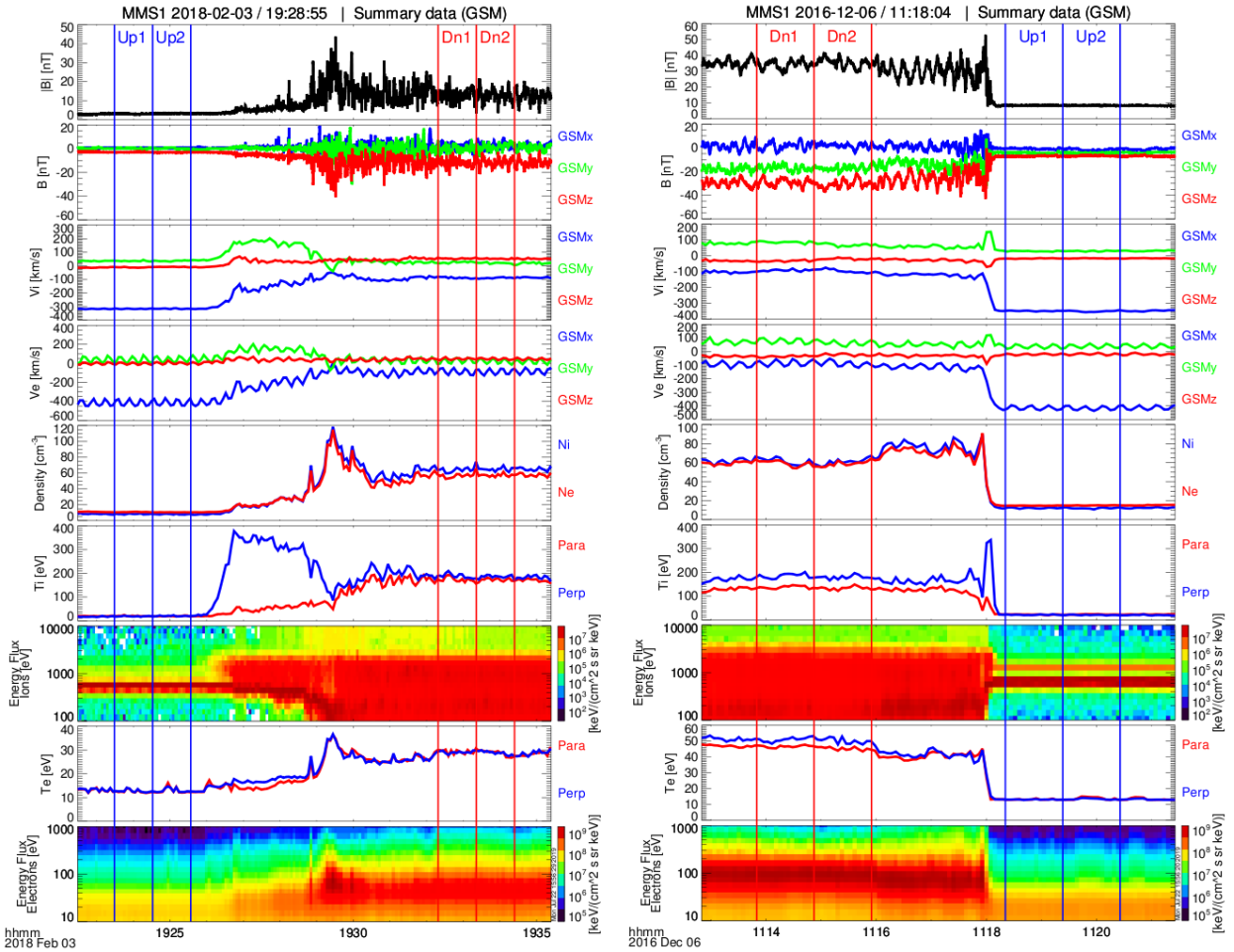

Figure 6.1. Summary data from MMS1 for two shocks: 03 February 2018 (left) and 06 December 2016 (right). Each shock includes the following panels from top to bottom: magnetic field magnitude, magnetic field vector, ion velocity, electron velocity, ion and electron density, ion parallel and perpendicular temperatures, ion energy flux, electron parallel and perpendicular temperatures, and electron energy flux. Vertical blue (red) lines indicate the two chosen upstream (downstream) regions, which are adjacent and non-overlapping. The 03 February 2018 (left) shock shows a good example of a foot in the magnetic field, accompanied by gradients in the particle moments, a strong enhancement in the ion perpendicular temperature, and the presence of an ion energy flux population distinct from and having higher energy than the incoming solar wind. The upstream regions were selected ahead of all these features. After the ramp, the magnetic field, particle densities, and electron temperatures of the same shock show an overshoot that overlaps with an enhanced population of high-energy ions. It is less clear where the plasma has returned to its new, downstream equilibrium, but the downstream time ranges were selected to avoid the most salient features of the ramp and overshoot. In the 06 December 2016 (right) data, upstream phenomena are not so prolonged, and the upstream time regions may be situated closer to the ramp observation. However, fluctuations in the downstream magnetic field look much more likely to be oscillations in this case, so the downstream regions were chosen after these oscillations fade into a more chaotic signal.

6.5 Algorithm and metrics

In order to designate the preferred upstream and downstream combination, we judge the RH conservation error from the magnetic field and the momentum flux. For each probe, the RH conservation errors corresponding to the four upstream and downstream range combinations were compared. The minimum error and the maximum standard deviation were both identified; all errors within one standard deviation of the minimum were identified as contenders to be preferred for that probe. The number of preferred designations for each upstream/downstream combination (0 if it was not a contender for any probe, or 4 if it was a candidate for all probes) were then compared and the maximum number of preferred designations identified. Two scenarios were possible:

(a) Only one upstream/downstream combination had the maximum value, which was at least 2, indicating that two or more spacecraft were in agreement as to the preferred upstream/downstream combination.

(b) Two or more upstream/downstream combinations had the maximum value. Of these competing preferred combinations, the one chosen was the one that most closely sandwiched the shock ramp (near upstream and near downstream, if available). In the event that the only two viable preferred options were the near/far and far/near combinations, the chosen option was the one with the near upstream.

In this way we established preferred upstream and downstream regions for each shock. The shock-normal magnetic field component can be seen in Figure 6.2, which shows the magnetic field magnitude and vector for the same shock crossings as in Figure 6.1. Here, the components of the magnetic field vector are defined by the shock normal direction and the average upstream magnetic field perpendicular to the shock normal, with the third component chosen to complete the right-handed triad. The normal magnetic field component stays roughly constant (on average) during the shock crossing, which indicates good estimation of the shock normal direction.

Thereafter it was necessary to estimate the robustness of each shock, which we did using the shock velocity v_{sh}, shock angle θ_{Bn}, and normal deviation angle. For the shock speed v_{sh} and angle θ_{Bn}, we first computed the average of the absolute differences between the parameter value for the preferred stream combination and the parameter value for the other combinations. The average difference in the normal was estimated by averaging the deviation angle between the normal vector of the preferred upstream and downstream regions and the normal vector of the other stream region combinations. The robustness of any given parameter was taken to be the average difference normalized by the corresponding standard deviation.

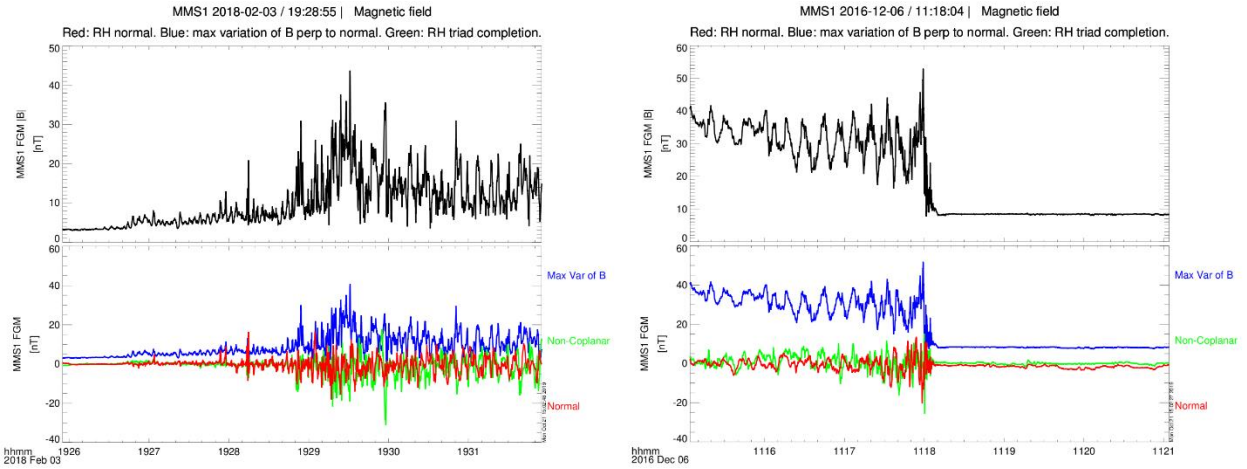

Figure 6.2. Magnetic field magnitude (top panels) and vector components (bottom panels) from MMS1 for the same two shocks shown in Figure 6.1: 03 February 2018 (left) and 06 December 2016 (right). In both plots, the bottom panel presents the magnetic field vector in a coordinate system defined by the shock normal (red) and the average upstream magnetic field component perpendicular to the shock normal (blue). The third component (green) completes the right-handed triad.

6.6 Description of results and database

We selected 51 bow shock crossings observed by MMS between September 2015 and March 2018. The vast majority of shocks selected are quasi-perpendicular. All bow shock crossing locations are shown in Figure 6.3, where the symbols are color-coded by the angle θ_{Bn} between the shock normal and the average upstream magnetic field (left panel), by the maximum angular separation between the SH normal and the preferred RH normals for the four probes (center panel), and by the standard deviation between the probes' preferred RH normals (right panel). The distribution of all shocks is illustrated in Figure 6.4, where the histograms on the left show the spread of Alfvén Mach number (Panel (a)) and the downstream-to-upstream ratio of the magnetic field (Panel (b)). The scatter plots on the right show shock angle plotted against local time (Panel (c)) and the magnetic field compression ratio plotted versus Alfvén Mach number (Panel (d)).

In Table A2.1 of Appendix 2, we summarize some basic parameters for each shock. More detailed parameter tables and a summary plot of each shock are given in the Supplement, not reproduced within this document but freely available at https://doi.org/10.5281/zenodo.3583341.

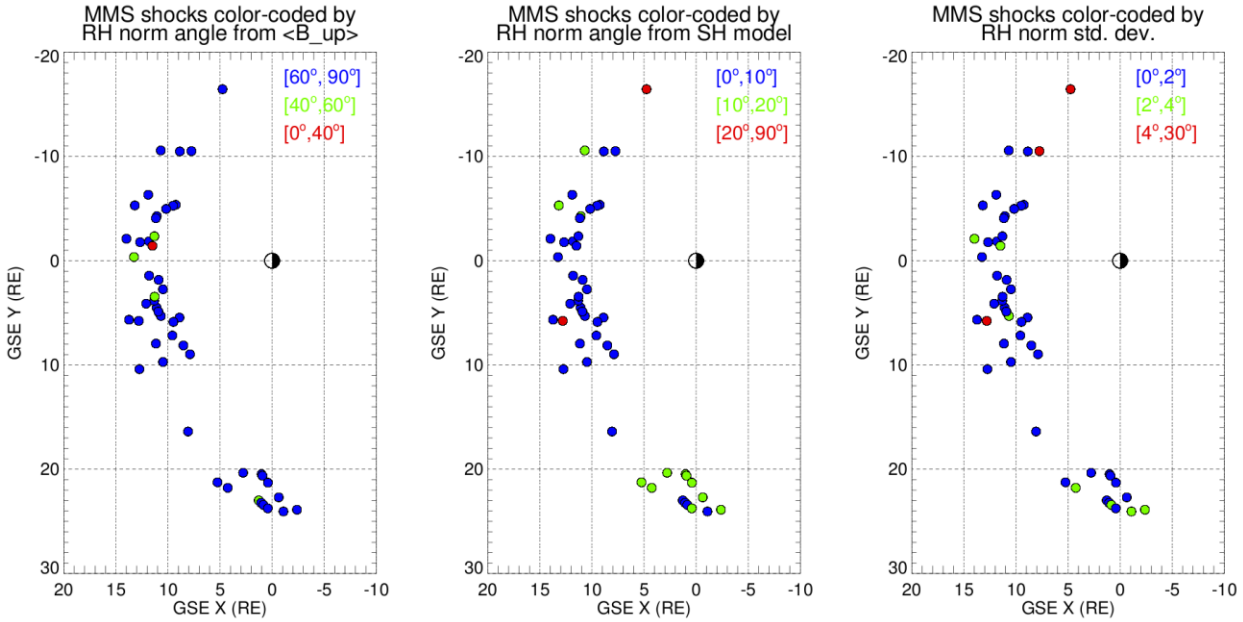

Figure 6.3. GSE x- and y-coordinates of observed bow shock crossings, in units of Earth radii. In the left panel, symbol colors indicate the angle θ_{Bn} between the shock normal and the average upstream magnetic field (dark blue: 60°-90°, green: 40°-60°, and red: 0°-40°). In the center panel, symbol colors indicate the maximum angle of deviation between the SH model normal and the preferred RH normals for each MMS probe (dark blue: 0°-10°, green: 10°-20°, and red: 20°-90°). In the right panel, symbol colors indicate the standard deviation of the preferred RH normals for the four MMS probes (dark blue: 0°-2°, green: 2°-4°, and red: 4°-20°). Larger discrepancies between the normals of each probe may indicate non-stationarity or rippling in the shock.

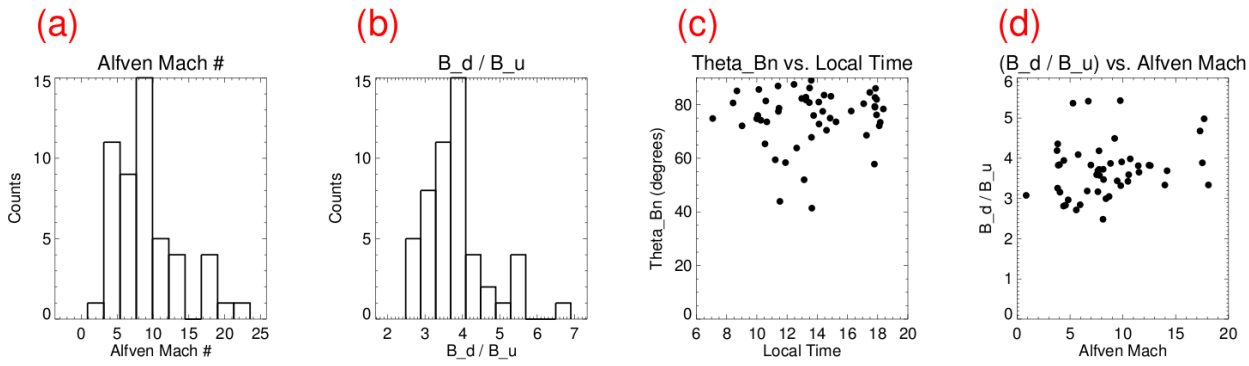

Figure 6.4. Left two plots: histograms showing the distribution of Alfvén Mach number (a) and downstream-to-upstream magnetic field compression ratio (b) for the full database of 51 shocks. The Alfvén Mach number is calculated in the Normal Incidence Frame (NIF) for all ions in the solar wind beam. Right two plots: scatter plots showing shock angle vs. local time (c) and magnetic field compression ratio vs. Alfvén Mach number (d).

6.7 Discussion and conclusions

The values of the parameters are of secondary interest to us in this case; we are most interested in assessing their robustness. In Tables 6.2-4, we have assembled a breakdown of the shock statistics by the standard deviation, average differences, and normalized differences for key parameters. The standard deviations are consistently low throughout the database; they are summarized in Table 6.2. The standard deviation in the normal vector is less than 3° for 89% of shocks in the database, while for over 90% of shocks, the standard deviation in the shock speed is less than 10 km/s. The standard deviation in θ_{Bn} is less than 2° for over 95% of the database. These standard deviations result solely from the analysis and do not account for experimental or instrumental sources of error.

In Table 6.3, the average difference thresholds are expressed in the dimensions of each parameter, representing the average shift to be expected from switching from the preferred stream region combinations to any other combination. The parameters of most shocks in the database would exhibit only modest differences if a different combination of stream regions were chosen: 90% of all shocks would experience less than 5° change in the normal vector, 71% would experience less than 15km/s change in speed, and 85% would experience less than 5° change in shock angle.

We gain an alternative understanding by normalizing the average differences of each shock's parameters by their respective standard deviations σ, as shown in Table 6.4. From this perspective, it is apparent that the amount by which each shock's parameters might change are generally larger than the standard deviation, suggesting that, small absolute differences notwithstanding, a shift of the upstream and/or downstream regions produces a parameter profile that is separate and distinct. This effect is least pronounced in the case of the normal, which would remain within 1σ for 22% of shocks and within 3σ for 86%. Only 8% (60%) of shocks exhibit less than 1σ (3σ) change in shock angle θ_{Bn}. The least robust parameter is the shock speed: 78% of shocks would change by more than 3σ if the upstream and/or downstream regions were shifted. The amount of robustness required in any given parameter depends on the intended topic of study.

Because the angular resolution of the possible normals in the RH analysis is 1°, the standard deviation in the normals must be at least 1° as well. That such a high proportion of the database has low standard deviations (less than 3° for the normal, less than 10km/s for the speed, and less than 2° for the shock angle) provides a reassuring testimonial to the utility of RH analysis for our purposes. Of greater interest in the context of this paper are the consistently low average differences in all parameters across the database, which indicate that little change is to be expected from selecting different preferred stream regions for the majority of shocks in the database. While this is reassuring, some visual attention is still required when designating boundaries for upstream and downstream regions, and the strategy outlined in Table 6.1 may be helpful. Having chosen a shock for further study, performing RH analysis on an ensemble of randomly-chosen points will typically yield parameters that are self-consistent within reasonably small errors. Instrumental and systematic effects must be taken into account separately, while comparison of a few stream region combinations helps not only to identify optimal upstream/downstream combinations but also to confirm the robustness of the parameters. Given that our database is strongly skewed towards quasi-perpendicular shocks, it could be interesting to repeat a similar investigation on a set of quasi-parallel shocks.

Standard Deviations					
Shock normal $\hat{n}$		Shock speed v_{sh}		Shock angle θ_{Bn}	
<3°	>3°	<10km/s	>10km/s	<2°	>2°
90.2%	9.8%	94.1%	5.9%	96.1%	3.9%

Table 6.2. Standard deviation of shock parameters for the preferred stream region combinations.

Average Differences			
Shock normal $\hat{n}$			
<2°	2°-3°	3°-5°	>5°
47.1%	29.4%	13.7%	9.8%
Shock speed v_{sh}			
<5km/s	5-10km/s	10-15km/s	>15km/s
11.8%	35.3%	23.5%	29.4%
Shock angle θ_{Bn}			
<2°	2°-3°	3°-5°	>5°
43.1%	17.6%	23.5%	15.7%

Table 6.3. The average change in parameters between the preferred stream combination and the other combinations.

Normalized Average Differences				
	<1.0	1.0-2.0	2.0-3.0	>3.0
Shock normal $\hat{n}$	21.6%	49.0%	15.7%	13.7%
Shock speed v_{sh}	3.9%	11.8%	5.9%	78.4%
Shock angle θ_{Bn}	7.8%	37.3%	15.7%	39.2%

Table 6.4. The average change in parameters between the preferred stream combination and the other combinations, normalized by the corresponding standard deviation of each individual shock.

Whether we can claim that the results of this study added to our peace of mind is debatable, but we accrued valuable experience in visually assessing and selecting upstream and downstream regions for quasi-perpendicular shocks. From here we returned to the IP shock, where some unfinished business in the ion distributions was beckoning.

Chapter 7
Shock Drift Acceleration (SDA) of Ions: Theory, Test-Particle Simulation, and Experimental Evidence

Here we treat our third paper (Hanson, Agapitov, Vasko, et al., 2020), a study of accelerated ions that persisted for a surprisingly long time ahead of the IP shock featured in Chapter 5. This brief study was published in *The Astrophysical Journal Letters*, as mechanisms of ion acceleration in collisionless plasma shocks are of interest in astrophysics as well as space physics.

7.1 Scientific background

Collisionless shocks, which effect the transition from upstream to downstream plasma states over a length scale far smaller than the collisional mean free path, appear throughout the universe and play an important role in shaping the emissions of supernovae and accelerating cosmic rays (Biermann et al., 2018; Gargaté & Spitkovsky, 2012). They also feature prominently in the heliosphere, for instance as planetary bow shocks and interplanetary (IP) shocks. Their prevalence has historically made planetary environments and the solar wind valuable hunting grounds for shock studies that are based upon *in situ* measurements, from space missions such as ISEE (e.g. Sckopke et al., 1983), Intershock (e.g. Walker et al., 1999), AMPTE (e.g. Balikhin et al., 1999), Cluster (e.g. Artemyev et al., 2013; Bale et al., 2005; Hobara et al., 2010; Kis et al., 2013; Krasnoselskikh et al., 2013; Kruparova et al., 2019; Mazelle et al., 2010), THEMIS (e.g. Hobara et al., 2010; Wilson et al., 2014b, 2014a), Polar (e.g. Bale & Mozer, 2007; Hull et al., 2006, 2012), and Wind (e.g. Wilson et al., 2012; Wilson III et al., 2017).

One of the primary consequences of passage through a shock transition is deceleration and increased thermalization of the incoming ions. The cross-shock electric field potential impacts the distribution functions of both ions and electrons (Goodrich & Scudder, 1984) and may contribute to ion reflection, but hitherto investigations of the electric field and electrostatic potential in collisionless shocks have been sparse due to the challenges of making *in situ* measurements. Fortunately, recent missions such as Magnetospheric Multiscale (MMS) are expanding our horizons with observations of unprecedented resolution (Burch et al., 2016; Fuselier et al., 2016).

Gradients within the shock transition may give rise to the phenomenon of shock drift acceleration (SDA), where ions travel along the shock front and gyrate through the ramp multiple times before either passing into the downstream or escaping into the upstream region (Armstrong et al., 1985; Decker & Vlahos, 1985; Pesses et al., 1982). When ions have been accelerated by SDA, they may pass downstream or escape upstream, but the highest-energy ions are expected to be found upstream (Armstrong et al., 1985). SDA is distinct from but has been included in models for diffusive shock acceleration (DSA) because both mechanisms act on particles drifting along the shock front within a small distance (on the order of the ion gyroradius) of the ramp (Jokipii, 1982). Ion acceleration models that rely upon time spent within the strong field gradients of the shock transition are not limited to the solar wind but have also been discussed within the context of interstellar pick-up ions and the heliospheric termination shock (Lee et al., 1996; Zank et al., 1996). Both SDA and DSA are invoked in more general astrophysical cases as well, particularly to explain observations of cosmic rays and supernova remnants (Biermann et al., 2018; Caprioli

& Spitkovsky, 2014; Gargaté & Spitkovsky, 2012; Ohira, 2016; Park et al., 2015; Zank et al., 2015). Lario et al. (2019) have described IP shock observations where enhancements in ions less than 10 keV appeared close to the shock. Similarly, ion populations of ~20 keV associated with an IP shock have been recorded by the ARTEMIS spacecraft (Kajdič et al., 2017). In this paper we report experimental evidence of SDA in a population of 2-7 keV ions observed ahead of an IP shock.

7.2 Data

The MMS mission boasts a full complement of high-resolution instruments for *in situ* plasma measurements (Burch et al., 2016; Fuselier et al., 2016). Ion and electron distributions and moments were obtained from the Fast Plasma Investigation (FPI) (Pollock et al., 2016). We checked the heavy ion observations from the Hot Plasma Composition Analyzer (HPCA) (Young et al., 2016), but within our interval of interest there was insufficient data for us to draw conclusions. The Fluxgate Magnetometer (FGM) provided magnetic field measurements (Russell et al., 2016; Torbert et al., 2016), while high-frequency (AC), 3D electric fields are measured by the Axial and Spin-Plane Double Probe electric field instruments (Ergun et al., 2016; Lindqvist et al., 2016; Torbert et al., 2016).

7.3 Overview of the interplanetary shock

The four MMS spacecraft recorded an IP shock on 2018 January 8 (magnetic field data and solar wind bulk velocity are shown in Figure 7.1a and 7.1b, respectively). The IP shock crossed the spacecraft at 330 km s^{-1} in the spacecraft frame at 06:41:11. The distance between individual MMS probes ranged from 15 km to 24 km at the time of observation (Hanson et al., 2019). An overview of the Fast Survey and Burst data is shown in Figure 7.1. The cross-shock potential for this quasi-perpendicular, low-Mach shock has been estimated to be near 25V based on electric field measurements (Cohen et al., 2019; Hanson et al., 2019). This IP shock was recorded later by the two ARTEMIS spacecraft (Angelopoulos, 2011; Auster et al., 2008), and the combined observations of MMS and ARTEMIS suggested that the shock front was nearly planar on a spatial scale of 60 Earth radii (R_E) (Hanson et al., 2019). The angle between the shock normal and the upstream magnetic field was 69°, and the magnetosonic Mach number was 1.1 (1.5 if ion temperatures from Wind are used in the calculation) (Hanson et al., 2019).

A population of the upstream ions reflected by the shock (less than 5% of the total upstream solar wind density) consisted of nearly-specularly reflected ions (Cohen et al., 2019) and ions accelerated to energies between 3 keV and 7 keV (Hanson et al., 2019). The specularly reflected ions, which appear for a few tenths of a second in the upstream region ~150 km ahead of the shock ramp (highlighted by the frame in Figure 7.1h), are seen as an enhancement in the Sun-directed flux of ions in the energy flux near 1 keV, described in detail by Cohen et al. (2019).

The ion population of interest to this paper (highlighted in Figure 7.1e) is seen as a broad, faint band between 2 keV and 5-7 keV, slowly decaying with distance from the ramp in the upstream direction until it reaches the noise level. It is strongest during 06:40:00-06:41:15 but is still clearly present as early as 06:37:50, several RE ahead of the shock. The upper bound of energy increases closer to the shock front. The flux of ions in the accelerated energy range decreases by a

factor of about four downstream, within a distance comparable to the Larmor radius of a 2-7 keV proton. Here, a brief enhancement of 0.2-2 keV ion flux is observed (Figures 7.1e, f, h). Observations of the accelerated ions in the upstream so far from the shock were possible due to the planar shock structure, narrow ramp, and relatively small angle between the upstream magnetic field and the shock normal (Cohen et al., 2019; Hanson et al., 2019), as well as the steady upstream magnetic field. Enhancements of a similar energy range but lower flux are visible even farther ahead of the ramp in Figure 7.1b (e.g. 06:27-06:33), but it is unclear whether these are due to the shock or to other solar wind phenomena.

Figure 7.2 illustrates the wave fields in the vicinity of the shock front for the magnetic field magnitude and the high-frequency electric field component parallel to the magnetic field. In Figure 7.2b, which shows the wavelet of the magnetic field GSM x-component, low-frequency whistler waves (0.5-2Hz) are evident, extending for ~2000 km on either side of the front. The strongest fluctuations are centered near 1Hz, and the phase (group) speed is 184 km s^{-1} (370 km s^{-1}). It is important to note that the group speed is comparable to the shock speed of 330 km s^{-1} because this enables the whistler waves to continue running ahead of the ramp without escaping easily.

Both wavelets indicate significant activity near the shock: large-scale whistler wave precursors (electromagnetic) just upstream and electrostatic wave activity in the ramp. The electrostatic waves most likely represent some combination of ion-acoustic waves, lower hybrid waves, and bipolar structures with wavelengths on the order of a few Debye lengths (Gurnett, 1985; Hull et al., 2006; Vasko et al., 2018). Although the electrostatic waves may contribute to the pitch angle scattering of electrons (Vasko et al., 2018), they are highly inefficient for scattering or accelerating protons. In some cases, whistler waves may lead to efficient acceleration of protons (Kis et al., 2013). For this particular shock, protons cannot be accelerated by the observed whistler and electrostatic waves. The magnetic field and plasma pressure gradients are insufficient for phase trapping in the whistler wave (Artemyev et al., 2013), while the wavelength of the electrostatic waves (~1 km) differs by about two orders of magnitude from the proton Larmor radius (~300 km), rendering trapping and acceleration impossible.

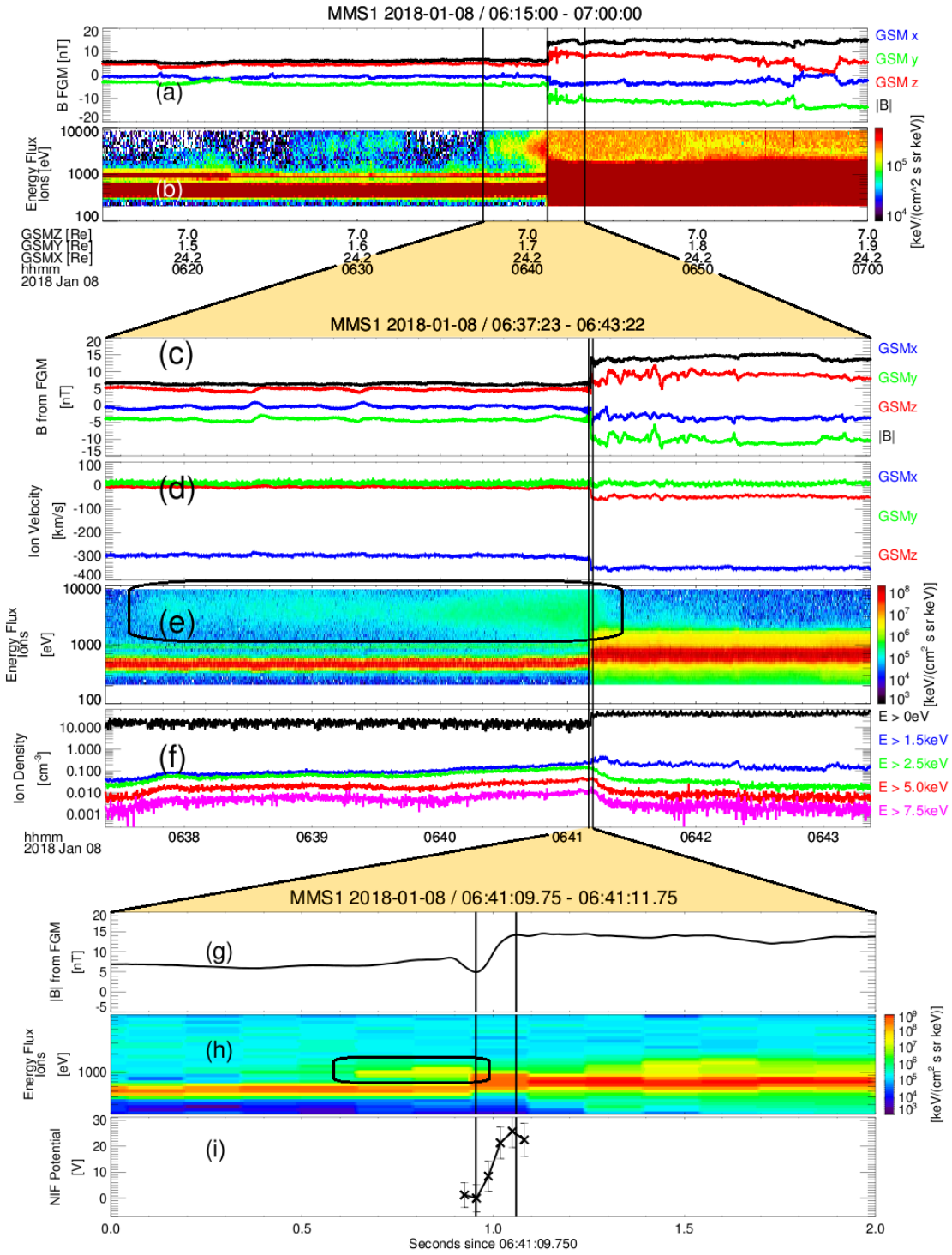

Figure 7.1. Summary of IP shock observation by MMS1 in Geocentric Solar Magnetic (GSM) coordinates. Panels (a)-(b) show Fast Survey data in the time range 06:15-07:00, panels (c)-(f) show the burst-rate data, which covers 06:37:23-06:43:22, and panels (g)-(i) present 2s of burst-rate data around the ramp. (a) and (c) Magnetic field vector and magnitude; (b), (e), (h) ion energy flux with different color scales; (d) ion velocity vector; (f) ion density split by several minimum energy thresholds; (g) magnetic field magnitude; (i) cross-shock potential.

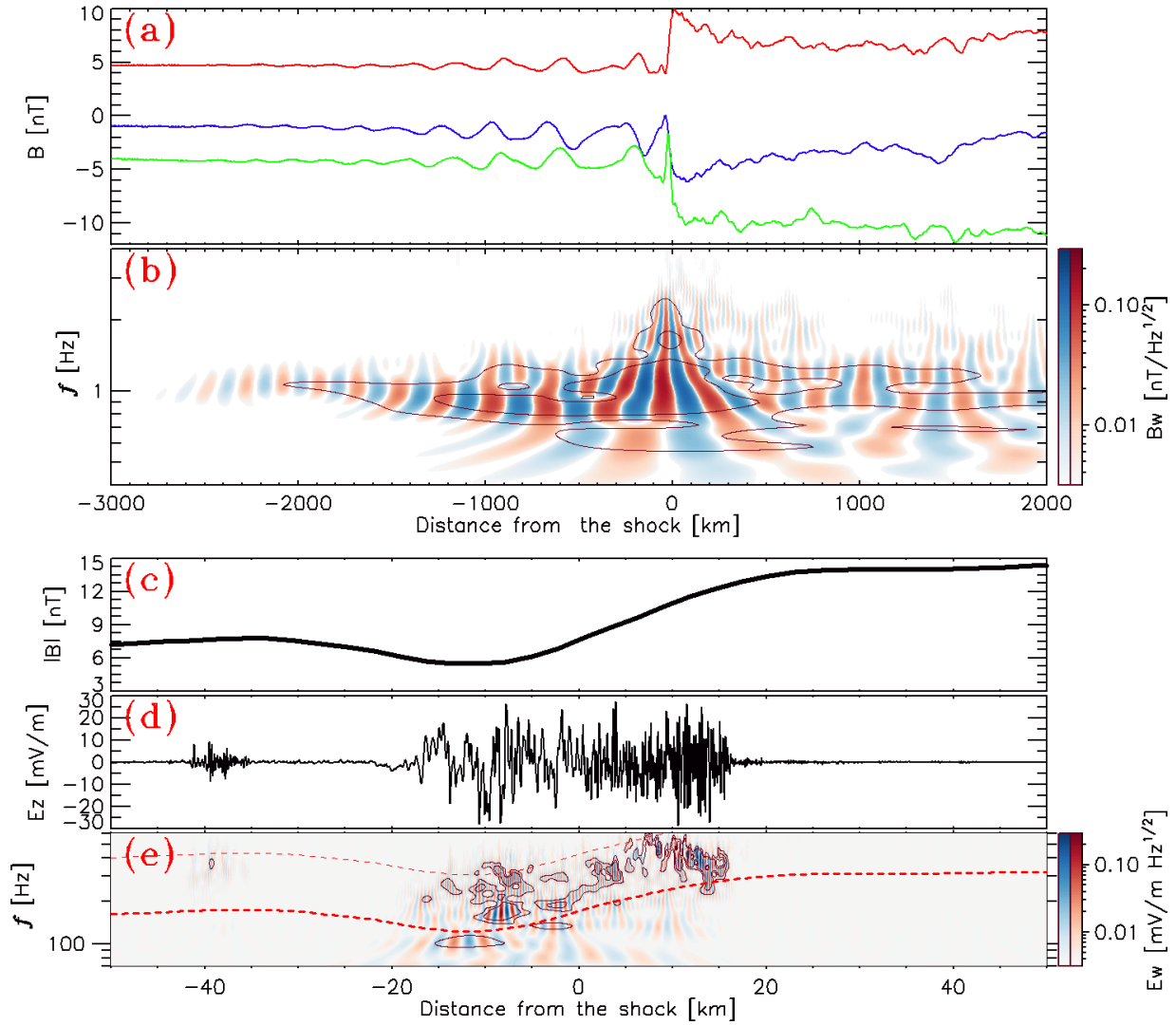

Figure 7.2. Wave activity surrounding the shock front in the spacecraft frame from MMS4 observations. Time has been scaled by the shock speed to present distance from the shock in the horizontal axes. Panels (a) and (b) extend 3000 km ahead of the shock and 2000 km behind it, and Panels (c)-(e) span 50 km on either side of the shock. (a) GSM components of magnetic field; (b) Morlet wavelet of the GSM x component of the magnetic field, showing whistler waves surrounding the shock. The wavelet amplitude is represented by the black contours, while red (blue) indicate positive (negative) values of the wavelet's real part; (c) magnetic field magnitude; (d) component of AC electric field parallel to the magnetic field; (e) Morlet wavelet of the parallel electric field, indicating lower hybrid wave activity within the ramp. The contours and color scale are the same as described in Panel (b). The red dashed (dotted) curve indicates 0.8 (2) times the electron cyclotron frequency.

7.4 Accelerated ions preceding the IP shock

The ion density, subdivided by minimum energy thresholds in Figure 7.1f, shows that ions with energy in excess of 1.5 keV comprise less than 1-2% of the total ion density throughout the observation. While the total ion density upstream of the shock remains nearly constant at 20 cm^{-3}, the higher-energy ions experience increasing density starting from about 06:37:50 (3min 20s ahead of the ramp). For all but the highest-energy ions (those with energy greater than 7.5 keV), this increase is monotonic until the shock front is encountered. The density of the highest-energy ions dips temporarily around 06:39:20-06:40:20 (1min 50s to 50s ahead of the ramp).

The density of all ions with energy exceeding 2.5 keV drops rapidly (on the scale of the ion gyroradius) once the shock front has passed. The density profile for ions with energy greater than 1.5 keV behaves differently: for ten seconds after the passage of the shock, the density jumps by a factor of two. Ions in the energy range 1.5-2.5 keV, presumably a combination of accelerated protons and compressed alpha particles, must be responsible for this phenomenon since no such jump is evident in the profiles for energies over 2.5 keV.

The panels of Figure 7.3 show three different plots for each of three time periods surrounding the shock. Figures 7.3a, 7.3d, and 7.3g present data from a far upstream region, before the accelerated ions appear (3min 47s to 3min 25s ahead of the ramp, or 06:37:23-45UT). Figures 7.3b, 7.3e, and 7.3h show observations taken in the near upstream region when the accelerated ions are most strongly visible (1min 10s to 9s ahead of the ramp, or 06:40:00-41:01UT). Finally, the downstream region is shown in Figures 7.3c, 7.3f, and 7.3i (49s to 2min 11s behind the ramp, or 06:42:00-43:22UT). Figure 7.3a-c presents profiles of ion differential energy flux (DEF) versus energy for three distinct time periods surrounding the shock. Figure 7.3d-f shows the angular distribution of ions in the Despun spacecraft Body Coordinate System (DBCS; (Pollock et al., 2016)), where particles appearing in 0° or 360° in azimuth have come from the direction of the Sun, and the ecliptic plane is near 90° in polar angle. The filled contours indicate where ions of a given energy flux exceed a minimum threshold. In Figure 7.3g-i, the ion DEF is shown in pitch angle versus energy.

The far upstream observations are typical of quiet solar wind conditions. In Figure 7.3a, the incoming solar wind population is dominated by a narrow beam of protons in the energy range 400-500 eV, while the alpha particles form a peak two orders of magnitude smaller in the energy range 0.9-1 keV. In Figure 7.3d, only the narrow, localized solar wind beam is evident, coming towards the spacecraft from the Sun. Similarly, in Figure 7.3g the solar wind protons form a strong, concentrated beam near a pitch angle of 90° in all panels, with a weaker beam at the same angle but higher energy for the alpha particles.

The downstream panels hold no surprises either. After the passage of the shock front, the DEF profile has changed significantly, as is shown in Figure 7.3c. Here the dominant proton beam has increased in peak DEF and broadened in energy to 600-700 eV. The alpha particles no longer form a separate beam but are subsumed in a higher-energy shoulder jutting out from the broadened solar wind beam. The DEF drops off rapidly with increasing energy beyond about 1.5keV. Figure 7.3f shows that the solar wind beam is still the dominant population, but it has a much larger angular spread than in Figure 7.3d. This broadening is also evident in Figure 7.3i, where the solar wind beam peaks at the same pitch angles as in Figure 7.3g but is significantly spread in both pitch angle and energy, with a higher peak energy.

It is in the upstream panels nearest the ramp that the most interesting features appear. In Figure 7.3b, the solar wind proton and alpha particle peaks are nearly the same as in Figure 7.3a,

but a broad beam has appeared in energies above 1 keV. For particles with energies between 2 keV and 5 keV, the total density is near 0.5 cm^{-3}. The DEF of this near upstream, high-energy peak is less than the solar wind protons by two orders of magnitude but comparable to the alpha particles, and greater than the far-upstream ions of the same energy by a factor of 3-5. Figure 7.3e shows that the solar wind beam has been joined by a new population of high-energy ions, moving in an azimuthal direction similar to the solar wind but offset in polar angle. The high-energy ions also exhibit a larger angular spread in comparison with the incoming solar wind. The solar wind and helium populations of Figure 7.3h look much the same as in Figure 7.3g, but in Figure 7.3h, the accelerated ions are seen as an enhancement for pitch angles between 90° and 150° and energies above ~2 keV. Note that the accelerated ions are more persistent at angles more aligned with the magnetic field, and only the highest-energy ions are able to access more perpendicular pitch angles. Particles that undergo SDA escape along the direction of the magnetic field before they are returned to the solar wind population.

We performed a test particle simulation with the observed shock parameters to verify that SDA can explain the accelerated protons' energy and pitch angle distributions. From the simulation data, we obtained the phase space density and DEF of protons in the spacecraft frame (see Appendix 3 for a detailed description). The DEF of incoming protons and protons accelerated by SDA and escaping upstream is shown in Figure 7.4a, while Figure 7.4b presents the DEF of protons in the downstream region. The distributions in Figures 7.4a-b are in a similar format as the experimental data in Figure 7.3a-c. We can see that the protons accelerated by the SDA are observed as a peak of DEF at energies of 1-2 keV and their DEF is 2-3 orders of magnitude less than the incoming population, consistent with the observations in Figure 7.3b. We stress that the actual acceleration of protons is up to 7 keV (see Figure A3.1b in Appendix 3), but for the considered Maxwellian distribution of the incoming protons, the phase space density and DEF of these protons is quite small. Figures 7.4c-d present the DEF of protons in the upstream and downstream regions in dependence on the energy and pitch angle. Comparison to Figures 7.3h-i shows that the simulations well reproduce the DEF of incoming protons and protons in the downstream regions, i.e. the peak of the DEF is around 90° and around 500 eV in the upstream region and around 700 eV in the downstream region. Most interestingly, the simulations show that the protons accelerated by SDA and escaping to the upstream region are observed in a narrow range of pitch angles of 120°-135°, which is quite consistent with the observations in Figure 7.3h. The test-particle simulations demonstrate that the upstream protons are accelerated within the shock front by the SDA process, explaining both the energies of the accelerated protons as well as their narrow pitch angle distribution.

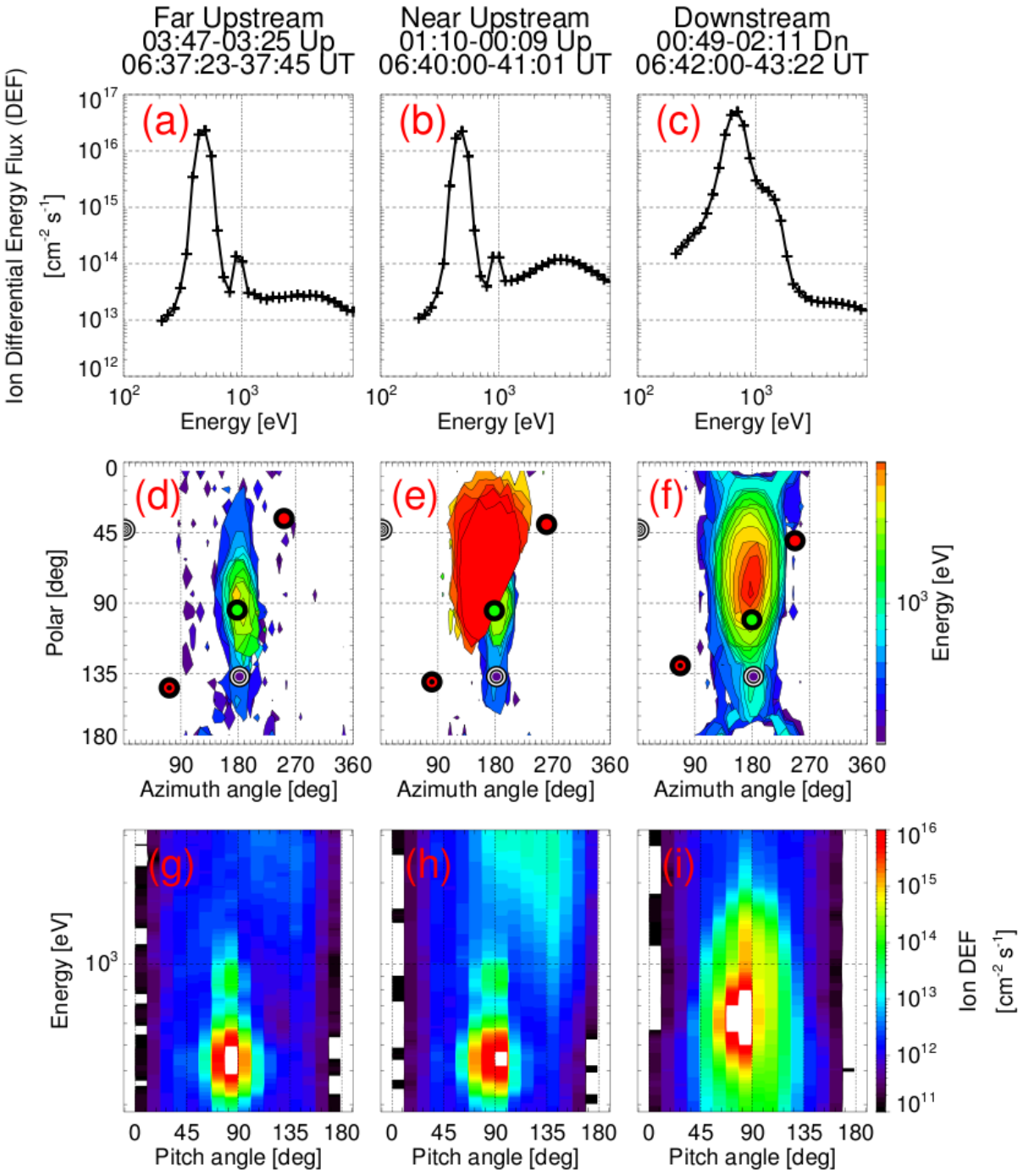

Figure 7.3. Panels (a)-(c) are profiles of DEF versus energy. Panels (d)-(f) show the angular locations where the energy flux at a given energy exceeds a minimum threshold. The coordinates are azimuthal angle (x-axis) and polar angle (y-axis) in the Despun spacecraft Body Coordinate System (DBCS). Panels (g)-(i) show ion distributions in energy and pitch angle with respect to the magnetic field. Panels (a), (d), and (g) display data averaged over a far upstream time range (06:37:23-45 UT, or 3min 47s to 3min 25s ahead of the shock); panels (b), (e), and (h)

show the near upstream (06:40:00-41:01 UT, or 1min 10s to 0min 9s ahead of the shock); and panels (c), (f), and (i) show the downstream (06:42:00-43:22 UT, or 0min 49s to 2min 11s after the shock). In panels (d)-(f), the azimuthal angle 180° points away from the Sun, and the polar angle 90° is approximately aligned with the ecliptic plane. The red circle indicates the direction of the magnetic field, while the red circle with a small black dot in the center shows the opposite. Similarly, the green dot at the right edge of the plot represents the average solar wind direction. The shock normal is represented by a purple dot surrounded by concentric black and white rings, and black and white rings with no central dot indicate the opposite direction.

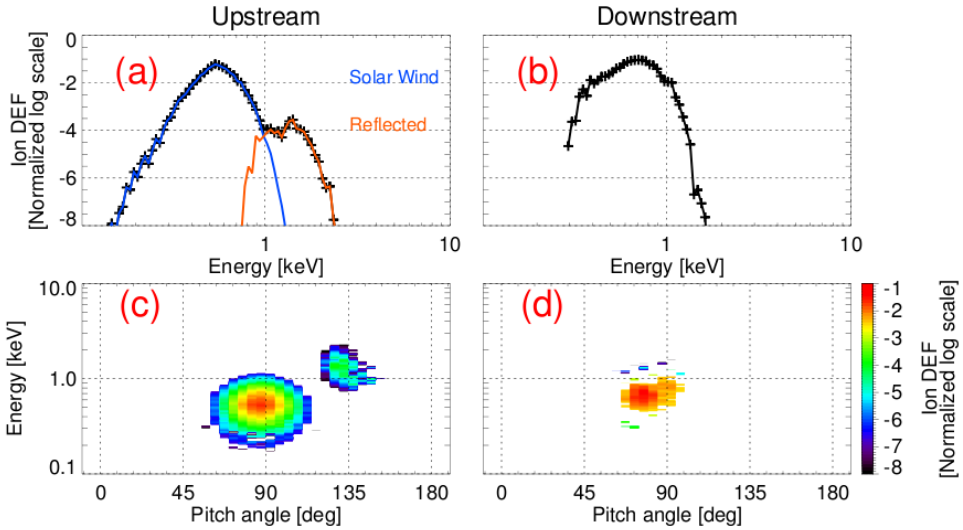

Figure 7.4. Panels (a)-(b) show the proton DEF profiles in the simulation upstream and downstream regions, respectively; compare the upstream (downstream) panel to Figure 7.3b (7.3c). The blue curve is the incoming solar wind, and the orange curve is the reflected population, which peaks at 1-2 keV. Panels (c)-(d) give the proton DEF versus energy and pitch angle for the upstream and downstream regions, respectively; compare the upstream (downstream) panel to Figure 7.3h (7.3i). The reflected protons are concentrated around pitch angles of 120°-135°. Simulation DEF units are logarithmic and normalized to the total DEF of the downstream protons.

7.5 Summary and conclusions

An IP plasma shock wave was recorded by the four MMS spacecraft on 2018 January 8. The plasma measurements provided evidence of ion acceleration from ~0.5 keV (solar wind ions) to 2-7 keV. These accelerated ions were observed to be injected into the plasma upstream of the IP shock, preceding the ramp by about three minutes (~8000 km) and decaying slowly in the upstream direction. In the downstream region, the flux of 2-7 keV ions falls by a factor of about four compared to the flux just before the ramp. Their energy range exceeds that of the solar wind protons and alpha particles, and though they travel in nearly the same azimuthal direction with respect to the spacecraft as the solar wind beam, they are slightly offset in polar angle and exhibit a broader angular distribution.

The shock itself is surrounded by wave activity: in addition to whistler precursors, there are short-scale electrostatic waves in the upstream and downstream regions as well as in the ramp. These waves were processed from the perspective of their impact on ions, and it was determined that the waves cannot provide the observed acceleration. The electrostatic waves have wavelengths too small compared to the ion gyroradius to provide the observed acceleration, and acceleration due to whistlers would require a large population of reflected particles at low energies.

The mechanism of SDA, in which the ions are incrementally accelerated along the component of the electric field parallel to the shock front during repeated crossings of the ramp, has been shown to be capable of accelerating the 2-7 keV ions and reflecting them upstream. The pitch angle distribution of the accelerated ion population (the higher-energy ions have larger pitch angles) is consistent with this mechanism; similar features are also seen in the test-particle simulation.

We note that ions are accelerated by a factor of five to ten in their interaction with this low-Mach, quasi-perpendicular IP shock. Since Mach numbers for astrophysical shocks are generally much higher, correspondingly greater acceleration of ions should be possible.

Having set our lingering curiosity about this IP shock to rest, we have many options for future work. In particular, we still have an entire database of shocks that are already half analyzed, though not all of them include measurements taken at the maximum temporal resolution. The database accumulated in the course of our statistical study offers a rich hunting ground from which to extract a new analysis project.

Chapter 8
Conclusions

In the course of two case studies and a statistical analysis, we have probed macroscopic shock physics ranging from measurements of cross-shock potential and ion acceleration to the dependence of shock parameters on variations in the designation of upstream and downstream regions bracketing the shock.

The cross-shock potential was derived from spin-plane electric field measurements, completed with the $\boldsymbol{E} \cdot \boldsymbol{B} = 0$ assumption, for two shocks observed by the MMS mission. These two shocks were instructive partly thanks to their differences from each other: we compared a rippled, moderate Mach number ($M_F = 2.13$) bow shock crossing to a highly planar, low Mach number ($M_F = 1.1$) IP shock. The cross-shock potential of the bow shock ranged between 290V and 440V, depending on which spacecraft provided the data, while the IP shock was estimated to be 26V. Proxy computations based on the electron momentum equation gave cross-shock potentials near 250V for the bow shock and 40V for the IP shock (Hanson et al., 2019). Both shocks lent themselves well to multiple methods of determining the shock normal, with reflected ions appearing in very different guises in each shock (Cohen et al., 2019; Hanson et al., 2019).

Taking a step back for the statistical study, we developed an automated algorithm that implemented RH analysis on a collection of 50+ bow shock observations. Two possible upstream and downstream regions were chosen by eye for each shock in the database. We then compared the resulting variation in key output parameters when different upstream and downstream regions were used in the analysis, with four possible combinations for each shock. Key parameters shifted by more than one standard deviation if either stream region was altered. Common strategies for defining reasonable upstream and downstream regions were articulated for readers' reference (Hanson, Agapitov, Mozer, et al., 2020).

We then returned our attention to the IP shock, which was characterized not only by nearly specularly reflected ions (Cohen et al., 2019), but also by an intriguing population of higher-energy (2-7keV) ions persisting for about three minutes upstream of the shock front (Hanson, Agapitov, Vasko, et al., 2020; Hanson et al., 2019). Comparison with a test-particle simulation confirmed our hypothesis that this population was accelerated and reflected as a result of shock drift acceleration (SDA) in the ramp (Hanson, Agapitov, Vasko, et al., 2020).

All these studies have concentrated on the processing and analysis of *in situ* measurements from a recently launched multi-spacecraft constellation. Shock physics was not the main driver for the development of the MMS mission, but thanks to the design of its orbit it has provided an abundance of high-quality, high-resolution data collected during bow shock crossings.

It is worth emphasizing and acknowledging that the bulk of the shocks analyzed here are quasi-perpendicular, exhibiting the comparatively distinctive phenomenology of upstream, foot, ramp, possible over- and undershoot, and downstream. These clear observations are particularly well suited to the kind of macroscopic studies we have performed. In contrast, the subtle or even indistinguishable blending of waves and reflected particles typical of quasi-parallel shocks significantly complicate the picture, making it difficult or impossible to identify the ramp, let alone what occurs in its vicinity. Ions reflected by quasi-perpendicular shocks may be more limited in their impact on the observations because the magnetic field does not provide so direct a path away and outward from the shock front.

Our work leaves open a number of doors for further study. By far the most difficult would be to assess the feasibility of repeating a similar statistical study of upstream and downstream regions for quasi-parallel shock observations. However, the inherent difficulty of even pinpointing the ramp in a quasi-parallel shock raises the question of whether this is the most useful paradigm for understanding quasi-parallel shock structure.

A more fruitful option is to sift through the shocks in our database for features and patterns worth quantifying. Why is ion reflection so much more obvious in some cases? How does the observed ion reflection depend upon shock or plasma parameters? In how many other shocks can we reliably estimate the cross-shock potential? What waves do we see upstream and downstream of the shocks, and how are these correlated with features in the particle distributions? How much rippling is evident? Do we see ion or electron acceleration in any of these bow shock observations? If so, what are the most probable mechanisms?

We certainly suffer from no shortage of interesting avenues of inquiry. Better still, the shock geometry and characteristic parameters have already been calculated as a byproduct of our statistical study.

Bibliography

Angelopoulos, V. (2011). The ARTEMIS Mission. *Space Science Reviews*, 165(1–4), 3–25. https://doi.org/10.1007/s11214-010-9687-2

Armstrong, T. P., Pesses, M. E., & Decker, R. B. (1985). Shock drift acceleration. In B. T. Tsurutani & R. G. Stone (Eds.), *Geophysical Monograph Series, Vol. 35*, pp. 271–285. Washington, D. C.: American Geophysical Union. https://doi.org/10.1029/GM035p0271

Artemyev, A. V., Agapitov, O. V., & Krasnoselskikh, V. V. (2013). Cyclotron resonance in plasma flow. *Physics of Plasmas, 20*(12), 124502. https://doi.org/10.1063/1.4853615

Auster, H. U., Glassmeier, K. H., Magnes, W., Aydogar, O., Baumjohann, W., et al. (2008). The THEMIS Fluxgate Magnetometer. *Space Science Reviews*, 141(1–4), 235–264. https://doi.org/10.1007/s11214-008-9365-9

Axford, W. I. (1962). The interaction between the solar wind and the Earth's magnetosphere. *Journal of Geophysical Research, 67*(10), 3791–3796. https://doi.org/10.1029/JZ067i010p03791

Bale, S. D., & Mozer, F. S. (2007). Measurement of Large Parallel and Perpendicular Electric Fields on Electron Spatial Scales in the Terrestrial Bow Shock. *Physical Review Letters, 98*(20). https://doi.org/10.1103/PhysRevLett.98.205001

Bale, S. D., Balikhin, M. A., Horbury, T. S., Krasnoselskikh, V. V., Kucharek, H., Möbius, E., et al. (2005). Quasi-perpendicular Shock Structure and Processes. *Space Science Reviews*, 118(1–4), 161–203. https://doi.org/10.1007/s11214-005-3827-0

Bale, S. D., Mozer, F. S., & Krasnoselskikh, V. V. (2008). Direct measurement of the cross-shock electric potential at low plasma β, quasi-perpendicular bow shocks. *ArXiv:0809.2435 [Astro-Ph, Physics:Physics]*. Retrieved from http://arxiv.org/abs/0809.2435

Balikhin, M., Walker, S., Treumann, R., Alleyne, H., Krasnoselskikh, V., Gedalin, M., et al. (2005). Ion sound wave packets at the quasiperpendicular shock front. *Geophysical Research Letters, 32*, L24106. https://doi.org/10.1029/2005GL024660

Balikhin, M. A., Alleyne, H. St.-C. K., Treumann, R. A., Nozdrachev, M. N., Walker, S. N., & Baumjohann, W. (1999). The role of nonlinear interaction in the formation of LF whistler turbulence upstream of a quasi-perpendicular shock. *Journal of Geophysical Research, 104*(A6), 12525–12535. https://doi.org/10.1029/1998JA900102

Balikhin, M. A., Nozdrachev, M., Dunlop, M., Krasnosel'skikh, V., Walker, S. N., Alleyne, H. St. C. K., et al. (2002). Observation of the terrestrial bow shock in quasi-electrostatic subshock regime. *Journal of Geophysical Research: Space Physics, 107*(A8), 1155. https://doi.org/10.1029/2001JA000327

Baumjohann, W., & Treumann, R. A. (2012). *Basic Space Plasma Physics*. Revised Edition. London: Imperial College Press.

Biermann, P. L., Becker Tjus, J., de Boer, W., Caramete, L. I., Chieffi, A., Diehl, R., et al. (2018). Supernova explosions of massive stars and cosmic rays. *Advances in Space Research, 62*(10), 2773–2816. https://doi.org/10.1016/j.asr.2018.03.028

Breneman, A. W., Cattell, C. A., Kersten, K., Paradise, A., Schreiner, S., Kellogg, P. J., et al. (2013). STEREO and Wind observations of intense cyclotron harmonic waves at the Earth's bow shock and inside the magnetosheath: Bow shock cyclotron harmonic waves.

Journal of Geophysical Research: Space Physics, 118(12), 7654–7664. https://doi.org/10.1002/2013JA019372

Burch, J. L., Moore, T. E., Torbert, R. B., & Giles, B. L. (2016). Magnetospheric Multiscale Overview and Science Objectives. *Space Science Reviews, 199*(1–4), 5–21. https://doi.org/10.1007/s11214-015-0164-9

Burgess, D. (1995). Collisionless shocks. In M. G. Kivelson and C. T. Russell (Eds.), *Introduction to Space Physics* (pp. 129–163). Cambridge, UK: Cambridge University Press.

Burgess, D. (2006). Simulations of Electron Acceleration at Collisionless Shocks: The Effects of Surface Fluctuations. *The Astrophysical Journal, 653*(1), 316–324. https://doi.org/10.1086/508805

Burgess, D., & Scholer, M. (2007). Shock front instability associated with reflected ions at the perpendicular shock. *Physics of Plasmas, 14*(1), 012108. https://doi.org/10.1063/1.2435317

Burgess, D., & Scholer, M. (2015). *Collisionless Shocks in Space Plasmas: Structure and Accelerated Particles*. Cambridge, UK: Cambridge University Press.

Caprioli, D., & Spitkovsky, A. (2014). Simulations of ion acceleration at non-relativistic shocks. I. Acceleration efficiency. *The Astrophysical Journal, 783*(2), 91. https://doi.org/10.1088/0004-637X/783/2/91

Carlson, C. W., Curtis, D. W., Paschmann, G., & Michel, W. (1982). An instrument for rapidly measuring plasma distribution functions with high resolution. *Advances in Space Research, 2*(7), 67–70. https://doi.org/10.1016/0273-1177(82)90151-X

Chen, F. F. (1965). Electric Probes. In R. H. Huddlestone and S. L. Leonard (Eds.), *Plasma Diagnostic Techniques* (pp. 113–200). New York: Academic Press.

Cohen, I. J., Schwartz, S. J., Goodrich, K. A., Ahmadi, N., Ergun, R. E., Fuselier, S. A., et al. (2019). High-Resolution Measurements of the Cross-Shock Potential, Ion Reflection, and Electron Heating at an Interplanetary Shock by MMS. *Journal of Geophysical Research: Space Physics, 124*(6), 3961–3978. https://doi.org/10.1029/2018JA026197

Decker, R. B., & Vlahos, L. (1985). Shock drift acceleration in the presence of waves. *Journal of Geophysical Research: Space Physics, 90*(A1), 47–56. https://doi.org/10.1029/JA090iA01p00047

Dimmock, A. P., Balikhin, M. A., & Hobara, Y. (2011). Comparison of three methods for the estimation of cross-shock electric potential using Cluster data. *Annales Geophysicae, 29*(5), 815–822. https://doi.org/10.5194/angeo-29-815-2011

Dimmock, A. P., Balikhin, M. A., Krasnoselskikh, V. V., Walker, S. N., Bale, S. D., & Hobara, Y. (2012). A statistical study of the cross-shock electric potential at low Mach number, quasi-perpendicular bow shock crossings using Cluster data. *Journal of Geophysical Research: Space Physics, 117*, A02210. https://doi.org/10.1029/2011JA017089

Ergun, R. E., Tucker, S., Westfall, J., Goodrich, K. A., Malaspina, D. M., Summers, D., et al. (2016). The Axial Double Probe and Fields Signal Processing for the MMS Mission. *Space Science Reviews, 199*(1–4), 167–188. https://doi.org/10.1007/s11214-014-0115-x

Eriksson, A. I., Khotyaintsev, Y., & Lindqvist, P.-A. (2007). Spacecraft wakes in the solar wind. In *Proceedings of the 10th Spacecraft Charging Technology Conference* (14pp.).

Fahleson, U. (1967). Theory of electric field measurements conducted in the magnetosphere with electric probes. *Space Science Reviews, 7*(2–3), 238–262. https://doi.org/10.1007/BF00215600

Farris, M. H., Petrinec, S. M., & Russell, C. T. (1991). The thickness of the magnetosheath: Constraints on the polytropic index. *Geophysical Research Letters, 18*(10), 1821–1824. https://doi.org/10.1029/91GL02090

Formisano, V. (1982). Measurement of the potential drop across the Earth's collisionless bow shock. *Geophysical Research Letters, 9*(9), 1033–1036. https://doi.org/10.1029/GL009i009p01033

Formisano, V., & Hedgecock, P. C. (1973). Solar wind interaction with the Earth's magnetic field: 3. On the Earth's bow shock structure. *Journal of Geophysical Research, 78*(19), 3745–3760. https://doi.org/10.1029/JA078i019p03745

Formisano, V., Hedgecock, P. C., Moreno, G., Palmiotto, F., & Chao, J. K. (1973). Solar wind interaction with the Earth's magnetic field: 2. Magnetohydrodynamic bow shock. *Journal of Geophysical Research, 78*(19), 3731–3744. https://doi.org/10.1029/JA078i019p03731

Formisano, V., Moreno, G., Palmiotto, F., & Hedgecock, P. C. (1973). Solar wind interaction with the Earth's magnetic field: 1. Magnetosheath. *Journal of Geophysical Research, 78*(19), 3714–3730. https://doi.org/10.1029/JA078i019p03714

Fuselier, S. A., Lewis, W. S., Schiff, C., Ergun, R., Burch, J. L., Petrinec, S. M., & Trattner, K. J. (2016). Magnetospheric Multiscale Science Mission Profile and Operations. *Space Science Reviews, 199*(1–4), 77–103. https://doi.org/10.1007/s11214-014-0087-x

Gargaté, L., & Spitkovsky, A. (2012). Ion acceleration in non-relativistic astrophysical shocks. *The Astrophysical Journal, 744*(1), 67. https://doi.org/10.1088/0004-637X/744/1/67

Gedalin, M., & Balikhin, M. (2004). Electric potential in the low-Mach-number quasi-perpendicular collisionless shock ramp revisited. *Journal of Geophysical Research, 109*, A03106. https://doi.org/10.1029/2003JA010219

Goodrich, C. C., & Scudder, J. D. (1984). The adiabatic energy change of plasma electrons and the frame dependence of the cross-shock potential at collisionless magnetosonic shock waves. *Journal of Geophysical Research, 89*(A8), 6654–6662. https://doi.org/10.1029/JA089iA08p06654

Gurnett, D. A. (1985). Plasma waves and instabilities. In B. T. Tsurutani & R. G. Stone (Eds.), *Geophysical Monograph Series, Vol. 35*, pp. 207–224. Washington, D. C.: American Geophysical Union. https://doi.org/10.1029/GM035p0207

Hanson, E. L. M., Agapitov, O. V., Mozer, F. S., Krasnoselskikh, V., Bale, S. D., Avanov, L., et al. (2019). Cross-Shock Potential in Rippled Versus Planar Quasi-Perpendicular Shocks Observed by MMS. *Geophysical Research Letters, 46*, 2381–2389. https://doi.org/10.1029/2018GL080240

Hanson, E. L. M., Agapitov, O. V., Vasko, I. Y., Mozer, F. S., Krasnoselskikh, V., Bale, S. D., et al. (2020). Shock Drift Acceleration of Ions in an Interplanetary Shock Observed by MMS. *The Astrophysical Journal, 891*(1), L26. https://doi.org/10.3847/2041-8213/ab7761

Hanson, E. L. M., Agapitov, O. V., Mozer, F. S., Krasnoselskikh, V., Bale, S. D., Avanov, L., et al. (2020). Terrestrial Bow Shock Parameters From MMS Measurements: Dependence on Upstream and Downstream Time Ranges. *Journal of Geophysical Research: Space Physics, 125*(1). https://doi.org/10.1029/2019JA027231

Heppner, J. P., Maynard, N. C., & Aggson, T. L. (1978). Early results from ISEE-1 electric field measurements. *Space Science Reviews, 22*(6), 777–789. https://doi.org/10.1007/BF00212623

Hobara, Y., Walker, S. N., Balikhin, M., Pokhotelov, O. A., Gedalin, M., Krasnoselskikh, V., et al. (2008). Cluster observations of electrostatic solitary waves near the Earth's bow shock: Electrostatic solitary waves. *Journal of Geophysical Research, 113*, A05211. https://doi.org/10.1029/2007JA012789

Hobara, Y., Balikhin, M., Krasnoselskikh, V., Gedalin, M., & Yamagishi, H. (2010). Statistical study of the quasi-perpendicular shock ramp widths. *Journal of Geophysical Research, 115*, A11106. https://doi.org/10.1029/2010JA015659

Hughes, W. J. (1995). The magnetopause, magnetotail, and magnetic reconnection. In M. G. Kivelson and C. T. Russell (Eds.), *Introduction to Space Physics* (pp. 227–287). Cambridge, UK: Cambridge University Press

Hull, A. J., Larson, D. E., Wilber, M., Scudder, J. D., Mozer, F. S., Russell, C. T., & Bale, S. D. (2006). Large-amplitude electrostatic waves associated with magnetic ramp substructure at Earth's bow shock. *Geophysical Research Letters, 33*, L15104. https://doi.org/10.1029/2005GL025564

Hull, A. J., Muschietti, L., Oka, M., Larson, D. E., Mozer, F. S., Chaston, C. C., et al. (2012). Multiscale whistler waves within Earth's perpendicular bow shock: Whistler waves at Earth's bow shock. *Journal of Geophysical Research, 117*, A12104. https://doi.org/10.1029/2012JA017870

Johlander, A., Schwartz, S. J., Vaivads, A., Khotyaintsev, Yu. V., Gingell, I., Peng, I. B., et al. (2016). Rippled Quasiperpendicular Shock Observed by the Magnetospheric Multiscale Spacecraft. *Physical Review Letters, 117*(16), 165101. https://doi.org/10.1103/PhysRevLett.117.165101

Jokipii, J. R. (1982). Particle drift, diffusion, and acceleration at shocks. *The Astrophysical Journal*, 255, 716. https://doi.org/10.1086/159870

Kajdič, P., Hietala, H., & Blanco-Cano, X. (2017). Different Types of Ion Populations Upstream of the 2013 October 8 Interplanetary Shock. *The Astrophysical Journal, 849*(2), L27. https://doi.org/10.3847/2041-8213/aa94c6

Kallenrode, M.-B. (2004). *Space physics: an introduction to plasmas and particles in the heliosphere and magnetospheres*. 3rd, Enlarged Ed. Advanced Texts in Physics. Berlin: Springer.

Kellogg, P. J. (1962). Flow of Plasma around the Earth. *Journal of Geophysical Research, 67*, 3805–3811. https://doi.org/10.1029/JZ067i010p03805

Kennel, C. F., Edmiston, J. P., & Hada, T. (1985). A Quarter Century of Collisionless Shock Research. In R. G. Stone & B. T. Tsurutani (Eds.), *Geophysical Monograph Series, Vol. 34*, pp. 1–36. Washington, D. C.: American Geophysical Union. https://doi.org/10.1029/GM034p0001

Kis, A., Agapitov, O., Krasnoselskikh, V., Khotyaintsev, Y. V., Dandouras, I., Lemperger, I., & Wesztergom, V. (2013). Gyrosurfing acceleration of ions in front of Earth's quasi-parallel bow shock. *The Astrophysical Journal, 771*(1), 4. https://doi.org/10.1088/0004-637X/771/1/4

Khrabrov, A. V., & Sonnerup, B. U. Ö. (1998). De Hoffmann-Teller analysis. In G. Paschmann & P. W. Daly (Eds.), *Analysis methods for multi-spacecraft data* (pp. 221–248). Noordwijk, Netherlands: The International Space Science Institute.

Krasnoselskikh, V., Balikhin, M., Walker, S. N., Schwartz, S., Sundkvist, D., Lobzin, V., et al. (2013). The Dynamic Quasiperpendicular Shock: Cluster Discoveries. *Space Science Reviews, 178*(2–4), 535–598. https://doi.org/10.1007/s11214-013-9972-y

Kruparova, O., Krupar, V., Šafránková, J., Němeček, Z., Maksimovic, M., Santolik, O., et al. (2019). Statistical Survey of the Terrestrial Bow Shock Observed by the Cluster Spacecraft. *Journal of Geophysical Research: Space Physics, 124*, 1539–1547. https://doi.org/10.1029/2018JA026272

Laakso, H., Aggson, T. L., & Pfaff, R. F., Jr. (1995). Plasma gradient effects on double-probe measurements in the magnetosphere. *Annales Geophysicae, 13*, 130–146. https://doi.org/10.1007/s00585-995-0130-z

Lai, S. T. (Ed.). (2011). *Spacecraft Charging*. Reston, VA: American Institute of Aeronautics and Astronautics.

Lario, D., Berger, L., Decker, R. B., Wimmer-Schweingruber, R. F., Wilson, L. B., Giacalone, J., & Roelof, E. C. (2019). Evolution of the Suprathermal Proton Population at Interplanetary Shocks. *The Astronomical Journal, 158*(1), 12. https://doi.org/10.3847/1538-3881/ab1e49

Le Contel, O., Leroy, P., Roux, A., Coillot, C., Alison, D., Bouabdellah, A., et al. (2016). The Search-Coil Magnetometer for MMS. *Space Science Reviews, 199*(1–4), 257–282. https://doi.org/10.1007/s11214-014-0096-9

Lee, M. A., Shapiro, V. D., & Sagdeev, R. Z. (1996). Pickup ion energization by shock surfing. *Journal of Geophysical Research: Space Physics, 101*(A3), 4777–4789. https://doi.org/10.1029/95JA03570

Lefebvre, B., Schwartz, S. J., Fazakerley, A. F., & Décréau, P. (2007). Electron dynamics and cross-shock potential at the quasi-perpendicular Earth's bow shock. *Journal of Geophysical Research, 112*, A09212. https://doi.org/10.1029/2007JA012277

Leroy, M. M., Winske, D., Goodrich, C. C., Wu, C. S., & Papadopoulos, K. (1982). The structure of perpendicular bow shocks. *Journal of Geophysical Research, 87*(A7), 5081–5094. https://doi.org/10.1029/JA087iA07p05081

Lindqvist, P.-A., Olsson, G., Torbert, R. B., King, B., Granoff, M., Rau, D., et al. (2016). The Spin-Plane Double Probe Electric Field Instrument for MMS. *Space Science Reviews, 199*(1–4), 137–165. https://doi.org/10.1007/s11214-014-0116-9

Lobzin, V. V., Krasnoselskikh, V. V., Schwartz, S. J., Cairns, I., Lefebvre, B., Décréau, P., & Fazakerley, A. (2005). Generation of downshifted oscillations in the electron foreshock: A loss-cone instability: Generation of downshifted oscillations. *Geophysical Research Letters, 32*, L18101. https://doi.org/10.1029/2005GL023563

Lobzin, V. V., Krasnoselskikh, V. V., Bosqued, J.-M., Pinçon, J.-L., Schwartz, S. J., & Dunlop, M. (2007). Nonstationarity and reformation of high-Mach-number quasiperpendicular shocks: Cluster observations: Shock front reformation. *Geophysical Research Letters, 34*, L05107. https://doi.org/10.1029/2006GL029095

Lowe, R. E., & Burgess, D. (2003). The properties and causes of rippling in quasi-perpendicular collisionless shock fronts. *Annales Geophysicae, 21*(3), 671–679. https://doi.org/10.5194/angeo-21-671-2003

Luhmann, J. G. (1995). Plasma interactions with unmagnetized bodies. In M. G. Kivelson and C. T. Russell (Eds.), *Introduction to Space Physics* (pp. 203–226). Cambridge, UK: Cambridge University Press

Mazelle, C., Lembège, B., Morgenthaler, A., Meziane, K., Horbury, T. S., Génot, V., et al. (2010). Self-Reformation of the Quasi-Perpendicular Shock: CLUSTER Observations. In *Presented at the Twelfth International Solar Wind Conference* (pp. 471-474). Saint-Malo, France. https://doi.org/10.1063/1.3395905

Mozer, F. S. (2016). DC and low-frequency double probe electric field measurements in space: E Field Measurements. *Journal of Geophysical Research: Space Physics, 121*(11), 10,942-10,953. https://doi.org/10.1002/2016JA022952

Mozer, F. S., & Bruston, P. (1967). Electric field measurements in the auroral ionosphere. *Journal of Geophysical Research, 72*, 1109–1114. https://doi.org/10.1029/JZ072i003p01109

Mozer, F. S., Carlson, C. W., Hudson, M. K., Torbert, R. B., Parady, B., Yatteau, J., & Kelley, M. C. (1977). Observations of paired electrostatic shocks in the polar magnetosphere. *Physical Review Letters, 38*, 292–295. https://doi.org/10.1103/PhysRevLett.38.292

Mozer, F. S., Torbert, R. B., Fahleson, U. V., Falthammar, C. G., Gonfalone, A., & Pedersen, A. (1978). Measurements of quasi-static and low-frequency electric fields with spherical double probes on the ISEE-1 spacecraft. *IEEE Transactions on Geoscience Electronics, 16*, 258–261. https://doi.org/10.1109/TGE.1978.294558

Newbury, J. A., Russell, C. T., & Gedalin, M. (1998). The ramp widths of high-Mach-number, quasi-perpendicular collisionless shocks. *Journal of Geophysical Research: Space Physics, 103*(A12), 29581–29593. https://doi.org/10.1029/1998JA900024

Ofman, L., & Gedalin, M. (2013a). Rippled quasi-perpendicular collisionless shocks: Local and global normals. *Journal of Geophysical Research: Space Physics, 118*, 5999–6006. https://doi.org/10.1002/2013JA018780

Ofman, L., & Gedalin, M. (2013b). Two-dimensional hybrid simulations of quasi-perpendicular collisionless shock dynamics: Gyrating downstream ion distributions. *Journal of Geophysical Research: Space Physics, 118*, 1828–1836. https://doi.org/10.1029/2012JA018188

Ohira, Y. (2016). Injection to rapid diffusive shock acceleration at perpendicular shocks in partially ionized plasmas. *The Astrophysical Journal*, *827*(1), 36. https://doi.org/10.3847/0004-637X/827/1/36

Oka, M., Wilson III, L. B., Phan, T. D., Hull, A. J., Amano, T., Hoshino, M., et al. (2017). Electron Scattering by High-frequency Whistler Waves at Earth's Bow Shock. *The Astrophysical Journal*, *842*(2), L11. https://doi.org/10.3847/2041-8213/aa7759

Park, J., Caprioli, D., & Spitkovsky, A. (2015). Simultaneous Acceleration of Protons and Electrons at Nonrelativistic Quasiparallel Collisionless Shocks. *Physical Review Letters, 114*(8). https://doi.org/10.1103/PhysRevLett.114.085003

Peredo, M., Slavin, J. A., Mazur, E., & Curtis, S. A. (1995). Three-dimensional position and shape of the bow shock and their variation with Alfvénic, sonic and magnetosonic Mach numbers and interplanetary magnetic field orientation. *Journal of Geophysical Research, 100*(A5), 7907. https://doi.org/10.1029/94JA02545

Pesses, M. E., Decker, R. B., & Armstrong, T. P. (1982). The acceleration of charged particles in interplanetary shock waves. *Space Science Reviews, 32*(1–2), 185–204. https://doi.org/10.1007/BF00225184

Pollock, C., Moore, T., Jacques, A., Burch, J., Gliese, U., Saito, Y., et al. (2016). Fast Plasma Investigation for Magnetospheric Multiscale. *Space Science Reviews, 199*(1–4), 331–406. https://doi.org/10.1007/s11214-016-0245-4

Russell, C. T., Anderson, B. J., Baumjohann, W., Bromund, K. R., Dearborn, D., Fischer, D., et al. (2016). The Magnetospheric Multiscale Magnetometers. *Space Science Reviews, 199*(1–4), 189–256. https://doi.org/10.1007/s11214-014-0057-3

Schwartz, S. J. (1998). Shock and Discontinuity Normals, Mach Numbers, and Related Parameters. In G. Paschmann & P. W. Daly (Eds.), *Analysis methods for multi-spacecraft data* (pp. 249–270). Noordwijk, Netherlands: The International Space Science Institute.

Sckopke, N., Paschmann, G., Bame, S. J., Gosling, J. T., & Russell, C. T. (1983). Evolution of ion distributions across the nearly perpendicular bow shock: Specularly and non-specularly reflected-gyrating ions. *Journal of Geophysical Research, 88*(A8), 6121. https://doi.org/10.1029/JA088iA08p06121

Scudder, J. D., Mangeney, A., Lacombe, C., Harvey, C. C., Aggson, T. L., Anderson, R. R., et al. (1986). The resolved layer of a collisionless, high β, supercritical, quasi-perpendicular shock wave: 1. Rankine-Hugoniot geometry, currents, and stationarity. *Journal of Geophysical Research, 91*(A10), 11019. https://doi.org/10.1029/JA091iA10p11019

Scudder, J. D., Mangeney, A., Lacombe, C., Harvey, C. C., & Aggson, T. L. (1986). The resolved layer of a collisionless, high β, supercritical, quasi-perpendicular shock wave: 2. Dissipative fluid electrodynamics. *Journal of Geophysical Research, 91*(A10), 11053. https://doi.org/10.1029/JA091iA10p11053

Scudder, J. D., Mangeney, A., Lacombe, C., Harvey, C. C., Wu, C. S., & Anderson, R. R. (1986). The resolved layer of a collisionless, high β, supercritical, quasi-perpendicular shock wave: 3. Vlasov electrodynamics. *Journal of Geophysical Research, 91*(A10), 11075. https://doi.org/10.1029/JA091iA10p11075

Slavin, J. A., & Holzer, R. E. (1981). Solar wind flow about the terrestrial planets 1. Modeling bow shock position and shape. *Journal of Geophysical Research, 86*(A13), 11401. https://doi.org/10.1029/JA086iA13p11401

Sonnerup, B. U. Ö. & Scheible, M. (1998). Minimum and Maximum Variance Analysis. In G. Paschmann & P. W. Daly (Eds.), *Analysis methods for multi-spacecraft data* (pp. 185–220). Noordwijk, Netherlands: The International Space Science Institute.

Torbert, R. B., Russell, C. T., Magnes, W., Ergun, R. E., Lindqvist, P.-A., LeContel, O., et al. (2016). The FIELDS Instrument Suite on MMS: Scientific Objectives, Measurements, and Data Products. *Space Science Reviews, 199*(1–4), 105–135. https://doi.org/10.1007/s11214-014-0109-8

Vasko, I. Y., Mozer, F. S., Krasnoselskikh, V. V., Artemyev, A. V., Agapitov, O. V., Bale, S. D., et al. (2018). Solitary Waves Across Supercritical Quasi-Perpendicular Shocks: Solitary waves and electron isotropization. *Geophysical Research Letters, 45*, 5809–5817. https://doi.org/10.1029/2018GL077835

Viñas, A. F., & Scudder, J. D. (1986). Fast and optimal solution to the "Rankine-Hugoniot problem." *Journal of Geophysical Research, 91*(A1), 39. https://doi.org/10.1029/JA091iA01p00039

Walker, R. J. & Russell, C. T. (1995). Solar-wind interactions with magnetized planets. In M. G. Kivelson and C. T. Russell (Eds.), *Introduction to Space Physics* (pp. 164–182). Cambridge, UK: Cambridge University Press.

Walker, S. N., Balikhin, M. A., & Nozdrachev, M. N. (1999). Ramp nonstationarity and the generation of whistler waves upstream of a strong quasiperpendicular shock. *Geophysical Research Letters, 26*(10), 1357–1360. https://doi.org/10.1029/1999GL900210

Walker, S. N., Alleyne, H. St. C. K., Balikhin, M. A., André, M., & Horbury, T. S. (2004). Electric field scales at quasi-perpendicular shocks. *Annales Geophysicae, 22*(7), 2291–2300. https://doi.org/10.5194/angeo-22-2291-2004

Walker, S. N., Balikhin, M. A., Alleyne, H. St. C. K., Hobara, Y., André, M., & Dunlop, M. W. (2008). Lower hybrid waves at the shock front: a reassessment. *Annales Geophysicae, 26*(3), 699–707. https://doi.org/10.5194/angeo-26-699-2008

Whipple, E. C. (1981). Potentials of surfaces in space. *Reports on Progress in Physics, 44*(11), 1197–1250. https://doi.org/10.1088/0034-4885/44/11/002

Wilson III, L. B., Koval, A., Szabo, A., Breneman, A., Cattell, C. A., Goetz, K., et al. (2012). Observations of electromagnetic whistler precursors at supercritical interplanetary shocks. *Geophysical Research Letters, 39*, L08109. https://doi.org/10.1029/2012GL051581

Wilson III, L. B., Sibeck, D. G., Breneman, A. W., Contel, O. L., Cully, C., Turner, D. L., et al. (2014a). Quantified energy dissipation rates in the terrestrial bow shock: 1. Analysis techniques and methodology. *Journal of Geophysical Research: Space Physics, 119*, 6455–6474. https://doi.org/10.1002/2014JA019929

Wilson III, L. B., Sibeck, D. G., Breneman, A. W., Contel, O. L., Cully, C., Turner, D. L., et al. (2014b). Quantified energy dissipation rates in the terrestrial bow shock: 2. Waves and dissipation. *Journal of Geophysical Research: Space Physics, 119*, 6475–6495. https://doi.org/10.1002/2014JA019930

Wilson III, L. B., Koval, A., Szabo, A., Stevens, M. L., Kasper, J. C., Cattell, C. A., & Krasnoselskikh, V. V. (2017). Revisiting the structure of low-Mach number, low-beta, quasi-perpendicular shocks. *Journal of Geophysical Research: Space Physics, 122*, 9115–9133. https://doi.org/10.1002/2017JA024352

Winske, D., & Quest, K. B. (1988). Magnetic field and density fluctuations at perpendicular supercritical collisionless shocks. *Journal of Geophysical Research, 93*(A9), 9681–9693. https://doi.org/10.1029/JA093iA09p09681

Wygant, J. R., Bensadoun, M., & Mozer, F. S. (1987). Electric field measurements at subcritical, oblique bow shock crossings. *Journal of Geophysical Research, 92*(A10), 11109. https://doi.org/10.1029/JA092iA10p11109

Young, D. T., Burch, J. L., Gomez, R. G., De Los Santos, A., Miller, G. P., Wilson, P., et al. (2016). Hot Plasma Composition Analyzer for the Magnetospheric Multiscale Mission. *Space Science Reviews, 199*(1–4), 407–470. https://doi.org/10.1007/s11214-014-0119-6

Zank, G. P., Pauls, H. L., Cairns, I. H., & Webb, G. M. (1996). Interstellar pickup ions and quasi-perpendicular shocks: Implications for the termination shock and interplanetary shocks. *Journal of Geophysical Research, 101*(A1), 457–477. https://doi.org/10.1029/95JA02860

Zank, G. P., Hunana, P., Mostafavi, P., Roux, J. A. L., Li, G., Webb, G. M., et al. (2015). Diffusive shock acceleration and reconnection acceleration processes. *The Astrophysical Journal, 814*(2), 137. https://doi.org/10.1088/0004-637X/814/2/137

Appendix 1: Additional figures and tables for Chapter 5

Parameter	Units	Upstream average				Downstream average			
		MMS1	MMS2	MMS3	MMS4	MMS1	MMS2	MMS3	MMS4
Magnetic field strength	nT	6.0	6.0	6.0	6.1	15.1	15.1	15.1	15.2
Shock angle	degrees	63.9	64.9	64.3	64.3	N/A	N/A	N/A	N/A
Ion density	cm^{-3}	7.3	7.3	6.9	6.7	20.2	22.0	21.2	19.1
Ion temperature	eV	23.2	22.3	21.9	24.3	40.6	39.3	39.7	42.6
Ion β	N/A	2.9	2.6	2.5	2.9	2.4	2.2	2.3	2.5
Electron density	cm^{-3}	11.1	10.5	10.5	11.1	34.2	32.4	33.0	33.7
Electron temperature	eV	18.9	19.4	19.3	19.2	26.4	26.8	26.6	26.8
Electron β	N/A	2.3	2.3	2.2	2.3	1.6	1.5	1.5	1.6
Ion speed	km/s	300	303	303	303	352	351	352	352
Ion speed (NIF)	km/s	-89	-86	-86	-86	-25	-25	-25	-25
Electron speed	km/s	312	336	314	309	351	327	350	354
Sonic Mach # (NIF)	N/A	1.2	1.2	1.2	1.1	0.3	0.3	0.3	0.3
Alfvén speed	km/s	39	40	40	39	56	58	57	57
Alfvén Mach # (NIF)	N/A	2.3	2.1	2.1	2.2	0.5	0.4	0.4	0.5
Fast magnetosonic speed	km/s	82	82	82	84	108	108	108	110
Fast magnetosonic Mach # (NIF)	N/A	1.1	1.0	1.1	1.0	0.2	0.2	0.2	0.2
Electron plasma frequency	Hz	29928	29075	29123	29834	52473	51020	51523	52045
Electron cyclotron frequency	Hz	168	168	168	169	422	423	423	424
Ion plasma frequency	Hz	698	679	680	696	1225	1191	1203	1215
Ion cyclotron frequency	Hz	0.092	0.092	0.092	0.093	0.231	0.231	0.231	0.231
Ion inertial length	km	68.3	70.3	70.2	68.5	39.0	40.1	39.7	39.3
Ion gyroradius	km	334	326	318	338	193	191	191	198
Electron inertial length	km	1.60	1.64	1.64	1.60	0.910	0.936	0.927	0.917
Electron gyroradius	km	7.79	7.89	7.85	7.78	3.66	3.69	3.67	3.67

Table A1.1: Average parameters for IP shock 2018-01-08. Upstream time period: 06:40:50-41:00 for most quantities except ion temperature: 06:37:23-33. Downstream time period: 06:42:40-50. Ion density replaced with electron density for calculation of ion plasma frequency, ion inertial length, ion and electron beta, Alfvén speed and Mach number, and Fast Magnetosonic speed and Mach number.

Shock Normal	GSM Components	Angle vs. timing analysis	Variance values
Timing Analysis	(-0.788, -0.022, -0.615)	N/A	N/A
B MVA Min, MMS1	(-0.719, 0.016, -0.694)	7°	(11.2, 1.08, 0.20)
B MVA Min, MMS2	(-0.701, -0.013, -0.713)	8°	(11.0, 1.01, 0.22)
B MVA Min, MMS3	(-0.699, -0.006, -0.715)	8°	(11.1, 1.02, 0.20)
B MVA Min, MMS4	(-0.699, -0.005, -0.715)	8°	(11.1, 1.15, 0.23)
B MVA Min, THB	(-0.645, -0.233, -0.728)	16°	(20.1, 0.661, 0.0317)
B MVA Min, THC	(-0.650, -0.264, -0.712)	17°	(21.0, 0.658, 0.109)

Table A1.2: Summary of shock normals for IP shock 2018-01-08.

Parameter	Units	Upstream average				Downstream average			
		MMS1	MMS2	MMS3	MMS4	MMS1	MMS2	MMS3	MMS4
Magnetic field strength	nT	10.1	10.1	10.1	10.0	25.9	26.0	26.4	26.0
Shock angle	degrees	85.7	84.7	85.2	84.1	N/A	N/A	N/A	N/A
Ion density	cm^{-3}	11.7	12.8	11.8	11.4	42.2	41.1	43.4	42.2
Ion temperature	eV	29.7	30.3	30.2	31.2	157.9	162.4	154.8	160.2
Ion β	N/A	1.4	1.5	1.4	1.4	4.0	4.0	3.9	4.1
Electron density	cm^{-3}	12.5	12.3	12.0	12.3	44.6	43.6	43.4	42.6
Electron temperature	eV	29.5	30.1	29.8	29.9	64.3	64.7	64.7	64.6
Electron β	N/A	1.4	1.5	1.4	1.4	1.6	1.6	1.6	1.6
Ion speed	km/s	316	314	315	315	234	235	235	236
Ion speed (NIF)	km/s	-229	-228	-230	-228	-81	-82	-82	-81
Electron speed	km/s	360	355	346	378	236	227	229	224
Sonic Mach # (NIF)	N/A	2.6	2.6	2.6	2.6	0.5	0.5	0.5	0.5
Alfvén speed	km/s	64	62	65	65	87	88	87	87
Alfvén Mach # (NIF)	N/A	3.6	3.7	3.6	3.5	0.9	0.9	0.9	0.9
Fast magnetosonic speed	km/s	108	107	109	110	197	199	196	198
Fast magnetosonic Mach # (NIF)	N/A	2.1	2.1	2.1	2.1	0.4	0.4	0.4	0.4
Electron plasma frequency	Hz	31693	31447	31059	31427	59768	59113	58953	58414
Electron cyclotron frequency	Hz	281	282	283	280	723	727	737	726
Ion plasma frequency	Hz	715	746	717	703	1357	1338	1375	1356
Ion cyclotron frequency	Hz	0.153	0.154	0.155	0.153	0.395	0.397	0.402	0.397
Ion inertial length	km	67.3	64.6	67.1	68.5	35.3	35.9	34.9	35.4
Ion gyroradius	km	245	245	243	251	248	250	241	249
Electron inertial length	km	1.51	1.52	1.54	1.52	0.802	0.812	0.814	0.821
Electron gyroradius	km	5.79	5.80	5.77	5.82	3.26	3.24	3.21	3.25

Table A1.3: Average parameters for bow shock crossing 2017-11-02. Upstream time period: 04:26:23-33. Downstream time period: 04:26:50-27:00.

Shock Normal	GSM Components	Angle vs. timing analysis	Variance values
Timing Analysis	(0.594, 0.717, 0.364)	N/A	N/A
Slavin and Holzer 1981	(0.802, 0.597, 0.010)	25°	N/A
E MVA Max, MMS1	(0.894, 0.443, 0.074)	29°	(2.08, 0.44, 0.14)
E MVA Max, MMS2	(0.516, 0.825, 0.231)	11°	(5.58, 0.27, 0.05)
E MVA Max, MMS3	(0.619, 0.681, 0.390)	3°	(4.69, 0.27, 0.04)
B MVA Min, MMS1	(0.990, 0.042, -0.137)	55°	(72.35, 3.01, 2.46)
B MVA Min, MMS2	(-0.799, 0.593, 0.101)	89°	(73.68, 3.12, 3.07)
B MVA Min, MMS3	(0.302, 0.952, -0.042)	32°	(75.92, 3.39, 3.07)
B MVA Min, MMS4	(0.968, 0.216, -0.128)	47°	(74.69, 3.09, 2.88)

Table A1.4: Summary of shock normals for bow shock crossing 2017-11-02. The magnetic field MVA shock normals shown were computed using data from the upstream (04:26:23-33) and downstream (04:26:50-27:00) time ranges; other time ranges were attempted with similar results.

Shock	**Potential**	**MMS1**	**MMS2**	**MMS3**
IP Shock	NIF, Measured ($\boldsymbol{E} \cdot \boldsymbol{B} = 0$)	26 ± 6 V	28 ± 6 V	24 ± 6 V
IP Shock	NIF, Proxy from electron motion	40 ± 10 V	40 ± 10 V	42 ± 10 V
Bow Shock	NIF, Measured ($\boldsymbol{E} \cdot \boldsymbol{B} = 0$)	440 ± 30 V	380 ± 50 V	290 ± 30 V
Bow Shock	NIF, Proxy from electron motion	250 ± 70 V	260 ± 70 V	240 ± 70 V

Table A1.5: Summary of cross-shock potential and proxy for both shocks.

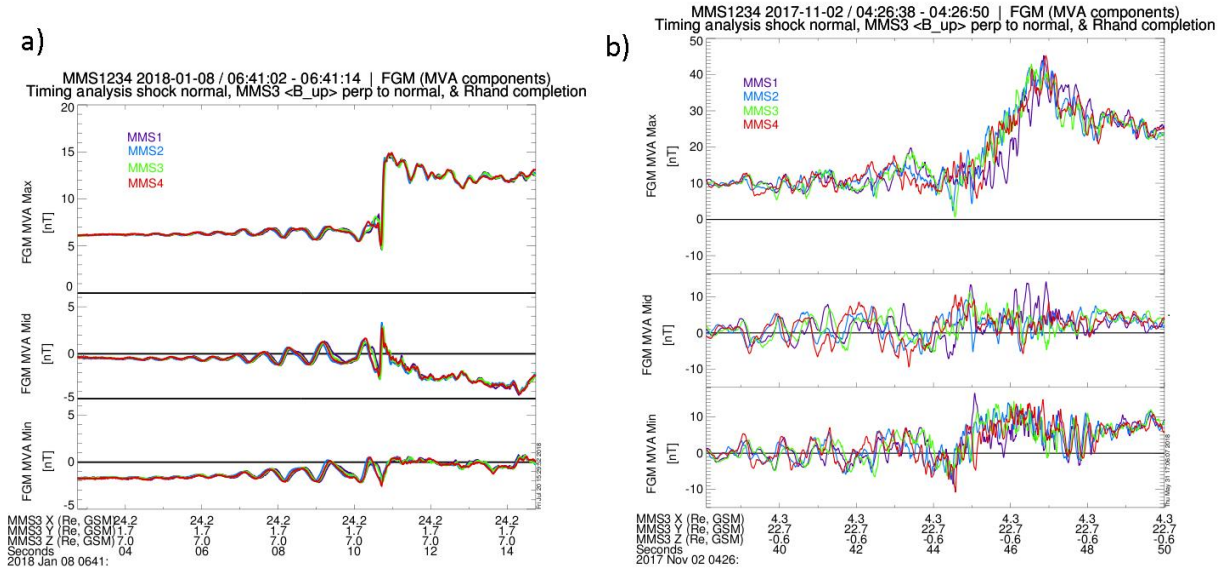

Figure A1.1: MMS1-4 Magnetic field components for (a) 2018-01-08 / 06:41:02 - 06:41:14 and (b) 2017-11-02 / 04:26:28 – 04:26:50. The MVA coordinate system for each shock is described in the text.

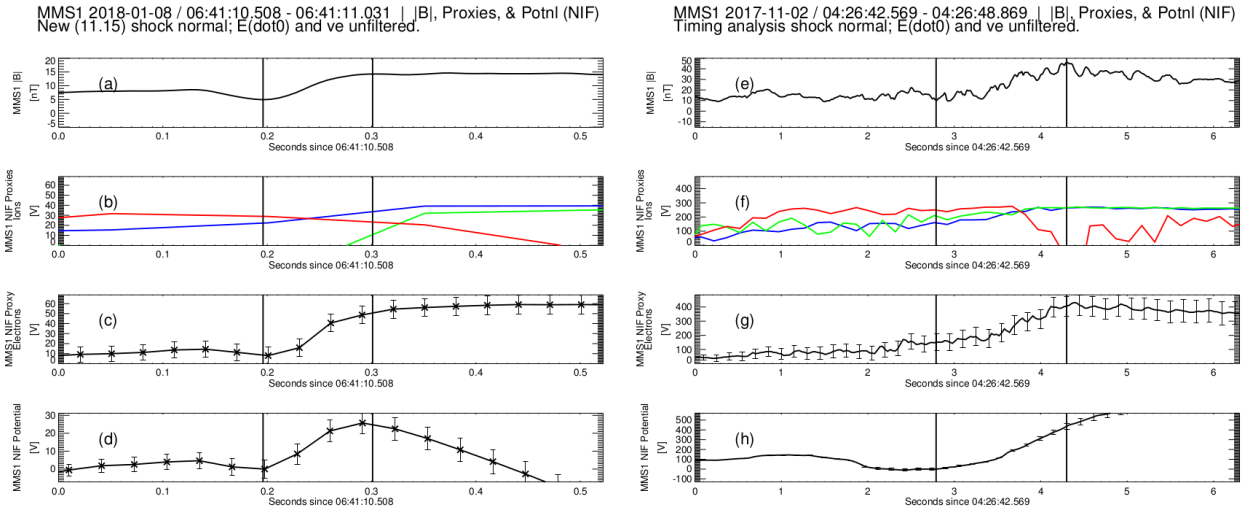

Figure A1.2: MMS1 magnetic field magnitude, potential proxies, and cross-shock potential for (a)-(d) IP shock on 2018-01-08 and (e)-(h) bow shock crossing on 2017-11-02. The ramp is marked by vertical lines through all panels. Panels (a), (e): Magnetic field magnitude. Panels (b), (f): Potential proxies that depend on ion moments: Φ_v from ion velocity (blue), Φ_n from ion density (green), and Φ_P from pressure balance (red). Note that Φ_P depends on the pressure due to electrons as well as ions. Panels (c), (g): Potential proxy that does not depend on ion moments: Φ_e from electron equation of motion. Panels (d), (h): Cross-shock potential in NIF.

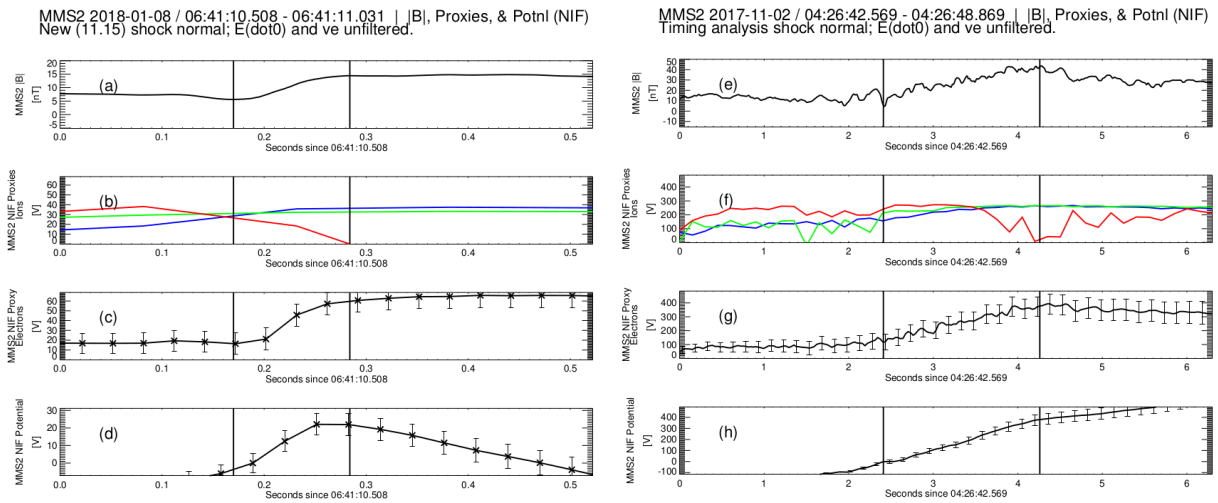

Figure A1.3: MMS2 magnetic field magnitude, potential proxies, and cross-shock potential for (a)-(d) 2018-01-08 IP shock and (e)-(h) 2017-11-02 bow shock. Vertical lines through all panels mark the ramp. Panels (a), (e): Magnetic field magnitude. Panels (b), (f): Potential proxies from ion moments: Φ_v from ion velocity (blue), Φ_n from ion density (green), and Φ_P from pressure balance (red). Φ_P depends on the pressure due to electrons as well. Panels (c), (g): Potential proxy independent of ion moments: Φ_e from electron equation of motion. Panels (d), (h): Cross-shock potential in NIF**.**

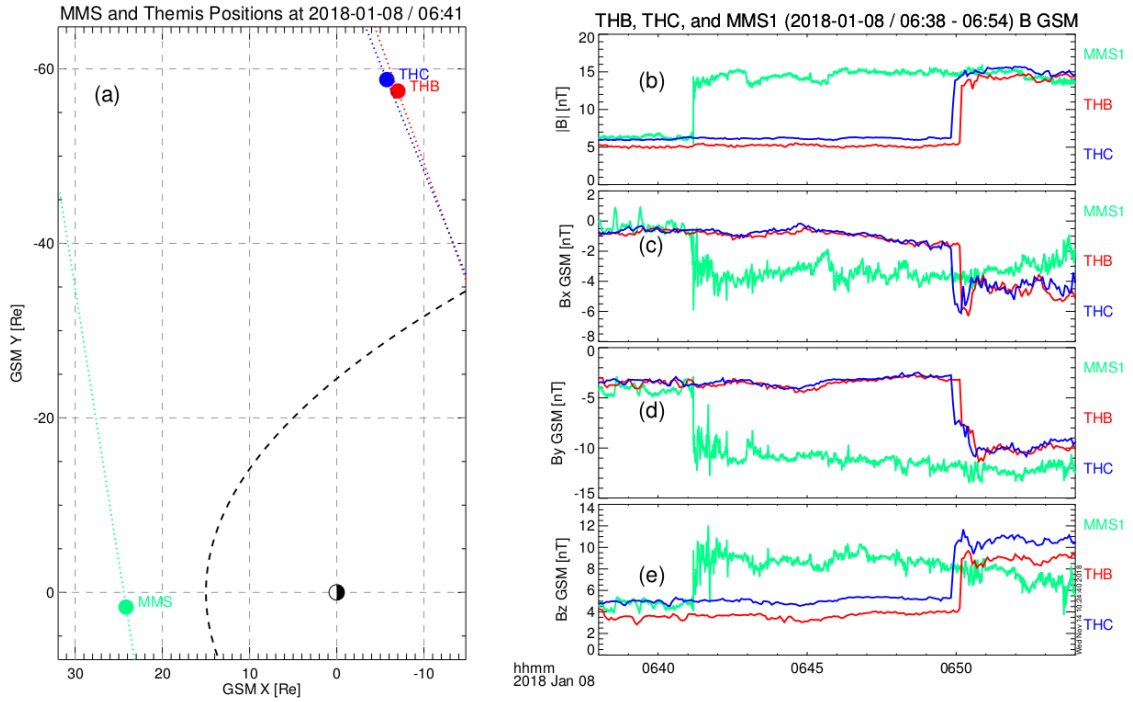

Figure A1.4: Observations of 2018-01-08 IP shock by MMS and ARTEMIS (THEMIS B and C). The shock front passed the MMS constellation around 06:41:10, THEMIS C at 06:49:53, and THEMIS B at 06:50:07. Panel (a): Geometry of the shock surface in the GSM x-y plane as

observed at MMS1, THB, and THC. Panels (b)-(e): magnetic field magnitude (b) and GSM components (c)-(e) observed by MMS1 (light green), THEMIS B (red), and THEMIS C (blue).

Appendix 2: Additional table for Chapter 6

Shock time	$\hat{n}$ GSM RH	$\alpha_{RH,SH}$	$\langle v_{sh} \rangle$	$\langle \theta_{Bn} \rangle$	Normalized differences		
	N/A	deg	km/s	deg	$\hat{n}$	v_{sh}	θ_{Bn}
2015-10-07 / 12:07:12	(.888, .328, -.321)	5.0	12.7±1.7	73.6±1.0	1.347	3.364	1.347
2015-10-21 / 10:52:50	(.951, .189, -.246)	4.8	11.6±1.9	83.5±1.0	1.360	15.752	2.751
2015-11-03 / 09:19:58	(.998, -.009, .070)	8.4	140.4±3.9	38.8±1.0	2.090	3.427	1.244
2015-11-13 / 13:58:25	(.977, .116, -.178)	8.8	4.5±1.7	80.8±1.0	1.523	11.078	2.724
2015-11-29 / 11:31:48	(.990, .087, -.109)	1.8	9.5±1.7	82.6±1.0	1.684	2.465	1.470
2015-12-10 / 05:25:39	(.994, -.091, -.052)	1.3	8.9±1.3	87.0±1.0	0.881	15.856	1.221
2015-12-20 / 00:04:56	(.966, -.214, -.143)	6.2	142.2±2.1	74.7±1.0	1.020	12.164	1.206
2015-12-20 / 00:24:57	(.969,-.197 ,-.148)	6.8	20.1±1.6	76.0±1.0	0.958	5.038	5.390
2015-12-20 / 01:24:53	(.988, -.152, -.031)	6.5	32.5±1.6	74.2±1.0	1.276	3.484	1.813
2015-12-22 / 07:14:44	(.989, -.130, -.065)	3.3	74.5±1.3	59.4±1.0	1.701	16.016	3.403
2015-12-28 / 05:07:17	(.995, .022, -.096)	14.3	-24.0±1.1	81.4±1.0	5.153	10.166	3.247
2016-11-09 / 12:58:05	(.971, .193, -.139)	9.6	-20.5±1.2	84.1±1.0	6.763	13.566	5.101
2016-12-05 / 12:46:10	(.969, .228, -.096)	4.8	4.4±1.5	75.9±1.0	0.736	3.597	1.356
2016-12-06 / 11:18:04	(.996, .091, .017)	5.7	30.2±1.6	80.7±1.0	2.535	7.338	5.055
2016-12-06 / 12:04:27	(.993, .100, .061)	6.3	256.5±3.8	89.4±1.0	1.338	12.246	2.112
2016-12-07 / 15:16:26	(.941, .338, -.031)	2.2	-2.4±1.4	72.7±1.0	2.207	4.730	1.652
2016-12-09 / 10:43:20	(.992, .117, .035)	2.4	-10.7±1.9	82.6±1.0	1.609	13.887	3.691
2016-12-17 / 12:06:48	(.980, .199, -.009)	1.5	0.7±1.0	52.0±1.0	2.561	4.333	2.038
2016-12-31 / 06:08:33	(.998, -.057, .004)	1.3	34.5±6.0	37.9±1.0	1.826	11.725	9.643
2016-12-31 / 12:39:33	(1.000, .004, .031)	4.9	38.9±1.1	63.8±1.0	3.128	17.829	1.565
2017-01-18 / 05:38:50	(.990, -.117, .074)	7.2	25.0±1.4	73.6±1.0	3.345	14.581	11.030
2017-10-03 / 20:34:57*	(.923, .382, -.052)	16.9	-110.5±2.7	79.3±1.0	2.268	3.803	2.566
2017-10-03 / 20:52:30*	(.876, .481, -.044)	11.4	-83.6±2.9	82.6±1.0	1.508	3.619	1.011
2017-10-09 / 18:13:51*	(.811, .584, .035)	7.2	-59.6±4.2	57.4±1.0	1.661	1.772	4.043
2017-10-09 / 19:04:23	(.805, .590, -.052)	6.0	-48.1±2.9	79.0±1.0	1.405	2.516	3.168
2017-10-09 / 19:54:30*	(.824, .566, .009)	8.5	-75.1±3.5	86.1±1.0	0.824	2.036	1.334
2017-10-09 / 21:32:54*	(.827, .563, .004)	9.4	-45.7±3.1	81.9±1.0	1.033	3.207	4.543
2017-10-10 / 08:11:53*	(.860, .486, -.156)	13.9	-87.1±3.5	78.3±1.0	1.020	4.303	7.964
2017-10-13 / 03:08:10*	(.789, .611, -.065)	6.7	-81.2±4.5	73.4±1.0	0.922	1.991	2.696
2017-10-18 / 01:39:37*	(.893, .441, -.087)	10.0	-59.8±2.6	82.2±1.0	1.705	4.124	4.769
2017-10-19 / 00:56:54	(.880, .473, .044)	15.8	-87.6±2.6	72.1±1.0	0.874	1.319	2.982
2017-10-24 / 20:03:13	(.761, .558, .330)	15.7	279.1±3.8	76.3±1.0	3.288	10.062	3.090
2017-11-02 / 04:26:45	(.903, .430, -.009)	11.3	-49.3±3.1	68.6±1.0	0.650	1.871	1.193
2017-11-02 / 08:29:22	(.899, .400, -.178)	13.7	-5.1±2.8	84.8±1.0	1.965	5.020	4.271
2017-11-14 / 19:57:09	(.958, .279, -.070)	8.9	36.9±2.3	70.4±1.0	3.382	5.465	1.972
2017-11-25 / 01:26:12	(.945, .321, .061)	9.0	-23.4±1.9	77.6±1.0	2.033	7.391	4.653
2017-11-25 / 23:40:01	(.900, .183, -.395)	28.9	5.6±6.8	67.9±2.4	0.116	0.353	0.783
2017-11-28 / 18:00:56	(.988, .156, .013)	4.2	-18.1±1.2	81.7±1.0	0.583	6.254	0.248
2017-12-23 / 10:44:52	(.963, .267, .035)	8.4	-4.8±1.3	75.0±1.0	2.226	4.046	1.678
2017-12-26 / 22:09:12	(.986, -.161, .035)	2.4	-7.7±1.1	78.6±1.0	1.614	8.871	3.992
2017-12-31 / 22:09:33	(.910, .331, .250)	3.7	19.2±1.7	77.7±1.0	1.269	3.967	1.924
2018-01-12 / 03:22:34	(.986, .052, .156)	5.4	-23.7±1.7	86.2±1.0	1.976	4.370	1.414
2018-01-18 / 11:50:38	(.964, -.254, .074)	3.4	-7.8±1.3	88.5±1.0	1.416	10.142	5.046
2018-02-03 / 19:28:55	(.987, -.052, .152)	1.5	-8.7±1.4	89.4±1.0	1.121	4.154	0.599
2018-02-07 / 06:50:30	(.945, -.325, -.022)	10.1	-41.9±1.8	72.1±1.0	1.256	4.782	1.905
2018-02-09 / 09:18:58	(.969, .042, .242)	7.5	-11.2±1.4	58.0±1.0	4.665	4.615	2.598
2018-02-10 / 01:00:58	(.887, -.452, -.092)	1.9	-13.8±2.0	85.2±1.0	1.720	1.581	1.744
2018-02-12 / 20:02:14	(.899, -.419, -.131)	7.9	-42.6±18.6	80.6±13.5	0.362	0.622	0.161
2018-02-14 / 23:48:09	(.978, -.094, .187)	7.6	-14.8±1.4	77.5±1.0	0.886	3.292	1.849
2018-03-01 / 01:43:11	(.977, -.163, -.139)	12.6	-8.5±1.3	65.4±1.0	2.139	9.417	3.767
2018-03-13 / 04:52:28	(.536, .773, .338)	82.1	-188.6±2.1	74.8±1.4	1.456	1.764	6.277

Table A2.1. Summary of parameters for the preferred upstream and downstream combination for each of the 51 shocks. Columns from left to right hold the shock time; the GSM components of the RH normal, averaged over the four; angle between the RH and SH normals; shock speed; shock angle θ_{Bn}; and normalized differences of the normal, shock speed, and shock angle expressed in units of the standard deviations of each parameter. An asterisk following the shock time in the far left column indicates that the ramp observation time for the four spacecraft differs by more than a few seconds.

Appendix 3: Test-particle simulations from Chapter 7

To address the origin of a few keV protons observed in a relatively narrow range of pitch angles upstream of the shock, we have performed a test-particle simulation of the interaction of incoming protons with the shock magnetic field and cross-shock electrostatic field. The shock is assumed to be planar with the x-axis along the shock normal directed into the upstream region, the z-axis in the plane of the shock and along the major magnetic field component B_z, and the y-axis completing the right-hand coordinate system. The magnetic field of the shock is modelled with two components, $\boldsymbol{B} = (B_x, 0, B_z)$, where $B_x = B_u \sin\theta_{Bn}$ =const and $B_z(x) = B_u \cos\theta_{Bn} + 0.5\Delta B(1 - \tanh(x/h_B))$, where B_u~6nT is the magnetic field magnitude in the upstream region ($x \to +\infty$), θ_{Bn}~115° is the angle between the x-axis and the magnetic field in the upstream region, ΔB~9nT is the magnetic field jump across the shock, and h_B is the gradient scale of the magnetic field. The electrostatic cross-shock field is modelled with $E_x = E_0 \cosh^{-2}(x/h_E)$, where E_0~1.1mV/m is the peak value of the cross-shock electrostatic field and h_E is the gradient scale of the cross-shock electrostatic field. The gradients scales $h_B = 8$km and $h_E = 14$km were estimated by fitting the measured magnetic field and electrostatic field profiles to the model profiles.

The simulation was performed in the Normal Incidence Frame (NIF). In that frame protons are incoming into the shock with the bulk velocity of about V_n~90 km/s in the direction opposite to the normal (i.e. toward –x direction) and the corresponding motional electric field of 0.5 mV/m is directed in the –y direction. To model the distribution function of incoming protons we run 200 thousand protons from a far upstream region and follow proton trajectories until they get either into a far downstream region or back into the far upstream region. The distribution function of the incoming protons is assumed to be an isotropic Maxwellian drifting with velocity 90 km/s opposite to the normal and temperature of 10 eV, which is rather close to the proton temperature estimate by the Wind spacecraft located in the solar wind about 200 R_E upstream of MMS. The results of the simulations are transformed into the spacecraft frame to facilitate the comparison with the MMS measurements.

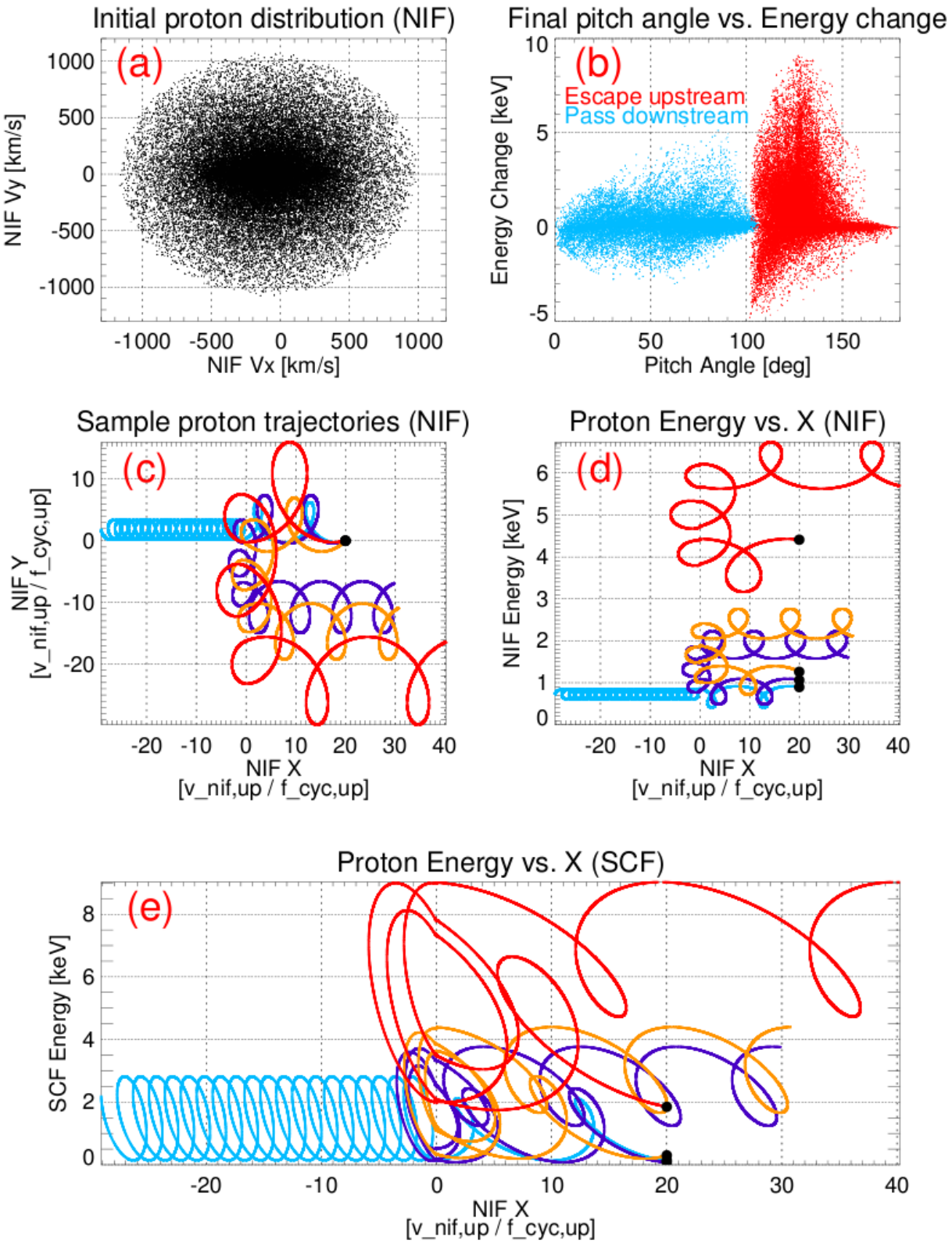
Initial proton distribution (NIF)
(a)
NIF Vy [km/s]
NIF Vx [km/s]
Final pitch angle vs. Energy change
(b)
Escape upstream
Pass downstream
Energy Change [keV]
Pitch Angle [deg]
Sample proton trajectories (NIF)
(c)
NIF Y
[v_nif,up / f_cyc,up]
NIF X
[v_nif,up / f_cyc,up]
Proton Energy vs. X (NIF)
(d)
NIF Energy [keV]
NIF X
[v_nif,up / f_cyc,up]
Proton Energy vs. X (SCF)
(e)
SCF Energy [keV]
NIF X
[v_nif,up / f_cyc,up]

Figure A3.1. Summary of test-particle simulation results. All panels but (e) show data in NIF. Panel (a): The distribution of velocities V_x and V_y of incoming protons, corresponding to 200 thousand protons with velocities distributed uniformly in a sphere centered at V_x~-90km/s. Panel (b): Change in energy (keV) versus final pitch angle (degrees). Protons that escape to the upstream are indicated with red dots, while protons transmitted downstream are light blue. Panel (c): Trajectories of four sample protons in the NIF x-y plane. The protons are launched from x=20, while the shock ramp is at x=0. Distances are scaled by the ratio of the average upstream NIF velocity and the corresponding proton cyclotron frequency. Panel (d): Proton energy in the NIF (keV) versus position x for the same four protons as in panel (c). Panel (e): Proton energy in the spacecraft-frame (keV) versus position x for the same four protons as in panels (c) and (d).

Figure A3.1 demonstrates the results of the test-particle simulation. Panel (a) presents the distribution of initial velocities of launched protons in the (V_x,V_y)-plane. Panel (b) presents the distribution of the energy change and pitch angles of the protons after interaction with the shock as viewed in the spacecraft frame. Protons ending up in the far downstream are observed at all pitch angles from 0° to ~90° and accelerated by up to a few keV. Protons escaping back to the far upstream region are observed in a narrow range of pitch angles, 120°-150°, and can be seen to be accelerated by up to 7 keV. Panel (c) presents trajectories of several protons interacting with the shock; the blue trace indicates a proton that is transmitted to the downstream, while violet, orange, and red traces represent protons that finally escape to the far upstream region. The same color scheme is employed in panels (d) and (e). Panel (d) shows the evolution of proton energy as viewed in the NIF, while the energy evolution in the spacecraft frame is shown in panel (e); both demonstrate that the acceleration experienced by the protons is due to classical shock drift acceleration (SDA), i.e. protons drift along the front of the shock and are accelerated by the motional electric field of 0.5 mV/m.

The trajectories of the test protons allow us to compute the phase space density of protons escaping back to the far upstream and ending up in the downstream regions of the shock. For that purpose we use Liouville's theorem and consider each of 200 thousand protons as a macro-particle carrying the phase space density determined by the initial phase space density of incoming protons. The phase space density is then used to compute the DEF of each proton population.